UiT
THE ARCTIC
UNIVERSITY
OF NORWAY

Faculty of Science and Technology
Department of Physics and Technology

Classification of Marine Oil Spills and Look-alikes in Sentinel-1 TOPSAR and Radarsat-2 ScanSAR Images

Magnus Wilhelmsen

EOM-3901 Master thesis in Energy, Climate and Environment 2018, 30 SP

June 2018

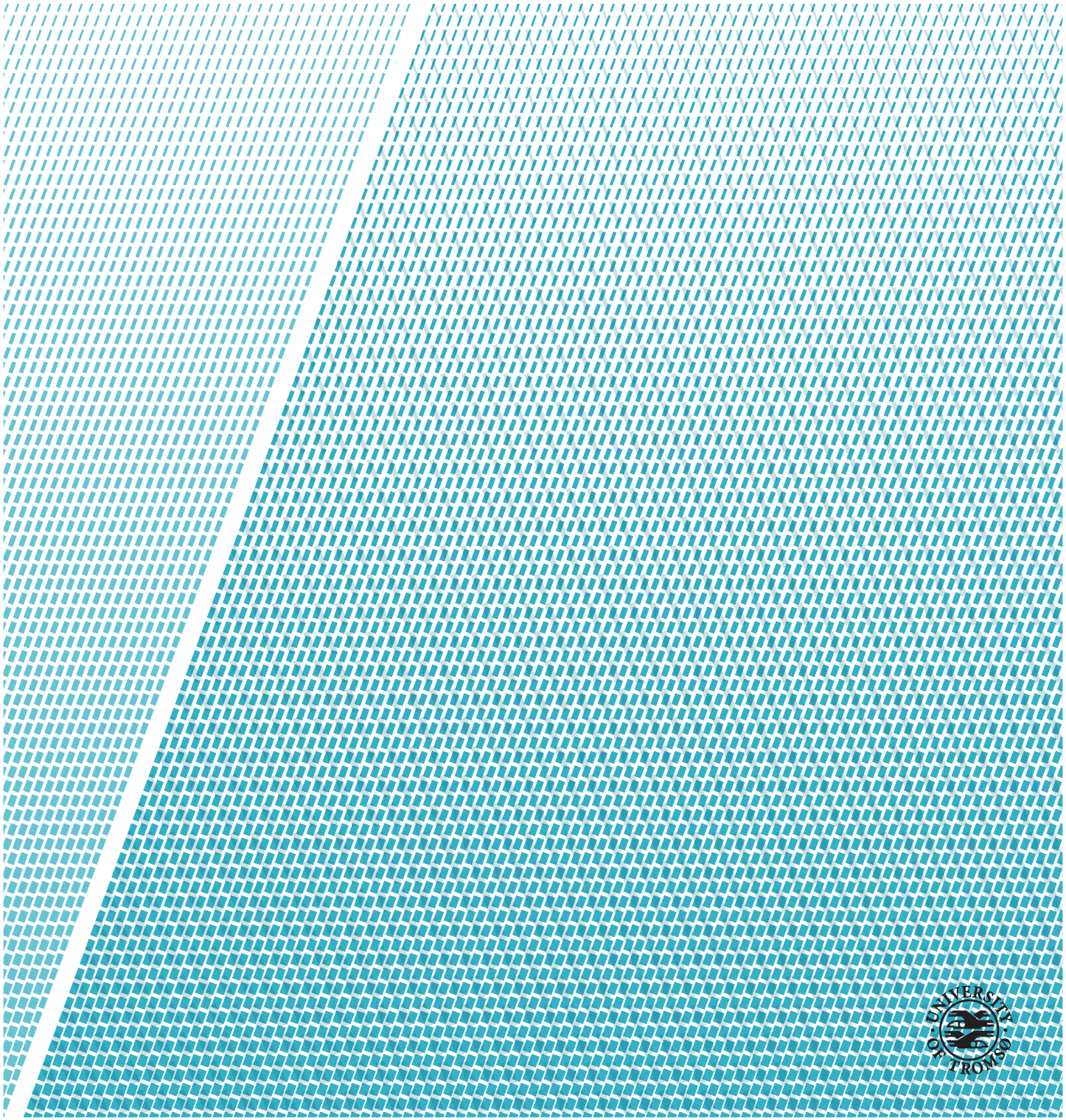

Abstract

The main focus of this thesis is to investigate the potential for discrimination between marine oil spills and look-alikes in Synthetic Aperture Radar (SAR) imagery, using log-cumulants and other parameters describing the characteristics of a dark feature. Look-alikes denotes other phenomena known to cause similar SAR signatures as mineral oil. It is vital for the companies managing oil detection services, e.g. Kongsberg Satellite Services (KSAT), to minimize the number of false alarms caused by look-alikes. A selection of parameters are investigated in this thesis, including descriptors currently used by KSAT, and parameters from literature quantitatively describing the same characteristics. Especially the statistical descriptors known as log-cumulants are thoroughly explored and analysed, which are currently not embedded in KSATs oil spill detection service. The potential for using the parameters to discriminate between mineral oil and look-alikes are evaluated using a linear Support Vector Machine (SVM). The analysis is performed on SAR data from KSATs detection service, i.e. large scale, low resolution and single/dual polarization SAR scenes, for which in-situ information is available.

The separability obtained between mineral oil and look-alikes using log-cumulants are found to be highly sensor specific. No significant separation are found for dark features acquired by RADARSAT-2 (RS2) in ScanSAR mode. An improved separation are found for the data acquired by Sentinel-1 (S1). Especially the separation between mineral oil and look-alikes assumingly created by atmospheric/oceanographic phenomena proves to be promising. The discrimination obtained in the log-cumulant domain appears to increase with resolution. No clear separation is identified for mineral oil and the class of look-alikes composed of other matter on the surface. The S1 log-cumulant analysis indicates that mineral oil tends to generate dark features with both a greater damping effect and texture than both classes of look-alikes.

The SVM is found to discriminate well between mineral oil and look-alikes assumingly created by atmospheric/oceanographic phenomena using S1 data. The first Hu-moment, compactness, coefficient of variation, along with the normalized first order log-cumulant are identified as the most promising parameters. These are objective quantitative parameters, measuring the same

characteristics as some of the descriptors currently used in KSATs oil detection service, which are mainly set qualitatively by visual inspection. In general, the quantitative measures performs better and more consistently compared to the descriptors used by KSAT. Resolution is found to be vital to obtain separation between the classes.

The work presented in this thesis adds to the research already conducted on the discrimination of mineral oil and look-alikes in SAR imagery. To the authors knowledge, this is the first log-cumulant analysis conducted on wide swath SAR data, i.e. the data type currently being used operationally by the oil detection services. The classification results obtained indicates that the parameters used today can advantageously be quantified, which can potentially contribute towards further automation of the oil detection services.

Acknowledgements

First and foremost, I would like to express my sincere gratitude towards my supervisor Stine Skrunes, for always finding the time to guide me through this master thesis. Especially thanks for the discussions, extensive knowledge, enthusiasm, encouraging feedback and last but not least for proof-reading my thesis countless times. I would also like to thank my main supervisor Camilla Brekke, for always providing insightful comments and for proof-reading. Your knowledge is greatly appreciated. Thanks to Thomas Kræmer for helping me move the segmentation masks, and for offering your technical expertise whenever needed.

I would also like to thank Kongsberg Satellite Services for giving me the opportunity to cooperate with them on this thesis. Thanks for allowing me to work as a summer intern to create the dataset used in this thesis, and for giving me insight into your oil detection service. Thanks to my supervisor Tony Bauna, for providing your expertise and for guiding me through the summer internship.

Thanks to my fellow students, for making these five years great, for your terrible humour and for participating in countless table tennis matches.

Thanks to my parents for providing continuous encouragement throughout my years of study, and my father for proof-reading the work. Last but not least, I would like to express my gratitude toward my girlfriend, Terese Helen Staff, for her love and support through this thesis.

Contents

List of Figures

List of Tables

List of Symbols

$\bar{\kappa}$	Cohen's kappa coefficient
$\bar{\nu}$	Radar frequency
η_{pq}	Normalized central moment of order (p+q)
$\hat{\phi}_n$	Hu invariant moment of order n
$\hat{m}_{pq}$	Moment of order (p+q)
κ_ν	Log-cumulant of order ν
λ	Radar wavelength
λ_B	Surface wavelength
λ_i	Lagrange multipliers
$\mathcal{F}$	Fourier transform
$\mathcal{M}$	Mellin transform
μ	Mean
μ_{pq}	Central moment of order (p+q)
ν	Radar frequency
ω	Angular frequency
ω_0	Bias
ω_c	Carrier angular frequency

ω_n	Membership function for class n
Φ_X	First characteristic function of random variable X
ϕ_X	First characteristic function of second kind for random variable X
Π	Classification accuracy
$\boldsymbol{\omega}$	Weight vector
Ψ_x	Second characteristic function of random variable X
ψ_X	Second characteristic function of second kind for random variable X
σ	Radar cross section
τ	Pulse length
Θ	Look angle
ξ	Slack variable
A	Magnitude of complex signal
A_e	Effective antenna area
A_g	Area on ground
b	Bandwidth
C	Compactness
c	Speed of light
G	Positive constant
$g(\boldsymbol{x})$	Linear discriminant function
G_g	Ground gain
G_t	Antenna gain
h	Height of satellite

h_{rms}	Root mean square wave height
I	Intensity
J	Cost function
L	Antenna length
m_v	Moment of order v
N	Number of looks
P_g	Power incident on an area
P'_g	Reflected power from the ground
P_r	Power recieved at antenna
P_t	Transmitted power from antenna
p_x	Probability density function of a random variable
r	Distance from satellite to object on the ground
s	Standard deviation of a random variable
t	Time
X_a	Azimuth resolution
Y	Imaginary part of complex signal
y_i	Class label vector
Z	Real part of complex signal
z	Margin
$\mathbf{x}$	Feature vector

List of Abbreviations

CA Classification Accuracy

CF Characteristic Function

COM Confimed Other Matter

CSN Clean Sea Net

dB Decibels

EM Electromagnetic Wave

EMSA European Marine Safety Agency

EW Extra Wide Swath

GML Geographic Markup Language

GRD Ground Range Detected

GRDH Ground Range Detected High

GRDM Ground Range Detected Medium

H Horizontally

IW Interferometric Wide-swath

KSAT Kongsberg Satellite Services

LUT Look-Up Table

NESZ Noise-Equivalent Sigma-Zero

PDF Probability Density Function

RAR Real Aperture Radar

RCS Radar Cross Section

RMS Root Mean Square

RS2 RADARSAT-2

S1 Sentinel-1

S1A Sentinel-1A

S1B Sentinel-1B

SAR Synthetic Aperture Radar

SGF SAR Georeferenced Fine

SNR Signal-to-Noise Ratio

SVM Support Vector Machine

TOPSAR Terrain Observation with Progressive Scans SAR

V Vertically

1 Introduction

Marine oil spills impose a serious threat to both the economy and the environment. Consequences are damage to the coastal ecology and seabirds covered in oil [Brekke and Solberg, 2005]. Operational discharges from ships constitute large portions of the oil spills, and many of these are illegal. Synthetic Aperture Radar (SAR) sensors are operationally used by oil detection companies to detect and monitor oil spills. Oil dampens the surface capillary and short gravity waves, which decreases the radar backscatter in these regions. This makes the oil slicks appear as dark features in a SAR image. One of the limitations with detection of oil spills using SAR systems are false detections caused by look-alikes, i.e. natural phenomena that also produce dark features in SAR-imagery.

Kongsberg Satellite Services (KSAT) is a world leading provider of ground station services for polar orbiting satellites. They provide around-the-clock oil spill detection service in marine environments. At KSAT, classification of dark features is currently done manually based on the operators knowledge and experience. Classification performed by humans often suffer from inconsistency, consequently there is a need for an automatic classification system that can aid, and in the long run replace the operators. Such a classification system would be much more consistent and hopefully recognize patterns that the human brain can't. Uncovering parameters that can help to distinguish between oil and look-alikes is therefore of major importance for the companies remotely detecting oil spills.

1.1 Objective

The objective of this thesis is to investigate the potential for using SAR to discriminate between marine oil spills and look-alikes. This work consists of two parts. First the potential for using log-cumulant to discriminate between mineral oil and look-alikes are explored. Then several other parameters describing the characteristics of a dark feature are investigated, then their potential for discrimination of mineral oil and look-alikes are quantified using a linear Support Vector Machine (SVM).

Log-cumulants are statistical descriptors related to radar texture, and [Skrunes et al., 2015a, Skrunes et al., 2015b] proposed the use of these to discriminate between mineral oil and look-alikes. Some potential were observed for discrimination of mineral oil and look-alikes using quad- and dual-polarization data with a high resolution and low spatial coverage [Skrunes et al., 2015a]. The log-cumulants was analysed in a preliminary study, using low resolution single-polarization RADARSAT-2 ScanSAR scenes. Neither of the log-cumulants were found to have a clear separation between mineral oil and look-alikes. The coarse resolution of the ScanSAR scenes seems to remove much of the separation previously found.

In this thesis, the log-cumulants will be further analysed and their ability to classify dark features in SAR data will be investigated. New classes will be added, and data from a new sensor with increased resolution will be explored. The parameters currently used in KSATs oil detection service are explored, in addition to parameters proposed in research papers, quantitatively describing the same properties as KSATs parameters. A linear SVM is built to evaluate and compare the parameters. The scenes investigated here are acquired from KSAT and [ESA, 2018], alongside ground truth information about each dark feature.

1.2 Contributions to the Research Field

To the author's knowledge there exists no previous study of log-cumulants using wide swath SAR data, i.e. this is the first study conducted on this type of data. The immediate contributions to the field of research are:

- Analysis of log-cumulants on data used operationally.
- Further evaluation of the potential for using log-cumulants to discriminate between mineral oil and look-alikes.

- Construction of a linear SVM classifying mineral oil and look-alikes, and identification of useful parameters.

- Comparison between the parameters currently applied in KSATs oil detection service and quantitative parameters selected from literature describing several of the same characteristics.

1.3 Structure of the Thesis

The thesis contains 9 chapters including the introduction. Chapter 2 summarises some of the most important SAR principles, including the imaging geometry, resolution, the radar equation, speckle, multilook processing, wavelength, polarization and Noise-Equivalent Sigma-Zero (NESZ). Chapter 3 describes the fundamental concepts regarding ocean surface sensing by SAR. Chapter 4 presents the challenges related to marine oil spills, and discusses currently used and suggested classification parameters. Chapter 5 introduces the theory behind the SVM, in addition to an overview of several accuracy assessment methods. Chapter 6 describes the dataset used throughout the analysis, including the sensors, products and metadata available. Chapter 7 presents the method, while the results are presented and discussed in chapter 8. The final conclusions and future work are presented in chapter 9.

2

SAR Principles

SAR is a type of radar found on moving platforms such as aircrafts and spacecrafts. SAR transmits electromagnetic pulses and records the backscattered pulse. Important factors affecting the backscatter is the surface physical characteristics, electrical characteristics, satellite-surface geometry and the radar wavelength. SAR systems yields high resolution surveillance of the earth's surface using the microwave region. SAR sensors are also what is called active sensors, which means that the sensor both transmits and receives electromagnetic-pulses. Consequently, SAR works under all weather conditions and the system is independent of daylight [Campbell and Wynne, 2011].

2.1 Imaging Geometry

The geometry of a SAR system can be seen in Figure 2.1 and 2.2. The satellite is travelling in the azimuth direction, also called the along-track direction. Perpendicular to the azimuth direction is the range direction, this is the direction that the sensor is pointing. The slant range is the distance between the target and sensor, hence it is the sensors point of view. Sensor measurements are originally in slant-range, and have to be projected from slant range to ground range to obtain targets that are in the correct dimensions. The size of an image in range is called the swath width. The range varies between near-range and far-range, where near-range is the part of the swath closest to the satellite, and far-range is the part of the swath furthest away. The incidence angle is the

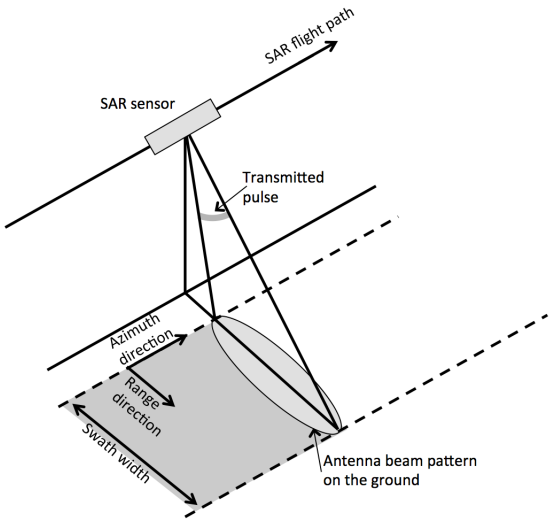

Figure 2.1: Imaging geometry of a SAR system. Figure from [Skrunes, 2014].

angle between the surface normal and the radar pulse, with the gracing angle as its compliment angle[Elachi and Van Zyl, 2006][Skrunes, 2014].

2.2 SAR Resolution

The advantage of using SAR compared to Real Aperture Radar (RAR) is the azimuth resolution. The sensor is the same in both cases, the difference is how the data is processed. SAR utilize the time delay between the backscattered echoes to separate objects in range, and the resolution in range is the minimum distance between two points on the surface which is still separable. The range resolution is mainly determined by the pulse length. The echo from one target have to be completely received before the head of the echo from a second target is received. If two echoes are received at the same time, they can't be distinguished [Elachi and Van Zyl, 2006]. The ground range resolution is given as

$$X_r = \frac{c}{2bsin\theta} = \frac{c\tau}{2sin\theta}, \tag{2.1}$$

where c is the speed of light, b is the bandwidth, τ is the pulse length and θ is the look angle. Equation 2.1 only applies under the assumption that the earth is flat. To obtain a good range resolution, it is desirable to use a short pulse. At the same time, a short pulse typically means a low energy pulse, which results in low Signal-to-Noise Ratio (SNR) [Elachi and Van Zyl, 2006]. To acquire a short pulse with high energy a frequency modulated chirp is used.

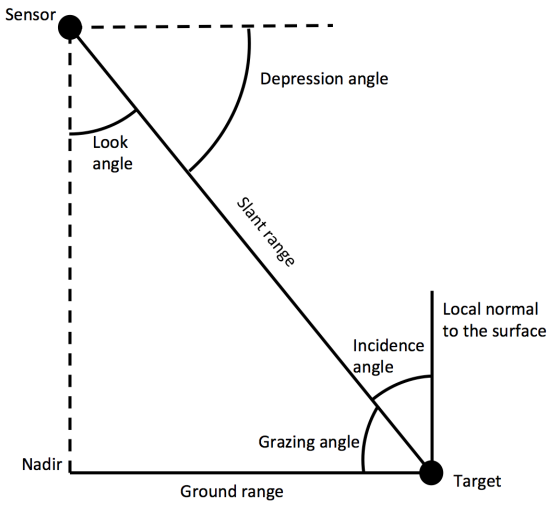

Figure 2.2: Important radar terms.

The instantaneous angular frequency of a chirp is described by

$$\omega = \omega_c + \frac{\Delta\omega}{\tau}t, \tag{2.2}$$

where ω_0 is the carrier angular frequency, $\Delta\omega$ is the change in angular frequency per unite time and t is the time. At transmission this pulse will have a large τ and consequently high energy. Then a matched filter can be used at reception to compress the pulse to a shorter pulse while keeping its energy [Elachi and Van Zyl, 2006].
The azimuth resolution for a RAR is

$$X_a = \frac{h\lambda}{Lcos\theta}, \tag{2.3}$$

where h is the height of the satellite, λ is the radar wavelength and L is the antenna length. This resolution is unacceptable for spaceborn radars, where the height typically is several hundred kilometres. In SAR, a larger antenna is synthesized using sophisticated signal processing techniques to increase the azimuth resolution. As long as the signal is coherently recorded and under the assumption that the object is static, an array of antennas is equivalent of a single moving antenna [Elachi and Van Zyl, 2006]. Now the length of the antenna is equal to the distance the satellite moves while the object is within the satellite beam. In Figure 2.3, this distance is equal to length B. By increasing the height of the sensor, the target stays within the beam for a longer period of time. Thus the length of the synthesized antenna increases. It turns out that these two factors cancel each other out, which makes the azimuth resolution independent of the height of the sensor [Elachi and Van Zyl, 2006]. The azimuth resolution

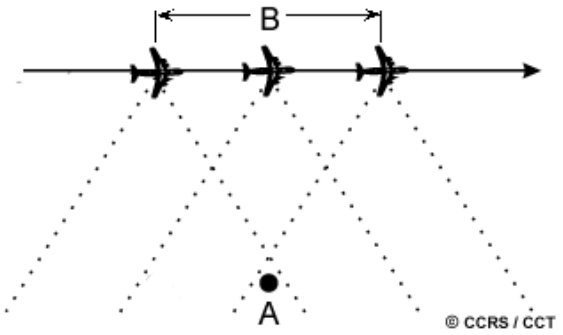

Figure 2.3: The principles of synthesizing a larger antenna to increase the azimuth resolution. Figure from [CCRS, 2007].

for a SAR radar is then

$$X_a = \frac{L}{2}. \tag{2.4}$$

2.3 The Radar Equation

The radar equation is the fundamental relationship between the radar, target and received signal, and is illustrated in Figure 2.4. Let P_t be the transmitted power from the antenna, the power, P_g, incident on an area, A_g, is then

$$P_g = \frac{P_t A_g G_t}{4\pi r^2}, \tag{2.5}$$

where G_t is the antenna gain, r is the distance from the sensor to object on the ground and the factor $(\frac{1}{4\pi r^2})$ is the attenuation of power as the wave propagates from the antenna to the ground [Elachi and Van Zyl, 2006, p. 241]. The received power at the antenna, P_r, from the ground is

$$P_r = \frac{P'_g G_g A_e}{4\pi r^2}, \tag{2.6}$$

where P'_g is the transmitted power from the ground, G_g is the gain from the ground and A_e is the effective antenna area. The ratio of the received power to the transmitted power is then

$$\frac{P_r}{P_t} = (\frac{P'_g G_g A_g}{P_g})\frac{GA_e}{(4\pi r^2)^2} = \sigma\frac{GA_e}{(4\pi r^2)^2}, \tag{2.7}$$

where σ is the Radar Cross Section (RCS). The RCS measures the backscatter recieved when an area/object is hit by a radar pulse. A high RCS value indicates

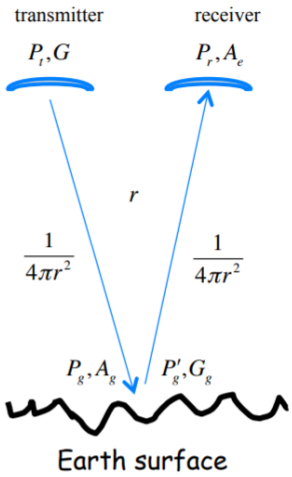

Figure 2.4: The principles of the derivation of the radar equation.

a strong return and a low RCS indicates a weak return. The effective antenna area can also be written as $A_e = \frac{G\lambda^2}{4\pi}$. Equation 2.7 then becomes [Wolff, 2017]

$$\frac{P_r}{P_t} = \sigma \frac{G^2\lambda^2}{4\pi^3 r^4}. \tag{2.8}$$

The radar equation is then

$$P_r = P_t \sigma \frac{G^2\lambda^2}{4\pi^3 r^4}. \tag{2.9}$$

2.4 Speckle

The radar wavelength is substantially smaller than the radar ground resolution, and one resolution cell on the ground contains several elementary scatterers with different scales and geometries. This implies that the radar receives multiple signals from scattering within one single pixel, making it possible to treat the magnitude and phase of the received signal as independent random variables. All of these different scattering events can produce constructive and destructive interference [Campbell and Wynne, 2011]. Constructive interference gives a strong return signal and a bright pixel, while destructive interference results in a weak return signal and a dark pixel.

This kind of noise is known as speckle noise, and is totally random. When processing SAR imagery, speckle introduces several problems such as loss of

crucial information and details in the image. The first step of removing speckle noise is understanding its statistical properties [Kuruoglu and Zerubia, 2004]. If the number of scatterers is large and fixed, the distribution of the real and imaginary parts of the received signal tends towards a normal distribution with zero mean and equal variances [Simard et al., 1998].
The magnitude of a complex signal is given by

$$A(t) = \sqrt{Z^2(t) + Y^2(t)}, \tag{2.10}$$

where Z(t) is the real part and Y(t) is the imaginary part of the signal. The magnitude of two normally distributed random variables with zero mean is Rayleigh distributed. The intensity of a single look complex image can be computed accordingly

$$I(t) = A^2(t). \tag{2.11}$$

The squared of a Rayleigh distribution is an exponential distribution, which is a special case of the gamma distribution, implying that the intensity is gamma distributed [Kuruoglu and Zerubia, 2004].

2.5 Multilook Processing

The problems induced by the presence of speckle creates the need for ways to reduce it. The most common way to do this is by multilooking. Multilooking can be done in the spatial domain by smoothing the image using average masks. It can also be done in the frequency domain, by creating several independent images by subdividing the frequency spectrum, and then merge these images into one final image [McCandless and Jackson, 2004]. The multilook operation can be described in the spatial domain as

$$< I >= \frac{1}{N} \sum_{i=1}^{N} I(i), \tag{2.12}$$

where N is the number of looks. Multilooking reduces speckle proportionally with $\sqrt{N}$ [Lee and Pottier, 2009], but at the cost of reduced resolution.

2.6 Wavelength

The wavelength of the transmitted SAR signal is given by

$$\lambda = \frac{1}{\bar{\nu}}, \tag{2.13}$$

where $\bar{\nu}$ is the radar frequency. The choice of the radar wavelength has several implications for the nature of the radar image, since it determines how the signal interacts with the surface [Campbell and Wynne, 2011]. By decreasing the wavelength of a signal, it will interact with smaller elements on the surface [Skrunes, 2014]. Radar signals are capable of penetrating solid matter, such as soil and vegetative cover. Penetration is assessed by the skin depth, which is the depth at which the magnitude of the signal is reduced to 1/e of the surface magnitude. The skin depth is a function of the wavelength, increasing with wavelength in the absence of soil moisture [Campbell and Wynne, 2011]. The primary subdivisions of the active microwave region can be seen in Table 2.1.

Band	Wavelength [cm]
P-band	77-107
UHF	30-100
L-band	15-30
S-band	7.5-15
C-band	3.75-7.5
X-band	2.40-3.75
Ku-band	1.67-2.40
K-band	1.18-1.67
Ka-band	0.75-1.18

Table 2.1: The primary subdivision of the active microwave region. Table adapted from [Campbell and Wynne, 2011, p. 212].

2.7 Polarization

An electromagnetic wave consists of both an electric and magnetic force field. For an electromagnetic wave propagating in free space, these two fields are orthogonal both to each other and the direction of propagation. The polarization of the electromagnetic wave is determined by the direction of the electric field [Elachi and Van Zyl, 2006]. In traditional SAR-systems, it is most common to use linearly polarized waves. This means that the electric field is confined to a plane along the direction of travel. The transmitted electromagnetic waves is usually Horizontally (H) and/or Vertically (V) polarized. The radar is also set to receive H and/or V polarized energy scattered from the ground. If the radar transmits and receives at one polarization, the radar is said to be at single-polarization mode. If the radar transmits at one polarization, but receives at both, the radar is set to dual-polarization mode [Campbell and Wynne, 2011]. This mode will produce two images, one co-polarized image (HH or VV), and one cross-polarized image (HV or VH). A radar in quad-polarization mode both

transmits and receives at V- and H-polarization. This produces four images, two co-polarized, and two cross-polarized images. The difference between the co- and cross-channels can be used to analyse the surface scattering mechanisms [Campbell and Wynne, 2011]. However quad-pol comes at a significant cost, with its technical limitations propagating through the SAR-system, putting constraints on the products. A radar in hybrid-polarization mode transmits a rightly circular wave and receives in both vertical and horizontal direction. Hybrid-pol mode retains most of the advantages with quad-pol mode, while avoiding its disadvantages [Raney, 2016].

2.8 Noise-Equivalent Sigma-Zero

The NESZ is the noise floor in a SAR system, and is a measure of the background noise. This means that if the signal strength approaches the NESZ, the signal will be corrupted and give a low SNR. For ocean areas the signal often approaches the NESZ in low backscatter regions such as oil spills, low wind areas, at large incidence angles and in cross-polarization channels [Skrunes, 2014]. The SNR is calculated by

$$SNR = \frac{Signal}{Noise} \rightarrow log(SNR) = log(Signal) - log(Noise). \tag{2.14}$$

The NESZ is given in Decibels (dB) and is lies as the point where SNR = 1, i.e. at the point where Signal = Noise. The SNR gives an indication of how corrupted the measured backscatter is by noise. If the radar backscatter approaches the NESZ, it is expected to be less separation between mineral oil and look-alikes, since the dark features contain most noise. A SNR analysis can help to identify and possibly exclude the data that are close to the noise floor.

3

Ocean Surface Sensing by SAR

Oceans cover three quarters of the earth, and to develop knowledge of this vast area is of major interest. Remote sensing, and especially SAR has proven to be a valuable tool for monitoring the ocean surface [Elachi and Van Zyl, 2006]. The high absorption and scattering from the ocean surface limits the ocean surveillance to the surface and the subsurface. Features such as surface waves, solitary waves, currents, fronts, eddies and near-surface wind affects the magnitude of the surface capillary and short gravity waves [Elachi and Van Zyl, 2006, p. 341]. This in turn is mainly responsible for the radar backscatter, making it possible to monitor the ocean surface. The radar backscatter is the product of the complex interaction between the transmitted signal and the dynamic ocean surface. This makes the return signal dependent on several factors such as the radar frequency, polarization, viewing geometry, the surfaces roughness characteristics, electrical properties and material composition [Holt, 2004, p. 25]. The wind-speed is an important parameter in ocean surface sensing. The magnitude of the wind-speed has to be large enough, such that the surface is sufficiently rough to make the strength of the backscattered signal larger than the noise floor of the sensor.

Many ocean surface characteristics can be retrieved from SAR imagery e.g ocean topography, Root Mean Square (RMS) wave heights, surface wind field, thermal fronts, eddies, internal waves and geoid measurements. SAR can

also be used for ship detection, sea ice features, deformation and movements alongside detection of biogenic slicks and oil spills [Elachi and Van Zyl, 2006, p. 341] [Skrunes, 2014, p. 35].

3.1 Surface Scattering

The scattering as an electromagnetic wave hits the sea surface is referred to as surface scattering, which is dependent on the surface geometry and dielectric properties. One of the most important factors determining surface scattering is roughness, and is statistically defined as the standard deviation relative to the mean flat surface [Elachi and Van Zyl, 2006, p. 203]. However, the roughness of a surface does not characterize its geometric properties alone. It is also important to know how each point on the surface is dependent on the points in the neighbourhood, i.e. the surface height autocorrelation function. By using the surface height autocorrelation function, it is possible to deduct the surface correlation length, which is defined as the distance between two points on the surface where the height of the two points are statistically independent. This is defined as the distance where the autocorrelation function has fallen below 1/e [Elachi and Van Zyl, 2006].

The relationship between surface roughness and the scattering of an electromagnetic wave are shown in Figure 3.1. For a perfectly smooth surface of infinite extent (Figure 3.1a), the entire radar wave will be reflected in the specular direction. Consequently, nothing will be scattered back to the sensor. As the surface gets rougher (Figure 3.1b), less radiation will scatter in the specular direction and more will scatter in other directions [Ulaby et al., 1982]. The scattering component in the specular direction is referred to as the coherent scattering component, while the scattering in other directions is often referred to as the incoherent scattering component. The coherent scattering component decreases as the surface roughness increases. When the surface gets very rough, the coherent scattering component gets negligible compared to the incoherent component. Thus for very rough surfaces(Figure 3.1c), the scattering can be approximated to be the same as from a Lambertian surface [Elachi and Van Zyl, 2006, p. 204].

If a surface is rough or smooth is decided by the Electromagnetic Wave (EM) wave which is incident on it, or more precisely the wavelength of the EM wave. A surface can be considered rough for one EM wave, and smooth for another. A commonly used criterion for deciding the roughness of a surface is the Rayleigh

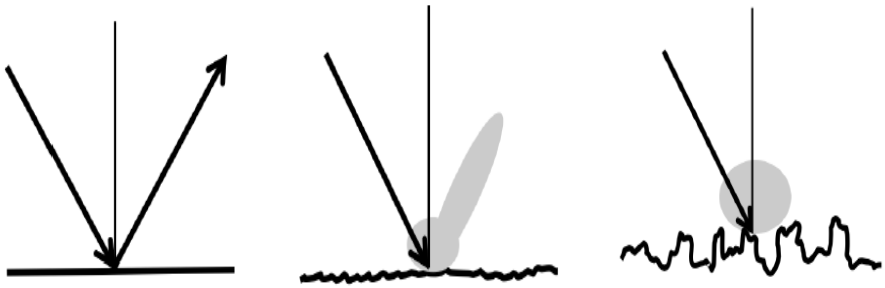

(a) Smooth surface. **(b)** Slightly rough surface. **(c)** Very rough surface.

Figure 3.1: Surface scattering for surfaces with different degree of roughness. Figure from [Skrunes, 2014]

criterion. A surface is considered rough if [Ulaby et al., 1982]

$$h_{rms} > \frac{\lambda}{8cos\theta}, \tag{3.1}$$

where h_{rms} is the RMS ocean wave height, λ is the radar wavelength and θ is the incidence angle.

3.2 Bragg Scattering

Bragg scattering is the scattering of electromagnetic waves on periodic surfaces, where the wavelength of the periodic surface are in the same range as the radar wavelength. This may lead to coherent addition of waves resulting in constructive interference. Constructive interference greatly increases the radar backscatter, and occurs when the following ratio is satisfied:

$$\lambda_B = \frac{\lambda_r}{2sin\theta}, \tag{3.2}$$

where λ_B is the surface wavelength, λ_r is the radar wavelength and θ is the incidence angle. The principles of Bragg scattering can be seen in Figure 3.2. The SAR backscatter from ocean surfaces are mainly due to Bragg scattering. For microwaves with typical SAR incidence angles (~18°-50°), capillary- and gravity waves generated by wind are generally continuously distributed in the scale (~cm) required to satisfy equation 3.2 [Holt, 2004].

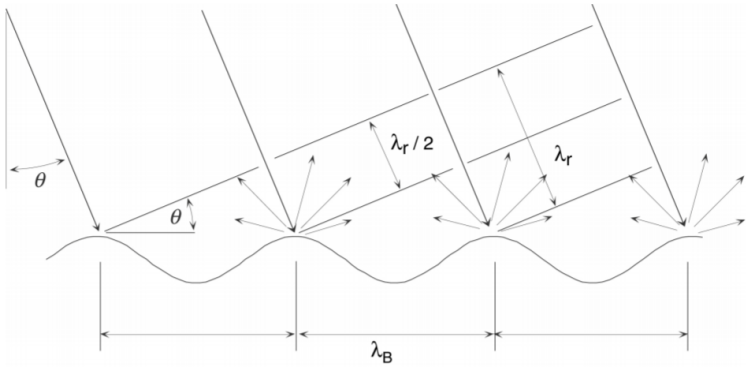

Figure 3.2: Illustration of Bragg scattering, figure from [Holt, 2004].

Tilted Bragg Scattering

The Bragg scattering model assumes that the ocean surface only consists of small gravity and capillary waves. In reality however, it consists of a vast diversity of waves, including waves on the scale of a few mm to a few hundred meters. Long waves usually combine with smaller Bragg waves to create two periodic structures on top of each other. The long waves alters the smaller Bragg waves by tilt modulation, hydrodynamic modulation and velocity bunching, which affects the radar backscatter [Holt, 2004]. This implies that the Bragg scattering model is insufficient for describing the radar backscatter over marine areas. The tilted Bragg scattering model accounts for the long waves. This model is further described in [Valenzuela, 1978].

4

Marine Oil Spills

Marine oil spills imposes a serious threat to the marine ecosystem. Oil is released into the marine environment regularly, both legally and illegally, and take place all around the world on a daily basis. This chapter gives an overview of the current status of oil released into the marine environment, alongside current remote sensing oil detection and the challenges associated with this. Parameters currently used by KSAT to distinguish between mineral oil and look-alikes is presented, in addition to other parameters proposed in scientific literature.

4.1 Anthropogenic and Natural Oil Releases

It is estimated that the amount of petroleum entering the oceans worldwide exceeds 1 300 000 metric tonnes yearly. About 46% of this comes from natural oil seepage (600 000 tonnes/year)[GESAMP, 2007]
[National Research Council, 2003]. Natural seeps occurs when crude oil seeps from the geological strata beneath the sea floor to the ocean surface. The seepage of crude oil into the marine environment tends to happen sporadically and at low rates. This gives the surrounding ecosystem time to adapt to release, although natural seepage constitutes vast volumes of oil into the marine environment [National Research Council, 2003].

Oil spills related to petroleum extraction is responsible for about 38 000 tonnes

of petroleum releases into the marine environment yearly, or about 5,4% of the total anthropogenic releases. Petroleum extraction means emissions originating from oil and gas exploration or production. Although the volume of petroleum released into the environment related to petroleum extraction is relatively small compared to the other sources, these spills often cause significant damage. They often occur in production fields and takes place as large spills or slow, continuous releases [National Research Council, 2003].

Petroleum transportation related releases amounts to 150 000 tonnes yearly, or about 21,4 % of the total anthropogenic releases. In the same manner as emissions from petroleum extraction, it produces large spills with a potentially serious impact on the environment. This type of releases can occur almost everywhere, which makes it difficult to anticipate the extent [National Research Council, 2003].

Petroleum consumption is by far the biggest source of man-made petroleum releases into the marine environment. Typical petroleum consumption sources are boat owners, non-tank vessels and runoff from paved urban areas. This category is responsible for 480 000 tonnes of petroleum released yearly, or about 68, 6% of the total release from anthropogenic sources worldwide. This type of releases mostly occurs as slow, chronic releases. A broad majority of the petroleum consumption takes place on land, and is transported by rivers or water streams into the ocean. This means that most of these releases happens in sensitive coastal water ecosystems [National Research Council, 2003].

4.2 Remote Sensing of Marine Oil Spills

Marine oil spills can be seen by SAR instruments as a dark feature in the ocean. Mineral oil films dampen the wind generated short-capillary waves, thus decreasing the SAR backscatter [Topouzelis, 2008]. Look-alikes denotes other phenomena known to cause similar SAR signatures as mineral oil, and often cause false detections. Classification of look-alikes and oil spills are of major importance for companies monitoring the ocean.

4.2.1 Look-alikes

An important part of remote sensing oil spill detection is to discriminate oil spills, which is illustrated in in Figure 4.1a, from other phenomena that produce dark features in a SAR image [Brekke and Solberg, 2005]. Examples are grease ice, current- and ship wakes, rain cells, internal waves, low wind areas, other man-made pollution (e.g. chemicals) and natural films [Espedal, 1999a]

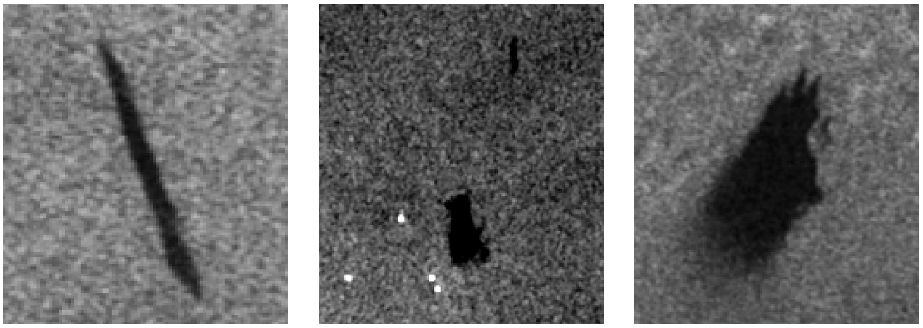

(a) (b) (c)

Figure 4.1: SAR imagery showing different detections. (a) Confirmed mineral oil. (b) Confirmed fish oil. (c) Nothing observed, dark feature assumingly created by atmospheric/oceanographic phenomena. All images are from the dataset used throughout this thesis. Contains modified Copernicus Sentinel data 2017, processed by KSAT.

[Espedal et al., 1998]. Natural films that can create dark features in SAR imagery includes algae, fish oil and vegetable oil. An example of a dark feature created by fish oil can be seen in Figure 4.1b. Look-alikes produced by natural films on the surface possesses many of the same properties as mineral oil, which makes it difficult to distinguish them [Brekke and Solberg, 2005]. Figure 4.1c pictures a look-alike that most likely originate from atmospheric- or oceanographic phenomena.

4.2.2 Present Classification of Marine Oil Spills

KSAT provides a near real-time oil spill detection service over maritime areas anywhere on earth twenty-four hours per day, seven days a week. The analysis is conducted by experienced operators that localizes, segments potential oil spills and give each dark feature a confidence category. They also identify possible sources using automatic information system data for vessels, alongside parameters like wind-speed and direction. They use the following parameters to describe and classify dark features

- Shape
- Outline
- Spatial texture
- Edges

- Weathering
- Contrast
- Presence of natural slicks in vicinity
- SAR derived wind information
- Area

The SAR derived wind information is estimated by the SARtool algorithm and the area is calculated based on the segmentation performed by the operator. The other parameters are set qualitatively by the operators based on their knowledge and experience. Then these parameters assessed to select a confidence category for the dark feature.

Shape

Different phenomena often cause dark features with different shapes, meaning that the shape of the dark feature is important for distinguishing between man-made slicks and look-alikes [Topouzelis, 2008] [Alpers et al., 2017] [Brekke and Solberg, 2005]. A feathered dark feature means that the the oil has been moved by currents or wind. An example of a feathered dark feature can be seen in Figure 4.2a. A feathered shape is also an indication that the dark feature is relatively old (hours/days) and is often created by anthropogenic oil spills. This kind of dark features are consequently referred to as high confidence detections [Alpers et al., 2017].

Angular winding dark features are characterized as two or more straight lines connected with an angle between them. The corners are typically sharp and are created by sudden changes in wind direction. See Figure 4.2b for illustration. Angular winding dark features are also referred to as high confidence detections, and are typically created by stationary sources such as platforms.

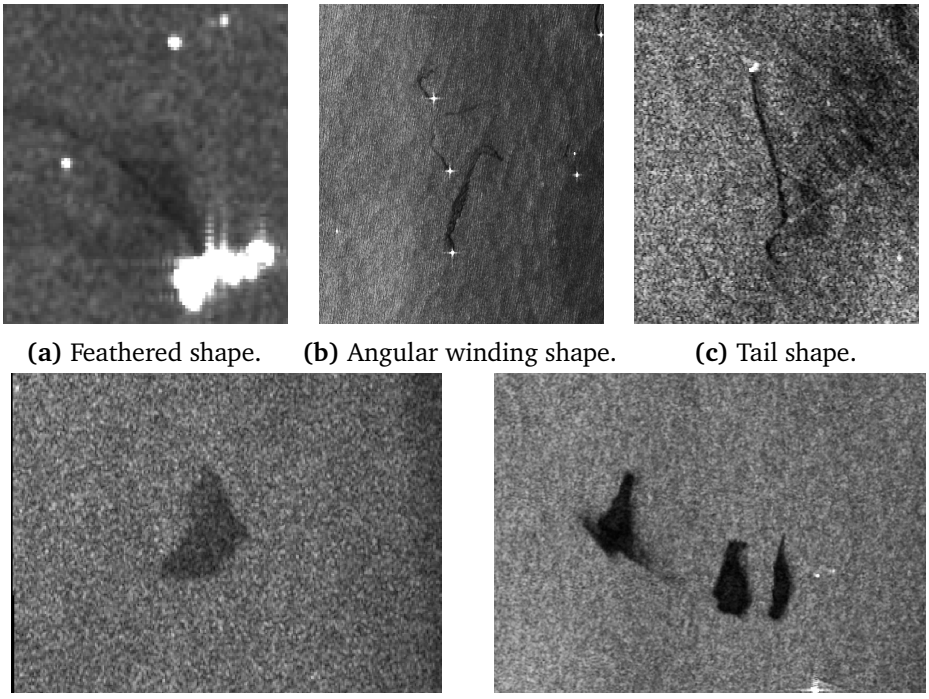

(a) Feathered shape. **(b)** Angular winding shape. **(c)** Tail shape.

(d) Patch shape. **(e)** Droplet shape.

Figure 4.2: Examples of different oil slick shapes. All images are from the dataset used throughout this thesis. RADARSAT-2 Data and Products © MacDONALD, DETTWILER AND ASSOCIATES LTD., 2015-2017 – All Rights Reserved.

Moving sources often create thin dark features, which are refereed to as tail-shaped dark features. The movement of the source alongside wind and currents decide the orientation of dark feature. Consequently, tail slicks can be straight or twisted depending on the movement of the source. Tail slicks are typically recent or ongoing emissions and are classified as high confidence detections [Alpers et al., 2017], although similar shapes can be produced by natural phenomena such as ship wakes, grease ice, current shears, internal waves and wind sheltering. An example of a tail shaped dark feature can be seen in Figure 4.2c.
Patch shaped dark features are circular in shape, and are often caused by natural phenomenona such as algae or ice. Hence this kind of dark feature are low confidence detections, although gas oil emissions can take this shape. A typical patch slick can be seen in Figure 4.2d.
A droplet shaped dark feature is a discontinuous dark feature, consisting of several smaller slicks [Hovland et al., 1994]. Droplet slicks usually originates from natural oil seepage. However, it can also originate from leaks from oil pipelines, wells and wrecks. This type of dark feature is classified as a high confidence slick, and an example can be seen in Figure 4.2e.

Outline

The outline of the dark feature describes whether the slick is continuous or fragmented.

Spatial Texture

The spatial texture of an object is the spatial information related to the pixels arrangement and the pixels relationship with the surroundings [Shi et al., 2008]. If the pixel intensity is relatively constant within an area, this area has little texture. On the other hand, if the variation in pixel intensity is large, the area has a lot of texture.

An important factor in explaining the expected difference in spatial texture is the varying viscosities of each material. Viscosity describes a fluids resistance to flow. Oil generally has a higher viscosity than look-alikes, and stays more concentrated. This dampens the capillary and small gravity waves on the surface, which results in a decreased RCS [Hovland et al., 1994][Del Frate et al., 2000]. In today's operational oil detection services, spatial texture is used as an aid to distinguish between oil spills and look-alikes. Look-alikes usually have small variance within the slick [Alpers et al., 2017], i.e. they are homogeneous. On the other hand, mineral oil have more variation within the slick and are inhomogeneous.

Edge

The edges of the dark objects are also commonly used for classification purposes [Brekke and Solberg, 2005]. This parameter is also affected by the viscosity of the material. A sharp edge means a large damping effect, which is caused by high viscosity materials. As a result, a sharp edge increases the possibility that the dark feature is oil. At the same time a diffuse edge implies that the dark feature most likely is a look-alike.

Contrast

The contrast of a dark feature to its surroundings is also a parameter used in the classification of oil and look-alikes. As it is with texture and edges, the contrast is also related to the damping effect created by the fluid present in the water. As discussed above, a slick containing oil is expected to have a larger damping than look-alikes [Hovland et al., 1994]. The relative damping effect of oil and look-alikes is reduced as the wind increases. Hence, when analysing

texture, edge and contrast of a slick for classification purposes, it is crucial to take the wind data into consideration. High wind reduces the relative damping effects of marine oil spills and look-alikes [Migliaccio et al., 2007], implying that a slick with little texture, diffuse edges and low contrast still can contain oil [Espedal, 1999b]. A dark feature that still remains connected at wind speeds above 7-8 m/s is likely to contain oil [Espedal, 1999a]. On the other hand, low wind decreases the contrast in the scene, which can also limit the separability between oil and look-alikes.

Weathering

The age of a slick greatly affects the shape, texture, edge and contrast of a dark feature. Old slicks are often referred to as weathered slicks, and present a much more complicated border structure than younger slicks due to their long exposure to the elements [Topouzelis, 2008]. The weathering process affects oil slicks and look-alikes differently. Look-alikes generally has smoother turnings, while oil slicks often develops thin tails that are fairly straight or slightly curved [Topouzelis, 2008].

Presence of Look-alikes in the Vicinity

In addition to analysing the slick, it is also important to analyse the surroundings. If the slick is located in an area with many other look-alikes present, the probability of the slick being of natural origin increases.

4.2.3 Other Parameters Proposed for Discrimination of Mineral Oil and Look-alikes

Parameters used for classification of mineral oil can in general be divided into three categories [Topouzelis et al., 2009]

1. Geometrical descriptors (e.g. area, perimeter and compactness)

2. Physical behaviour of oil (e.g. Damping ratio, backscatter and coefficient of variation)

3. Context of oil spill (e.g. Number of dark features in the image and presence of ships)

[Topouzelis et al., 2009] summarises several research papers trying to classify mineral oil, and presents 25 of the most commonly used parameters, Table

4.1 shows a selection of these parameters. Many of the parameters currently used in KSATs oil detection service are qualitative subjective parameters. On the other hand, the parameters presented in the following sections describes several of the same dark feature characteristics as KSATs parameters, just in a quantitative objective manner.

Feature	[Del Frate et al., 2000]	[Solberg et al., 1999]	[Fiscella et al., 2000]
Width/length	Spreading	Slick width	
Area	x	x	x
Perimeter	x		x
Compactness			x
Shape descriptor		First Hu moment	Form factor
Coefficient of variation			x
Damping ratio			x

Table 4.1: A selection of some of the parameters used for classification of mineral oil, alongside articles that have used them. Table adapted from [Topouzelis et al., 2009].

Geometrical Descriptors

Geometrical descriptors are used to describe regions in an image, and the simplest geometrical descriptors are width and length. The area of a region is the number of pixels in that region. It can also be converted to other units by knowing the pixel size [Gonzalez and Woods, 2012]. The perimeter is the length of the boundary around a region. By combining these two parameters the compactness of the region is obtained, which is defined as [Nixon and Aguado, 2002]

$$C = \frac{4\pi Area}{Perimeter^2}. \tag{4.1}$$

Compactness measures the relationship between the area of a region and the boundary that encloses this object. For circular shapes the compactness approaches one, $\frac{\pi}{4}$ for a square and zero for highly complex shapes. Compactness is often referred to as the circularity ratio [Gonzalez and Woods, 2012].

Hu Invariant Moments

In 1962 Ming-Kuei Hu presented the theory of two-dimensional moment invariants for planar geometric figures [Hu, 1962], these moments are often referred to as Hu invariant moments. These are regularly used in visual pattern recognition tasks due to their ability to recognize geometrical patterns, in addition to being invariant to image translation, scale change, mirroring and rotation [Gonzalez and Woods, 2012]. [Brekke, 2007] identified Hu's first moment as useful for separating dark features with thin, piecewise elongated

shapes from dark features with other arbitrary shapes. For an 2-D image f(x,y) with dimensions M × N, the moment of order (p + q) is defined as [Gonzalez and Woods, 2012]

$$\hat{m}_{pq} = \sum_{x=0}^{M-1} \sum_{y=0}^{N-1} x^p y^q f(x,y). \tag{4.2}$$

The central moment of order (p+q) is defined as [Gonzalez and Woods, 2012]

$$\mu_{pq} = \sum_{x=0}^{M-1} \sum_{y=0}^{N-1} (x-\bar{x})^p (y-\bar{y})^q f(x,y), \tag{4.3}$$

$$\text{where } \bar{x} = \frac{\hat{m}_{10}}{\hat{m}_{00}} \text{ and } \bar{y} = \frac{\hat{m}_{01}}{\hat{m}_{00}}.$$

The normalized central moments are then defined as [Gonzalez and Woods, 2012]

$$\eta_{pq} = \frac{\mu_{pq}}{\mu_{00}^{\gamma}}, \quad \text{where } \gamma = \frac{p+q}{2} + 1 \tag{4.4}$$

and η_{pq} is the normalized central moment of order (p+q). From these normalized central moments, seven Hu moments can be derived. These are given as [Gonzalez and Woods, 2012]

$$\hat{\phi}_1 = \eta_{20} + \eta_{02} \tag{4.5}$$

$$\hat{\phi}_2 = (\eta_{20} - \eta_{02})^2 + 4\eta_{11}^2 \tag{4.6}$$

$$\hat{\phi}_3 = (\eta_{30} - 3\eta_{12})^2 + (3\eta_{21} - \eta_{03})^2 \tag{4.7}$$

$$\hat{\phi}_4 = (\eta_{30} + \eta_{12})^2 + (\eta_{21} + \eta_{03})^2 \tag{4.8}$$

$$\begin{aligned}\hat{\phi}_5 = {} & (\eta_{30} - 3\eta_{12})(\eta_{30} + \eta_{12}) \left[(\eta_{30} + \eta_{12})^2 - 3(\eta_{21} + \eta_{03})^2\right] \\ & + (3\eta_{21} - \eta_{03})(\eta_{03} + \eta_{21}) \left[3(\eta_{12} + \eta_{30})^2 - (\eta_{03} + \eta_{21})^2\right]\end{aligned} \tag{4.9}$$

$$\begin{aligned}\hat{\phi}_6 = {} & (\eta_{20} - \eta_{02}) \left[(\eta_{30} + \eta_{12})^2 - (\eta_{21} + \eta_{03})^2\right] \\ & + 4\eta_{11}(\eta_{30} + \eta_{12})(\eta_{03} + \eta_{21})\end{aligned} \tag{4.10}$$

$$\begin{aligned}\hat{\phi}_7 = {} & (3\eta_{21} - \eta_{03})(\eta_{30} + \eta_{21}) \left[(\eta_{30} + \eta_{21})^2 - 3(\eta_{21} + \eta_{03})^2\right] \\ & + (3\eta_{12} - \eta_{30})(\eta_{21} + \eta_{03}) \left[3(\eta_{30} + \eta_{12})^2 - (\eta_{21} + \eta_{03})^2\right]\end{aligned} \tag{4.11}$$

Parameters Related to the Physical Behaviour of Oil

Parameters related to the physical behaviour of oil is connected to the RCS of the dark feature. The damping ratio is the ratio between the mean value of the dark feature and the surrounding sea [Gade et al., 1998]. The coefficient of variation is the ratio between the standard deviation and the mean of the dark feature [Solberg et al., 1999].

4.3 Log-Cumulants

In classical statistics, moments and cumulants are often used to describe the statistical distribution of parameters. Recently, it's been proposed to use log-moments and log-cumulants instead.

4.3.1 Radar Texture

The randomness of a radar image is often described by two unrelated factors, speckle and radar texture. As described above, speckle is caused by constructive and destructive interference, and leads to the characteristic grainy appearance of SAR imagery. Speckle is assumed to have a Gaussian distribution in homogeneous regions. However, perfect homogeneous regions rarely exists. Radar texture describes this natural variation in radar cross section. It's important to distinguish between spatial texture, and radar texture. [Skrunes, 2014]. Quite a few statistical models exists that accounts for both Speckle and texture. These models are often based on assuming that texture is a non-Gaussian scattering vector, or that texture is a separate random variable [Anfinsen and Eltoft, 2011].

4.3.2 Classical Statistics

Accurate estimation of the Probability Density Function (PDF) of data is crucial when working with classification problems. If a random phenomenon is described by a PDF, a Characteristic Function (CF) is often introduced. The CF is defined as the Fourier transform of the PDF [Nicolas and Anfinsen, 2002]

$$\Phi_X(v) = \mathcal{F}[p(u)](v) = \int_{-\infty}^{\infty} e^{jvu} p_X(u) du, \tag{4.12}$$

Where $\mathcal{F}$ denotes the Fourier transform, $p_X(u)$ is the PDF of the random variable X and $\Phi_X(v)$ is the CFCF of the random variable X. The second CF is

defined as [Nicolas and Anfinsen, 2002]:

$$\Psi_X(v) = log(\Phi_X(v)), \tag{4.13}$$

where $\Psi_x(v)$ denotes the second CF. Then the moments and cumulants of order v can be attained by derivation of the first and second CF. The derivation of the moments and cumulants is based on the Fourier transform, which is poorly adapted to the analysis of pdfs defined in $\mathbb{R}^+$, in the sense that the analytic expressions of CFs might become impossible to formulate. [Nicolas, 2002](translated in [Nicolas and Anfinsen, 2002]) proposes to deal with this problem by introducing second kind statistics, in which the Fourier transform is replaced by the Mellin transform.

4.3.3 Mellin Transform and Log-Cumulants

Let X be a real and positive random variable, or in other words X $\in \mathbb{R}^+$. This implies that $p_X(u)$ also is defined for u $\in \mathbb{R}^+$, then the first CF of second kind is defined as [Nicolas and Anfinsen, 2002]

$$\phi_X(s) = \mathcal{M}[p_X(u)](s)] = \int_0^\infty u^{s-1} p_X(u) du, \tag{4.14}$$

where $\mathcal{M}$ denotes the Mellin transform. Since $p_X(u)$ is a PDF, the second kind CF satisfies the property [Nicolas and Anfinsen, 2002]

$$\phi_X(s)|_{s=1} = 1. \tag{4.15}$$

The second kind moments are defined as [Nicolas and Anfinsen, 2002]

$$m_v = \left.\frac{d^v \phi_X(s)}{ds^v}\right|_{s=1} = \int_0^\infty (\log(u))^v p_X(u) du. \tag{4.16}$$

The second kind moments is often referred to as log-moments. The second characteristic function of the second kind is defined accordingly [Nicolas and Anfinsen, 2002]

$$\psi_X(s) = log(\phi_X(s)). \tag{4.17}$$

The second kind cumulants is defined in the same manner as classical cumulants, leading to the definition of second kind log-cumulants of order v [Nicolas and Anfinsen, 2002]:

$$\kappa_{X(v)} = \frac{d^v \psi_X(s)}{ds^v}. \tag{4.18}$$

Then according to [Nicolas and Anfinsen, 2002] the three first log-cumulants can be written accordingly

$$\kappa_1 = m_1, \tag{4.19}$$

$$\kappa_2 = m_2 - m_1^2, \tag{4.20}$$

$$\kappa_3 = m_3 - 3m_1m_2 + 2m_1^3. \tag{4.21}$$

4.3.4 Sample Log-Cumulants

The sample log moments of order ν, can be calculated using the sample mean estimator [Anfinsen and Eltoft, 2011]:

$$m_\nu\{X\} = \frac{1}{N}\sum_{i=1}^{N}\log(X_i)^\nu, \tag{4.22}$$

where N is the number of samples. The log-cumulants are then defined in the same manner as the theoretical log cumulants defined in equation 4.19, 4.20 and 4.21, namely

$$\kappa_1\{X\} = m_1\{X\}, \tag{4.23}$$

$$\kappa_2\{X\} = m_2\{X\} - m_1\{X\}^2, \tag{4.24}$$

$$\kappa_3\{X\} = m_3\{X\} - 3m_1\{X\}m_2\{X\} + 2m_1\{X\}^3, \tag{4.25}$$

where $\kappa_1\{X\}$, $\kappa_2\{X\}$ and $\kappa_3\{X\}$ represents the mean, variance and skewness in the log-domain, respectively.

4.3.5 Previous Work using Log-Cumulants

[Anfinsen and Eltoft, 2011] first proposed to use the κ_2-κ_3 space to find the distribution of texture in a given region for multilooked polarimetric data.

[Skrunes et al., 2015b] then took a look at the possibility to use log-cumulants for classification of marine oil and look-alikes. The data consisted of scenes acquired from RADARSAT-2 (RS2) and TerraSAR-X which had a temporal distance of only 24 minutes. The RS2 and TerraSAR-X scene had a resolution

of 5.2 × 7.6m and 1.2 × 6.6m (range × azimuth), respectively. κ_2 and κ_3 from single channel (VV-channel from quad polarization data) single-look intensity data was explored. Especially κ_2 was found useful in discriminating between mineral oil and look-alikes.

The potential for classification of marine oil spills and look-alikes using log-cumulants was further explored in [Skrunes et al., 2015a]. Five scenes acquired from RS2 in fine quad polarization mode were investigated, the scenes had a pixel size of $4.73 \times (4.71 - 5.12)$m (range × azimuth) [Skrunes et al., 2015a]. When normalized to the sea state, a clear separation between simulated look-alikes and mineral oil was observed both κ_1 and κ_2 when utilizing multiple channels and single-channel from the quad-polarization data.

The potential of using log-cumulants for classification of mineral oil and look-alikes were further tested in a preliminary study to this thesis. The log-cumulants was calculated for low resolution and single-polarization ScanSAR scenes acquired by RS2. Neither of the log-cumulants were found to have a clear separation between mineral oil and look-alikes. Generally, mineral oil was found to have larger damping and less internal variation than look-alikes. The log-cumulants were also normalized with regard to the sea state in an attempt to account for the different characteristics of the dark features. This didn't increase the separation noteworthy. κ_3 was found to have the least classification potential, which led to a more extensive analysis of κ_1 and κ_2. κ_1 was found to decrease with incidence angle, and not be that dependent on neither wind or size. κ_2 was found to have a low dependency on incidence angle, wind speed and slick size. Including only mid-range incidence angles (30°-40°) proved to give a better separation in the normalized $\kappa_1 - \kappa_2$ space.

Neither κ_1 or κ_2 proved to give a clear separation between the classes, although κ_1 gave a better separation than κ_2. The coarse resolution of the RS2 ScanSAR scenes (50 × 50m) seems to remove much of the separation previously found between the classes in κ_2-space. Thus producing an overall inaccurate classification. The potential for using log-cumulants to separate between mineral oil and look-alikes will be further tested in this thesis.

5 Classification

Classification refers to the categorization of objects based on their features. The objective is to obtain features that separates the objects such that they can be classified correctly. The features describing an object form the feature vector [Theodoridis and Koutroumbas, 2008]

$$\boldsymbol{x} = [x_1, x_2, ..., x_l]^T, \tag{5.1}$$

where T denotes the transposed and l is the number of features. The classification systems task is to divide the feature space into regions that correspond to each class. When a classifier utilizes a priori known information, it is referred to as supervised learning [Theodoridis and Koutroumbas, 2008]. Another approach for many classification algorithms is to look for natural groups in the dataset, without the use of training data, this is referred to as unsupervised learning or clustering [Theodoridis and Koutroumbas, 2008].

5.1 Support Vector Machine

SVM is a relatively new classification technique, which was introduced in the middle of the 1990s. Experiments have shown that the SVM, compared to neural networks, has a simpler structure, improved performance and a better generalization ability. SVM also proves to be very efficient in solving problems with a small dataset containing high dimensional feature vectors [Yan et al., 2009].

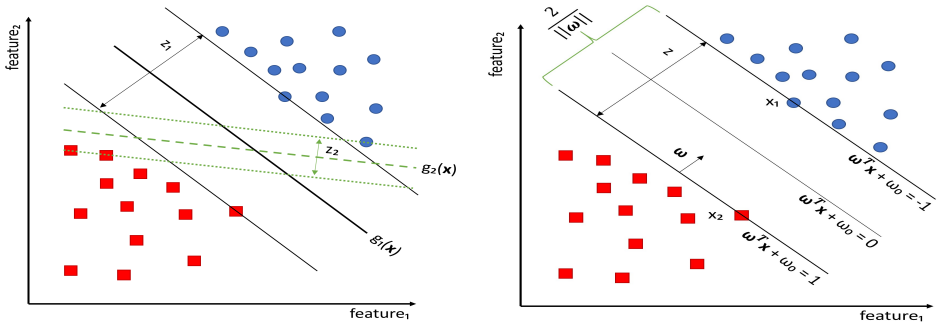

Figure 5.1: Examples demonstrating the idea behind a linear SVM. (a) Two hyperplanes separating two separable classes, adapted from [Theodoridis and Koutroumbas, 2008]. (b) Visualization of how the margin is calculated.

5.1.1 Linearly Separable Classes

A support vector machine classifier can both be linear or non-linear. Under the assumption that the classes are linearly separable, the overall goal is to design a hyperplane on the form [Theodoridis and Koutroumbas, 2008]

$$g(\boldsymbol{x}) = \boldsymbol{\omega}^T \cdot \boldsymbol{x} + \omega_0 = 0, \tag{5.2}$$

that classifies all the training vectors correctly, where g(x) is a linear discriminant function, $\boldsymbol{x}$ refers to the training data vector, $\boldsymbol{\omega}$ is the weight vector and ω_0 is the bias. The direction of the hyperplane is determined by $\boldsymbol{\omega}$, while its position in space is determined by ω_0. This solution is in general not unique and the SVM tries to find the best possible solution. It does this by introducing the margin, which is two separate and parallel lines that lies between the decision boundary and the data points [Theodoridis and Koutroumbas, 2008]. The optimal line is the decision boundary that maximizes the margin. Equivalently, the optimal hyperplane is the the one that maximizes the distance between the hyperplane and the support vectors, with support vectors being the data points that lie on the margin. Figure 5.1a shows two linearly separable classes separated by two different hyperplanes. Many other classifiers (e.g. neural networks) are only interested in finding a hyperplane that separates the classes, and could as a consequence end up with producing the stapled hyperplane in Figure 5.1a. However, the full-lined hyperplane has a greater margin and performs much better when introduced to unknown data, i.e. it generalizes better [Theodoridis and Koutroumbas, 2008]. The first step in finding the solution that maximizes the margin is to express it in terms of ω. By choosing the appropriate scaling factor the hyperplane can be defined such that all points on the margin is 1 or -1, see Figure 5.1b for illustration, thus leading to the

property [Theodoridis and Koutroumbas, 2008]

$$\begin{aligned} \boldsymbol{\omega}^T \boldsymbol{x} + \omega_0 \geq 1, \quad \forall \boldsymbol{x} \in \omega_1 \\ \boldsymbol{\omega}^T \boldsymbol{x} + \omega_0 \leq -1, \quad \forall \boldsymbol{x} \in \omega_2, \end{aligned} \tag{5.3}$$

where ω_1 and ω_2 denotes the membership function for class 1 and 2, respectively. Then by vector subtraction, the distance between the points on the margin can be expressed as

$$\begin{aligned} & (\boldsymbol{\omega}^T \cdot \boldsymbol{x_1} + \omega_0) - (\boldsymbol{\omega}^T \cdot \boldsymbol{x_2} + \omega_0) = 2 \\ \Rightarrow & \boldsymbol{\omega}^T (\boldsymbol{x_1} - \boldsymbol{x_2}) = 2 \\ \Rightarrow & \frac{\boldsymbol{\omega}^T}{||\boldsymbol{\omega}||} (\boldsymbol{x_1} - \boldsymbol{x_2}) = \frac{2}{||\boldsymbol{\omega}||} \\ \Rightarrow & z = (\boldsymbol{x_1} - \boldsymbol{x_2}) \hat{\omega} = \frac{2}{||\boldsymbol{\omega}||}, \end{aligned} \tag{5.4}$$

where z is the margin as defined in Figure 5.1b and $\hat{\omega}$ denotes the unit vector in ω-direction. It turns out that it's easier to minimize the equivalent cost function

$$J(\boldsymbol{\omega}, \omega_0) \equiv \frac{1}{2} ||\boldsymbol{\omega}||^2, \tag{5.5}$$

than it is to maximize Equation 5.4. The optimization task can then be formulated accordingly, calculate $\boldsymbol{\omega}$ and ω_0 such that the cost function is minimized, with the constraints defined in Equation 5.3
[Theodoridis and Koutroumbas, 2008]. This is a quadratic optimization task subject to a set of linear inequality constraints, which can be solved using Karush-Kuhn-Tucker conditions in combination with Lagrange multipliers λ_i. This will provide a global and unique minima and it gives the following solutions

$$\boldsymbol{\omega} = \sum_{i=1}^{N} \lambda_i y_i \boldsymbol{x}_i \tag{5.6}$$

$$\sum_{i=1}^{N} \lambda_i y_i = 0. \tag{5.7}$$

Where y_i is a vector containing the class labels defined as

$$y_i = \begin{cases} -1, \ \forall \quad \boldsymbol{x} \in \omega_1 \\ 1, \quad \forall \quad \boldsymbol{x} \in \omega_2 \end{cases}$$

5.1.2 Nonseparable Classes

For non-separable classes, the approach is a bit different than described above. The training vectors can now be divided into three categories
[Theodoridis and Koutroumbas, 2008]:

1. Training vectors that are correctly classified and lie outside the margin i.e. $y_i(\boldsymbol{\omega}^T\boldsymbol{x} + \omega_0) \geq 1$.

2. Training vectors that are correctly classified but lie inside the margin i.e. $0 \leq y_i(\boldsymbol{\omega}^T\boldsymbol{x} + \omega_0) < 1$.

3. Training vectors that are misclassified i.e. $y_i(\boldsymbol{\omega}^T\boldsymbol{x} + \omega_0) < 0$

To be able to treat all of these categories under a single constraint, the slack variable ξ is introduced, which is defined accordingly [Theodoridis and Koutroumbas, 2008]

$$\xi_i = \begin{cases} 0, & \forall\ y_i(\boldsymbol{\omega}^T\boldsymbol{x} + \omega_0) \geq 1 \\ (0,1], & \forall\ 0 \leq y_i(\boldsymbol{\omega}^T\boldsymbol{x} + \omega_0) < 1 \\ (1,\infty) & \forall\ y_i(\boldsymbol{\omega}^T\boldsymbol{x} + \omega_0) < 0 \end{cases}$$

Then the constraint can be defined accordingly [Theodoridis and Koutroumbas, 2008]

$$y_i(\boldsymbol{\omega}^T\boldsymbol{x} + \omega_0) \geq 1 - \xi_i. \tag{5.8}$$

Now the concept becomes similar to the separable classes case. The overall goal is now to make the margin as large as possible, with the constraint that the number of training vectors with $\xi > 0$ should be minimized. The cost function can then be mathematically formulated as [Theodoridis and Koutroumbas, 2008]

$$J(\boldsymbol{\omega}, \omega_0, \boldsymbol{\xi}) = \frac{1}{2}||\boldsymbol{\omega}||^2 + G\sum_{i=1}^{N}\xi_i, \tag{5.9}$$

where G is some positive constant that controls the relative size of the two terms in the equation. Then the cost-function can be minimized with the constraints defined in equation 5.8, in the same manner as in the separable classes case, namely using the Karush-Kuhn-Tucker conditions alongside Lagrangian multipliers.

5.2 Accuracy Assessment

The accuracy of a classification result is the correctness i.e. it measures the agreement between the correct and classified objects [Campbell and Wynne, 2011]. Compilation of the confusion matrix is required for any serious study of accuracy [Campbell and Wynne, 2011]. It does not only tell the overall error but also the misclassifications for each class. An example of a confusion matrix can be seen in Figure 5.2, where a,b,c and d can be both

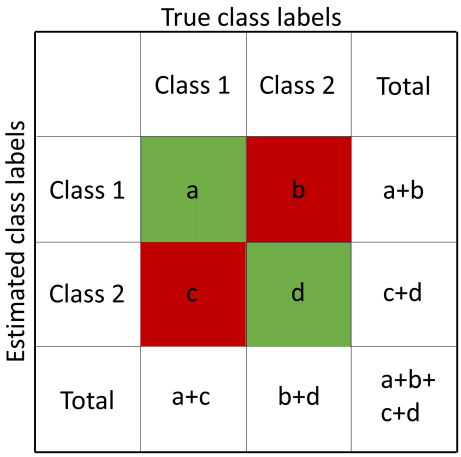

Figure 5.2: The confusion matrix, green areas denote correctly classified objects, while red areas denotes misclassifications.

the percentage and number of values [Campbell and Wynne, 2011]. The y- and x-axis denotes the classified class labels and true class labels, respectively. The rows sum to the total amount of objects assigned to a class, while the columns sum to the true number of objects belonging to that class. The most intuitive and most used accuracy descriptor is the overall Classification Accuracy (CA), which can be expressed as [Campbell and Wynne, 2011]

$$\Pi = \frac{a+d}{a+b+c+d}, \tag{5.10}$$

where a, b, c and d are as defined in Figure 5.2. The overall CA is the relationship between the proportion of correctly classified objects versus the total amount of objects. Overall accuracy is the simplest form of accuracy assessment, and it quantifies the relative effectiveness of the classification. However, it does not take into account the possibility of the agreement occurring by chance. Hence it does not contain enough information for it to solely determine the performance of the classifier. To properly assess the result fo a classification, the overall accuracy has to be combined with the confusion matrix [Campbell and Wynne, 2011].

$\bar{\kappa}$ measures the difference between the overall accuracy and the accuracy that could occur by chance. This is an important distinction from the overall accuracy, since not all agreement can be attributed to the success of the classification. $\bar{\kappa}$ is defined as [Cohen, 1960]

$$\bar{\kappa} = \frac{observed - expected}{1 - expected}, \tag{5.11}$$

where observed denotes the overall accuracy, while expected represent the contribution of chance agreement to the observed overall accuracy. Expected can be calculate accordingly

$$expected = \left[\left(\frac{a+b}{a+b+c+d} \cdot \frac{a+c}{a+b+c+d}\right) + \left(\frac{c+d}{a+b+c+d} \cdot \frac{b+d}{a+b+c+d}\right)\right]. \tag{5.12}$$

$\bar{\kappa}$ ranges from -1 to 1, where 0 represents the amount of agreement that can be expected from random chance, while 1 indicates perfect agreement, and -1 implies zero agreement. An interpretation of $\bar{\kappa}$ is presented in Table 5.1.

$\bar{\kappa}$	**Strength of agreement**
<0.20	Poor
0.21-0.40	Fair
0.41-0.60	Moderate
0.61-0.80	Good
0.81-1.00	Very good

Table 5.1: Interpretation of $\bar{\kappa}$ value. Table adapted from [Marston, 2009].

6

Data Collection

A challenge when working with remote sensing of oil spills is the lack of data available. It's difficult to know exactly when and where oil spills take place. The spills are also located at remote places, and it is expensive to verify the oil spills and look-alikes. For this thesis, KSAT provided access to their database along with feedback reports from the European Marine Safety Agency (EMSA). KSAT provides daily oil spill detection for EMSA through the Clean Sea Net (CSN) service [KSAT, 2017]. When a dark feature is detected, national authorities receive a pollution alert from EMSA. Then the national authorities can decide how they want to respond to the suspected oil spills. They often send patrol vessels or aircrafts to investigate and verify the oil spill. Approximately 30 coastal states use this service and over 2000 images are ordered and analysed each year [EMSA, 2017].
KSAT acquires SAR images and delivers them to EMSA, along with detailed analysis of possible oil spills, sources and confidence levels. All of this within 30 minutes of acquisition.

6.1 SAR Sensors

RS2 is a SAR sensor which has been operational since 2007, and offers scenes with a wide variety of characteristics. RS2 uses C-band and can deliver scenes with a resolution from 1 to 100 meters, with a coverage up to 250 000 km^2 and can deliver single-, dual- and quad-polarization data [Dettwiler et al., 2008a]

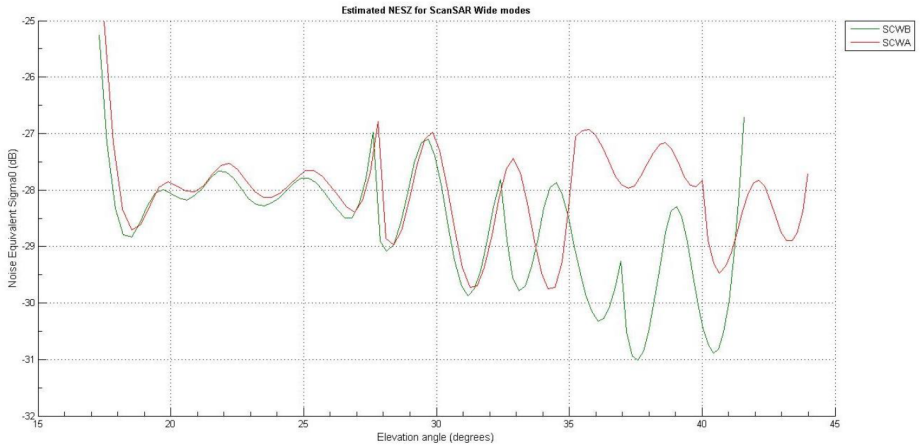

Figure 6.1: The estimated NESZ for ScanSAR Wide modes for RS2. Figure from [Dettwiler et al., 2016]

[Dettwiler et al., 2016]. RS2 has 20 different beam-modes, among these are stripmap, ScanSAR and spotlight mode. Stripmap mode is single beam mode, which has a constant beam elevation and profile. In spotlight mode, the antenna is steered at a fixed point on the ground, increasing the azimuth resolution. In ScanSAR mode the antenna elevation angle changes corresponding to several subswaths [Dettwiler et al., 2008b]. This mode provides a huge coverage, but at the cost of resolution in the azimuth direction. The estimated NESZ for ScanSAR Wide modes can be seen in Figure 6.1, which shows how dependent the NESZ is on elevation angle, which is the same as incidence angle for a flat surface. A typical NESZ given for ScanSAR wide multilooked products are -28.5 ± 2.5 dB [Dettwiler et al., 2016].

Sentinel-1 (S1) is the first satellite in the proposed fleet of satellites in Europe's Copernicus programme, and its objective is to provide an all-weather, day and night surveillance of the earth's surface. S1 is a constellation of two satellites, namely Sentinel-1A (S1A) and Sentinel-1B (S1B), which is orbiting 180° apart. The S1 constellation utilizes C-band and offers the following modes: Interferometric Wide-swath (IW), wave-mode, strip map and Extra Wide Swath (EW) [ESA, 2017b]. IW mode has a swath width of 250 km [ESA, 2017c], and has similarities to the more traditional ScanSAR mode. Both modes steers the beam in range, which trades resolution for range coverage. The main difference between IW and ScanSAR mode is that IW mode utilizes the Terrain Observation with Progressive Scans SAR (TOPSAR) technique. This means that in addition to steering the beam in range, the beam is also steered in azimuth between each burst. Thus avoiding azimuth artifacts like scalloping, in addition to ensuring homogeneous image quality throughout the swath [De Zan and Guarnieri, 2006]. This leads to a nearly uniform SNR, with a

maximum NESZ of -22 dB [ESA, 2017c].

All scenes analysed in this thesis are acquired by S1A, S1B or RS2. The modes used are ScanSAR Wide (RS2), ScanSAR Narrow (RS2), IW (S1) and EW (S1), which all covers huge areas. The majority of the scenes are captured by ScanSAR Wide and IW, and an overview of the properties of these modes is provided in Table 6.1. There are two type of products available in this dataset for S1 data, namely Ground Range Detected Medium (GRDM) and Ground Range Detected High (GRDH). The main difference between the two product types is the amount of multilooking performed. S1-GRDM and S1-GRDH products are multilooked 22 × 5 and 5 × 1 (range × azimuth), respectively. This leads to a pixel spacing of 40m × 40m (range × azimuth) for S1-GRDM products and 10 × 10m for S1-GRDH products. S1-GRDM and RS2 ScanSAR data are acquired from KSAT, while S1-GRDH products are acquired from [ESA, 2018].

Properties/satellite	**RS2**	**S1**
Mode	ScanSAR Wide	IW
Product type	SAR Georeferenced Fine	GRDM and GRDH
Swath	500 km	250 km
Resolution (range × azimuth)	50 × 50m	10 x 10m or 40 x 40m
Incidence angle	20°-49°	30°-45°
NESZ [dB]	-28.5 ± 2.5	-22
Polarization	VV or HH	VV, VV/VH or HH/HV

Table 6.1: Overview of the modes primarily used in this thesis and their properties

6.2 Dataset

The data provided by KSAT for this project spans across the time from 01/08/2015-31/12/2017 and originate from the CSN service. The selection of data is based on feedback reports describing each checked spill reported from KSAT to EMSA during the period defined above. Most importantly, the reports contain in-situ information about each dark feature. The feedback reports contains 1961 reports of dark features, where 1227 of these were physically checked either by patrol vessels, boats or airplanes.

6.2.1 Available Dark Features

For 844 of the dark features physically checked nothing was found, i.e. 68,3% of the in-situ observations made belong to this category. From this category, the 83 observations with a response time (time from SAR acquisition to in-situ

observation) lower than 3 hours are included in the analysis. It's difficult to know exactly what creates the dark features in the nothing observed category, it could be atmospheric/oceanographic phenomena or a substance that has vanished by the time it is checked. Due to the low response time of the dark features in the nothing observed category, it is assumed that these dark features are caused by atmospheric/oceanographic phenomena. 81 out of 1227 in-situ observations contained mineral oil, all of which are included in the dataset. The remaining 302 observations are Confimed Other Matter (COM) (algae, fish oil, chemical, unknown substance etc.). After consideration, it was decided that it was sufficient for the purpose of this thesis to only include 184 of these dark features. The remaining 119 dark features, mainly unknown substances, are excluded from the dataset.

Detection type	**Number of detections**
Algae	20
Chemical	18
Current front	3
Fish oil	57
Natural phenomena	6
Unknown substance	58
Produced water	3
Sandbank	2
Seaweed	2
Sewage	1
Vegetable oil	13
Total	183

Table 6.2: Distribution of COM.

As can be seen in table 6.2, there are mainly 5 large categories of COM in the dataset, namely unknown substance, fish oil, algae, chemical and vegetable oil, alongside several smaller categories. It's worth noticing that most of the COM observed are films on the surface, and not atmospheric/oceanographic phenomena. This raises the total number of dark features in the dataset to 348. Examples of mineral oil, COM and nothing observed can be seen in Figure 4.1a, 4.1b and 4.1c, respectively.

Satellite	**Number of detections**	**Oil**	**COM**	**Nothing observed**
RS2	174	51	96	27
S1	174	30	88	56
Total	348	81	184	83

Table 6.3: Number of dark features and type detected by each satellite.

An overview of the distribution of confirmed oil, COM and nothing observed, alongside the distribution between each satellite can be seen in Table 6.3.

Polarization	Number of detections
HH	3
HH/HV	4
VV	218
VV/VH	123

Table 6.4: Overview of the polarizations used to detect the dark features.

The data is mainly single- and dual-polarization data, and the distribution of polarizations can be seen in Table 6.4. The dataset primarily consists of VV and VV/VH polarizations. To decrease the number of variables in the dataset, the scenes acquired with a HH and HH/HV polarization are removed in this study. In addition, all dark features acquired at other modes than RS2 ScanSAR wide and S1 IW modes are removed from the dataset, alongside all dark features where either the product or Geographic Markup Language (GML) file was missing. Table 6.5 shows the total amount of dark features remaining after removal. The total number of unique dark features are now reduced to 325. For all scenes acquired by S1, there exists both a GRDM and GRDH product, implying that the data size should be the same for both product types. This is not the case in Table 6.5, which is elaborated in section 7.1.1.

6.2.2 Metadata Available for Each Dark Feature

The 325 dark features that are analysed here are spread throughout 181 scenes. The geographic span of the data is all the way from the Norwegian sea in the north, to Iceland in the west, to the Mediterranean sea in the south and to the Baltic sea in the east. For each of the dark features, KSAT provided the SAR product and the GML file. The GML file contains information about the detection made by KSAT. The parameters available for each suspected oil spill can be seen in Table 6.6, 6.7 and 6.8, illustrated by an example. The data acquired from the SAR product and GML file can be seen in Table 6.6 and 6.7, respectively. These files represent information about the SAR scene and

Detection type	RS2 ScanSAR	S1-GRDM	S1-GRDH
Oil	47	27	19
COM	85	85	68
Nothing observed	27	54	37
Total	159	166	124

Table 6.5: Number of dark features analysed in this thesis.

Product property	Sensor	
	RS2	S1
Incidence near [°]	19,503	30,341
Incidence far [°]	49,473	45,641
Pixels in range [#]	10552	6344
Pixels in azimuth [#]	9987	23317
Incidence angle [°]	42,426	37,448
Bandwidth azimuth [Hz]	188,223	327
Bandwidth range [MHz]	11,597	56,5
Resolution in azimuth [m]	50	40
Resolution in range [m]	50	40
Multilooking azimuth [#]	2	5
Multilooking range [#]	4	22
Acquisition mode	ScanSAR Wide	IW
Beams	W1 W2 W30 S7	
Pulse repetition frequency [Hz]	1273,4	1717,1
Radar frequency [Hz]	5405	5405

Table 6.6: The data from the SAR product file, illustrated by the data from RS2_20160311_060832_0075_SCWA_VV_SGF_462443_2637_12781763 and S1A_IW_GRDM_1SDV_20160629T161208_20160629T161428_011928_0125FB_48E6.

Property from GML	Value
Size (m^2)	276132
Length(m)	6696
Width(m)	510
Orientation (°)	300,8
Shape	Linear, tail
Contrast characteristics	Variable
Edge characteristics	Variable
Texture characteristics	Variable
Position of slick in range (pixel)	8071
Position of slick in azimuth (pixel)	6713
Wind speed SARTool (m/s)	1,99
Wind direction SARTool (°)	162
Wind speed model (m/s)	5,13
Wind orientation model (°)	170
Wave height model (m)	0,6

Table 6.7: The data from the GML file produced by KSAT, illustrated by the data from RS2_20160311_060832_0075_SCWA_VV_SGF_462443_2637_12781763.

Property from feedback report	Value
Satellite	RS2
Polarization	VV
Coordinate of dark feature (longitude/latitude)	004° 44’ 54.04" E / 055° 45’ 21.55" N
Acquisition time (SAR)	11/03-2016 06:08:31
Coastal States	Germany, Bonn Agreement, European Union, Denmark
Service	KSAT
Class	A
Pollution type	Mineral oil
Area	Denmark
Observation time (visual)	11/03-2016 07:41:00
Observation method	Fixed wing aircraft
Observer	Naval Airwing 3

Table 6.8: The data extracted from the feedback reports provided by EMSA, illustrated by the scene RS2_20160311_060832_0075_SCWA_VV_SGF_462443_2637_12781763.

about the detection made by KSAT. The wave height is only available for the newest RS2-scenes. The incidence angle of the slick is not directly acquired from the product file, but is calculated using linear interpolation and data from the product file. An example of the data available from the feedback reports from EMSA after in-situ check can be seen in Table 6.8. Whereas acquisition time denotes the time the SAR scene is acquired, observation time denotes the time at which the slick is visually checked. KSAT has their own confidence levels in each detection, denoted by class. "A" indicates high confidence and "B" indicates low confidence.

7 Method

This chapter gives an overview of what has been done to each dark feature, both in terms of preprocessing and calculation.

7.1 Preprocessing

Preprocessing readies the SAR-data to the principal analysis [Campbell and Wynne, 2011]. It prepares, or in some cases improves, the image such that information can be extracted at a later stage.

7.1.1 Segmentation

Segmentation of the slicks is the first step in the processing of the data. In this case, segmentation means separating the open sea and the slick, such that calculations can be made on the slick itself, and not the open sea. Several automatic segmentation techniques are presented in [Brekke and Solberg, 2005]. Although there are several automatic segmentation methods, none of them are perfect. Thus KSAT is still using manual segmentation in their operational oil slick detection service. To mimic how things are done operationally and to have full control of the masks, dark features originating from RS2 and S1-GRDM scenes are segmented manually. The main problem when segmenting manually is human errors such as inconsistency, especially when segmenting a

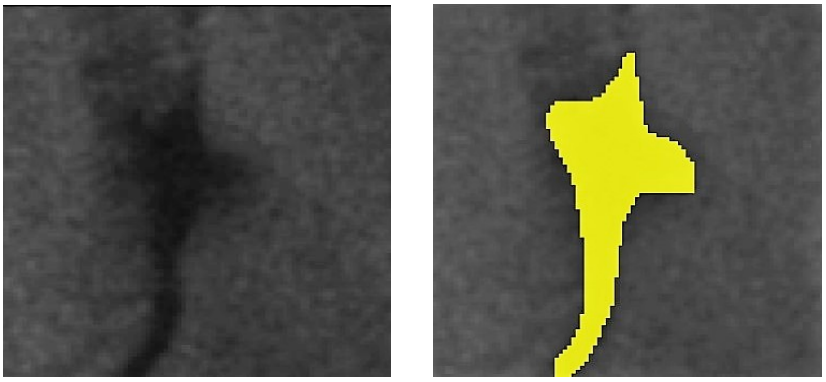

(a) Original image. **(b)** Segmented image

Figure 7.1: Example illustrating the segmentation. RADARSAT-2 Data and Products © MacDONALD, DETTWILER AND ASSOCIATES LTD., 2016 – All Rights Reserved.

large number of slicks over a long period of time.
To avoid open water in the masks, regions where it is difficult to decide whether it is open water or a dark feature are not included. An example of a region which it is hard to decide whether to include in the mask can be seen in Figure 7.1, where there is a region above the segmentation mask which is slightly darker than the open sea. However, it is not included in the mask since it is hard to decide which category it belongs to. It's very important to avoid objects such as vessels and platforms in the segmentation mask. Target smearing often happens in areas close to bright objects. An example can be seen in Figure 7.2. It's vital to avoid these areas in the mask.

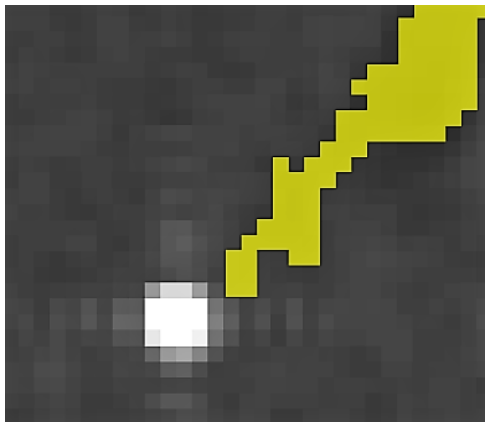

Figure 7.2: Example illustrating target smearing. RADARSAT-2 Data and Products © MacDONALD, DETTWILER AND ASSOCIATES LTD., 2016 – All Rights Reserved.

The variation in each dark feature in terms of incidence angle and sea state,

makes it difficult to directly compare the dark features to each other. [Skrunes et al., 2015a] accounted for this variation by normalizing with respect to the sea state, which proved effective. To perform this procedure, there is need for a mask representing a clean sea region. An example of a clean sea mask can be seen in Figure 7.3. Unlike when segmenting the dark features,

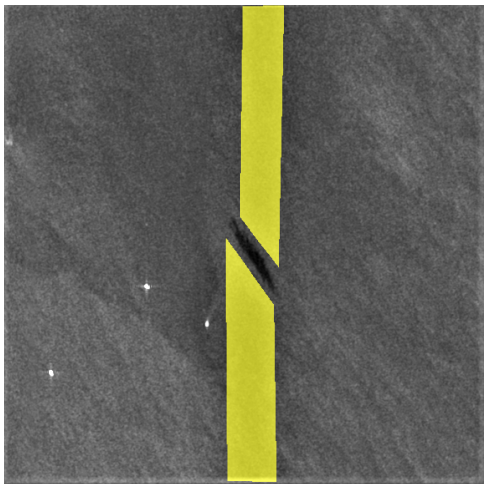

Figure 7.3: Example of a mask used to represent the average sea state around a slick. Contains modified Copernicus Sentinel data 2017, processed by KSAT.

there is less constrains in how many pixels the mask can contain. Making the sea-mask much larger than the slick will give a better statistical representation of the sea state. Although one has to be careful and only include open water in the masks, and to have a mask spanning approximately the same incidence angles as the dark feature. The normalization procedure is performed for the log-cumulants, and are further described in section 7.2. The sea masks are also used to calculate the damping ratio.

A vital element in the thesis is to compare the parameters obtained from the same dark features in S1-GRDM and S1-GRDH scenes. This will give an indication of their dependency on resolution. To maximize the comparability of the results from S1-GRDM and S1-GRDH scenes, each mask segmented from S1-GRDM products are moved to the S1-GRDH grid such that the masks cover roughly the same area. The first step of this process is to geocode the scenes, which means converting each pixel into geographic coordinates. Then each pixel in the scene corresponds to a location on the earth surface, and the S1-GRDM mask can be recreated in the S1-GRDH grid by moving the mask to the pixels representing the same area in the S1-GRDH format. The result of this procedure can be seen in figure 7.4. This method worked satisfyingly for most of the masks, although 42 masks were moved to the wrong position. This is a problem previously observed when geocoding S1-scenes in Sentinel

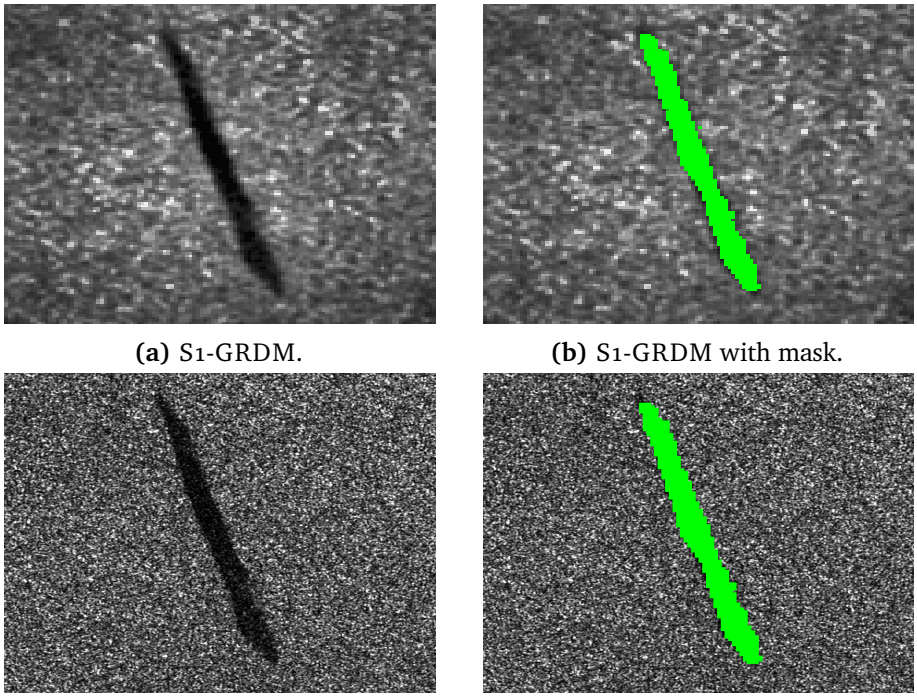

(a) S1-GRDM. **(b)** S1-GRDM with mask.

(c) S1-GRDH. **(d)** S1-GRDH with mask

Figure 7.4: Example showing a dark feature (at 54,73N, 6,45E) and the mask segmented from the S1-GRDM product, alongside the same dark feature and the equivalent mask moved to the S1-GRDH grid. The size of the S1-GRDM and S1-GRDH subscenes are 118 × 128 pixels and 469 × 508 pixels, respectively. All images are from the dataset used throughout this thesis. (a-b) Contains modified Copernicus Sentinel data 2017, processed by KSAT . (c-d) Produced from ESA remote sensing data.

Application Platform (SNAP), and is further confirmed here. The reason for this problem is unknown, but it is suspected that it could be caused by some bug in SNAPs code. One option would be to segment these masks manually, but this would not make it possible to directly compare results from S1-GRDM and S1-GRDH. As a consequence, these 42 dark features are excluded from the dataset.

7.1.2 Calibration

Calibration of SAR-data is essential when working with data from different sensors, or data acquired with the same sensor, but under different operating conditions. Inspection of equation 2.9 reveals that the power of the received signal is not only dependent on the interaction between the target and transmitted pulse. It is also dependent on factors such as the antenna

gain and system loss. This introduces serious radiometric bias in SAR images [El-Darymli et al., 2014].
Calibration of SAR images changes the pixel values such that they go from being represented by the biased backscattered signal, to being represented by the RCS and the backscatter coefficient (σ_0). RS2, S1A and S1B images comes with look-up tables making it possible to conduct σ_0, β_0 and γ_0 calibrations. σ_0 is the RCS per unit area in ground-range. β_0 is the radar brightness coefficient, and is the RCS per unit area in slant-range. γ_0 is the RCS per unit area of the incident wavefront [El-Darymli et al., 2014]. These parameters are illustrated in Figure 7.5. The calibration of SAR Georeferenced Fine (SGF) from RS2 is

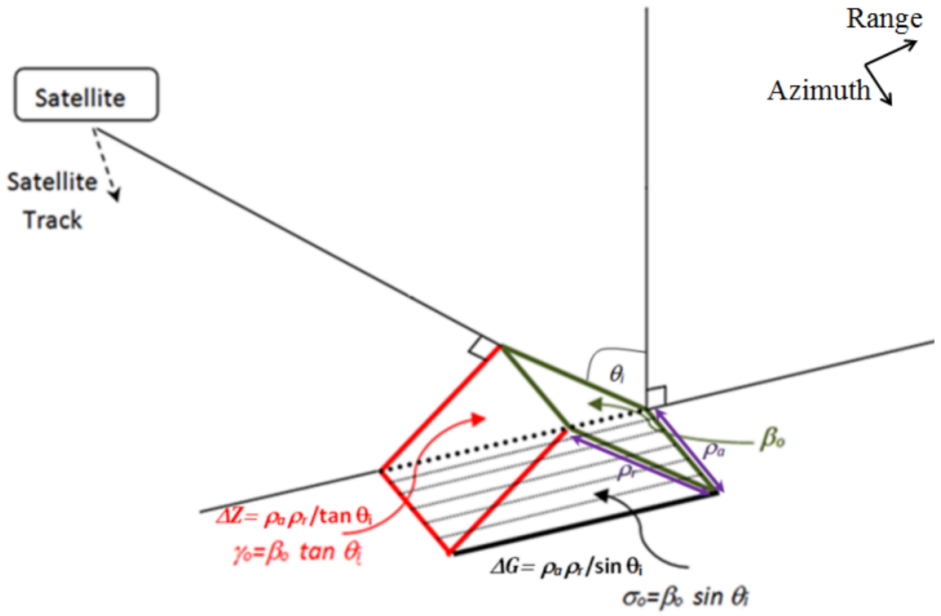

Figure 7.5: Illustration of the different radiometric calibrations. Figure from [El-Darymli et al., 2014].

achieved by [Dettwiler et al., 2008b]

$$\text{Calibrated value} = \frac{\text{Digital value}^2 + \text{Offset}}{\text{Gains}}, \tag{7.1}$$

where gains and offset are provided in a Look-Up Table (LUT) with each product. Equation 7.1 are applied to each RS2 image in the dataset. The same calibration procedure applies for S1 Ground Range Detected (GRD) products, with some alterations [ESA, 2017a]

$$\text{Calibrated value} = \frac{|\text{Digital value}|^2}{\text{Gains}^2}, \tag{7.2}$$

where gains can be found in the LUT provided with each product.

7.2 Calculation of Log-Cumulants

After segmentation and radiometric calibration, log-cumulants can be calculated using equation 4.23, 4.24 and 4.25. [Skrunes et al., 2015a] calculated log-cumulants using a randomly chosen sample of 4000 pixels from each dark feature, then this calculation was repeated 200 times. The number of pixels in each mask in the RS2 dataset can be seen in Figure 7.6. Note that there are a few masks with a size greater than 10 000, but these are left out of Figure 7.6 for visual reasons. The size of the S1-GRDM masks are in the same range. The number of pixels available for each dark feature in this data is far less than [Skrunes et al., 2015a] had. As a consequence, all of the pixels in each mask are used in the calculations, instead of using a fixed number of pixels in all masks.

After calculating the log-cumulants, they are normalized. This is achieved by calculating the log-cumulants from a clean sea region (which represents the average sea state in this region). Then κ_ν is normalized by

$$\tilde{\kappa}_\nu = \kappa_{\nu darkfeature} - \kappa_{\nu sea}, \tag{7.3}$$

where $\kappa_{\nu darkfeature}$ and $\kappa_{\nu sea}$ denotes the κ of order ν for the dark feature and sea state, respectively.

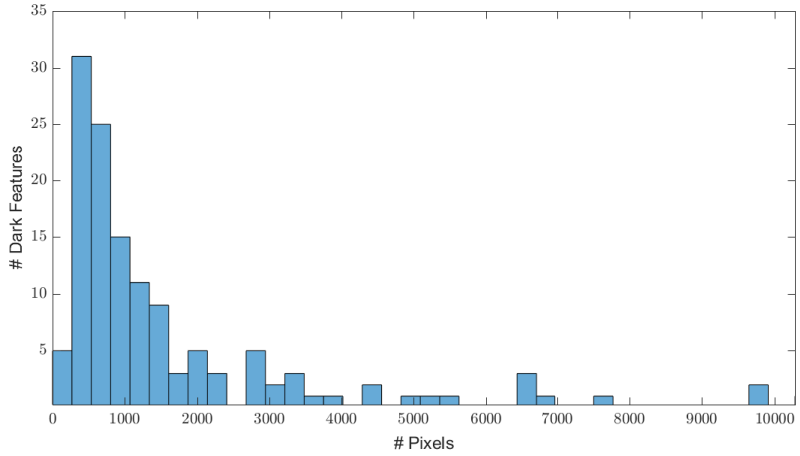

Figure 7.6: Histogram showing the number of pixels each segmented mask contains from the RS2 dataset.

7.3 Classification

Figures 7.7 shows the distribution for some of the parameters available in KSATs detection report, where all bars sums to one for each class. Most of these parameters are set manually by the operators. These figures underlines the complexity in the process of discriminating mineral oil and look-alikes, where look-alikes denotes both the COM and nothing observed class. The difference between Figure 7.7a and Figure 7.7b is that they contain dark features acquired by S1 and RS2, respectively. Figure 7.7a indicates that a large portion of mineral oil spills tend to be smaller than 1.5 km^2, while Figure 7.7b on the other hand, suggests that around half of the mineral oil spills are greater than 1.5 km^2. A high percentage of the dark features are labelled with variable contrast, texture or edge in Figures 7.7c-7.7h , with little separation between the classes and consequently low separation. Figures 7.7i and 7.7j shows that the outline of a dark feature provides little separation between the classes. No conclusive parameters are identified in Figure 7.7.

Several of the parameters shown in Figure 7.7 are set manually by the operator, and are consequently subjective. These parameters will be tested in the SVM, in addition to testing the parameters presented in section 4.2.3, which are objective and quantitative parameters. Table 6.5 shows that the distribution of oil spills and look-alikes in the dataset are uneven. Ideally, this distribution should be more even. A common problem when trying to classify unbalanced classes using linear classifiers or clustering techniques, is that the smallest classes might not be "found" by the classifier. This often leads to misclassifications.

MatLabs built-in classification learner software is applied to classify the data [MatLab, 2018] using a linear SVM(see chapter 5 for more details). This software trains models to classify data, and it offers several types of classification models, including decision trees, discriminant analysis, linear and non-linear SVMs, logistic regression, nearest neighbours and ensemble classification. All of these methods were tested on the dataset initially by varying the input parameters, with linear SVM proving to give the best and most consistent result. The first classification model is implemented using the log-cumulants and parameters suggested in literature. The parameters used includes both geometrical descriptors and parameters characterizing the physical behaviour of the dark feature, all of which are quantitative parameters. The parameters being assessed in this model includes:

- $\tilde{\kappa_1}$(defined in section 4.3): measures the relative radar backscatter from the dark feature normalized to the sea state, i.e. contrast between a dark feature and sea state

- $\tilde{\kappa_2}$(defined in section 4.3): describes the relative variance of the dark feature normalized to the sea state, i.e. the relative texture between a dark feature and sea state
- $\tilde{\kappa_3}$(defined in section 4.3): measures the relative skewness in the distribution of the dark feature, normalized to the sea state
- κ_2(defined in section 4.3): describes the variance of the dark feature, i.e. its texture
- Width[pixel](defined in section 4.2.3): distance across the dark feature
- Length[pixel](defined in section 4.2.3): distance across the dark feature in the direction perpendicular to the width
- $\hat{\phi}_1$(defined in section 4.2.3): shape parameter that describes the elongatedness of dark feature
- Damping-ratio (defined in section 4.2.3): physical descriptor defined as the ratio between the radar backscatter of the dark feature and the sea state, measures contrast between the dark feature and sea state
- Perimeter[pixel](defined in section 4.2.3): describes the length of the boundary around the dark feature
- Area[pixel](defined in section 4.2.3): the size of the dark feature
- Compactness(defined in section 4.2.3): shape parameter that measures the circularity of a dark feature
- Coefficient of variation(defined in section 4.2.3): physical descriptor defined as the ratio between the standard deviation and the mean of the dark feature
- Number of objects: tells whether the dark feature is continuous or fragmented

The second classification model is implemented using the log-cumulants and the parameters available in KSATs detection report. These parameters consists of both quantitative and qualitative parameters and includes: $\tilde{\kappa_1}$, $\tilde{\kappa_2}$, $\tilde{\kappa_3}$, κ_2, width[m], length[m], SAR derived wind speed, area[m^2], contrast, edge, natural slicks in vicinity, shape, outline, shape related to wind history and texture, where the first 8 parameters are quantitative and the rest are qualitative parameters. To validate the results of the classification, k-fold cross validation is

used in both models. In this method the dataset is randomly partitioned into k subsamples, then one single subsample is retained as validation data, and the remaining k-1 subsamples are used as training data. This process is repeated k times until all subsamples are used as validation data. Due to the size of the dataset used in this thesis, it is desirable to maximize the size of the training data used. The ideal option would be the leave-one-out validation scheme, but this is not an option in MatLabs software. This implies that a large k should be chosen in the k-fold cross validation. The maximum size possible to choose in MatLabs classification software is 50, hence all classification results in this thesis are generated using 50-fold cross validation.

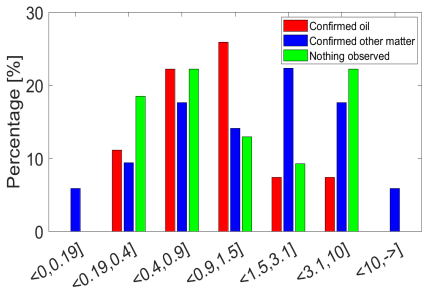

(a) Size [km^2] S1

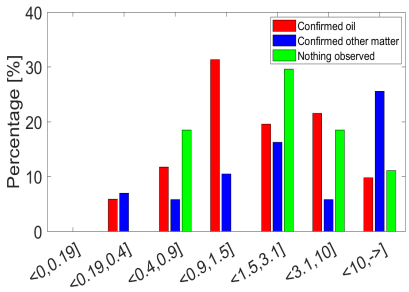

(b) Size [km^2] RS2

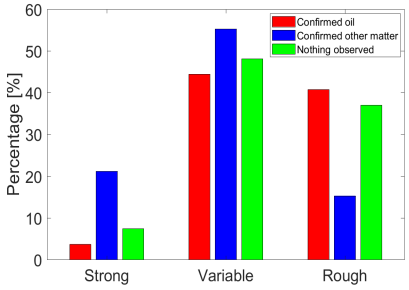

(c) Texture S1

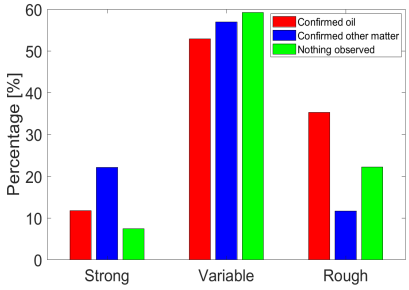

(d) Texture RS2

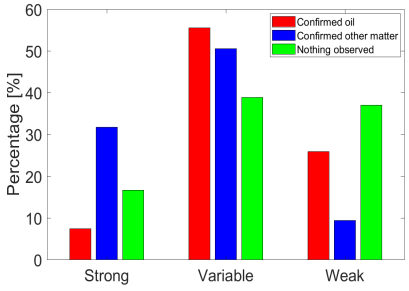

(e) Contrast S1

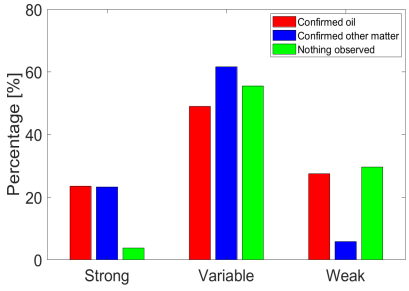

(f) Contrast RS2

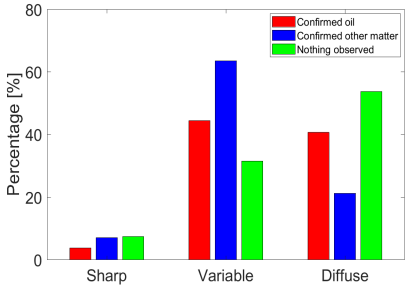

(g) Edge S1

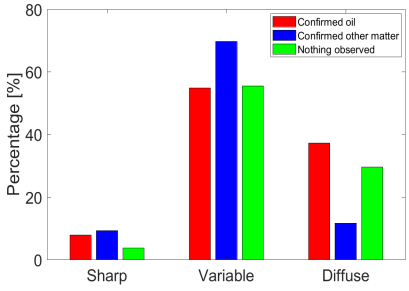

(h) Edge RS2

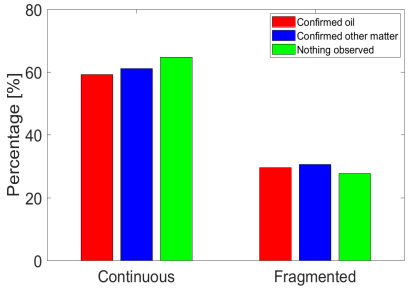

(i) Outline S1

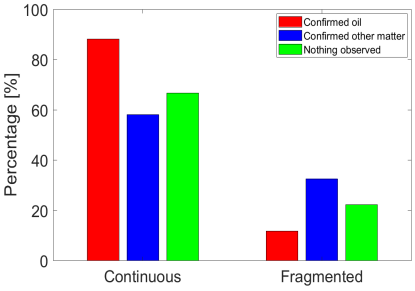

(j) Outline RS2

Figure 7.7: The distribution of parameters for the dark features in the dataset, (a-b) size, (c-d) texture, (e-f) contrast, (g-h) edge and (i-j) outline. (a,c,e,g,i) Properties of dark features captured by S1. (b,d,f,h,j) Properties of dark features acquired by RS2. The bars for each class sums to one in all figures.

8

Results and Discussion

In this chapter, the results are presented and discussed. The first and second order log-cumulant and their dependency on variables such as incidence angle, wind-speed, sensor and spatial resolution are analysed. The separability obtained between mineral oil and look-alikes will be tested using a linear SVM, with a variety of parameters as input. These parameters includes descriptors currently applied in KSATs detection service, and quantitative parameters selected from literature describing several of the same characteristics.

8.1 Log-Cumulant Analysis

This section contains the log-cumulant analysis. The dataset is mainly divided into two parts, namely the data acquired by RS2 and the data acquired by S1. The two datasets will be investigated and discussed individually.

8.1.1 Analysis of the RS2 Dataset

This subsection contains the investigation of log-cumulants using the RS2 dataset. The RS2 dataset contains the same dark features as analysed in the preliminary study to this thesis, but it is further extended. The nothing observed class is added to the dataset, which represents a new class of look-alikes that should be easier, but also more important to separate from mineral oil. Several

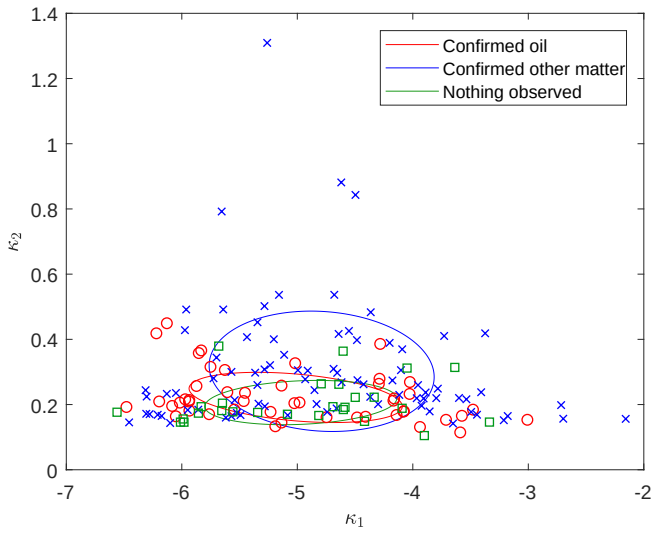

Figure 8.1: κ_2 plotted as a function of κ_1. Confirmed oil spills are denoted by red circles, COM by blue crosses and nothing observed by green squares. The ellipses represent the mean and variation for each class.

new dark features containing mineral oil are added to the dataset. κ_1, κ_2, $\tilde{\kappa_1}$ and $\tilde{\kappa_2}$ was identified as the most interesting and promising log-cumulants in the preliminary study, leading to a more extensive analysis of these parameters in this thesis. Plots involving κ_3 and $\tilde{\kappa_3}$ are found in Appendix A.

Log-Cumulants and Normalized Log-Cumulants

Figure 8.1 shows κ_2 plotted as a function of κ_1. The ellipses orientation in space is determined by the principal components, its position by the mean and the size is set to be 2 standard deviations for each class. The ellipses are included to better show the general characteristics of each class. The overlap between the ellipses are substantial, indicating an overall bad separation between the classes. κ_1 appears to be quite similar for all classes, both in terms of spread and mean. The variation and mean in κ_2 is larger for COM, than it is for the other classes. This implies that COM in general has a larger internal variation within the dark feature.

The data presented in Figure 8.1 consists of dark features obtained at different incidence angles and different metocean conditions. These parameters affects the radar backscatter, which makes it difficult to directly compare the dark features to one another. As a measure to try to account for this, the log-cumulants are normalized with respect to the sea state. Figure 8.2 shows $\tilde{\kappa_2}$ plotted as a function of $\tilde{\kappa_1}$, where $\tilde{\kappa_1}$ and $\tilde{\kappa_2}$ denotes the normalized (see

equation 7.3) κ_1 and κ_2, respectively. The normalization procedure moves the sea state to position (0,0), and seems to remove much of the spread in the data, especially in $\tilde{\kappa_1}$ direction. The normalization procedure also increases the separation between the classes, although there's still to much overlap to successfully separate the classes. κ_1 is a measure of the radar backscatter, while $\tilde{\kappa_1}$ is a measure off the radar backscatter in the dark feature compared to the sea state. This means that $\tilde{\kappa_1}$ can be used as indirect measure of the damping ratio, where a low $\tilde{\kappa_1}$ implies a large damping ratio and vice versa. κ_2 is a measure of the variation in radar backscatter within the dark feature, i.e. it measures the texture. $\tilde{\kappa_2}$ then measures the texture in relation to the texture of the sea state. From Figure 8.2, COM appears to have an increased spread and mean in $\tilde{\kappa_2}$, compared to both mineral oil and nothing observed. The other classes have lower and more concentrated $\tilde{\kappa_2}$ values. This means that mineral oil and nothing observed have similar texture, and that COM can generate dark features both with a far greater texture, but also in the same range as the other classes. Mineral oil appears to have a slightly smaller $\tilde{\kappa_1}$ than nothing observed, meaning that mineral oil generally creates a greater damping effect than nothing observed. COM produces some "outliers", which generates a larger damping effect than the other classes. The plot also suggests that there is a negative correlation between $\tilde{\kappa_1}$ and $\tilde{\kappa_2}$ for COM.

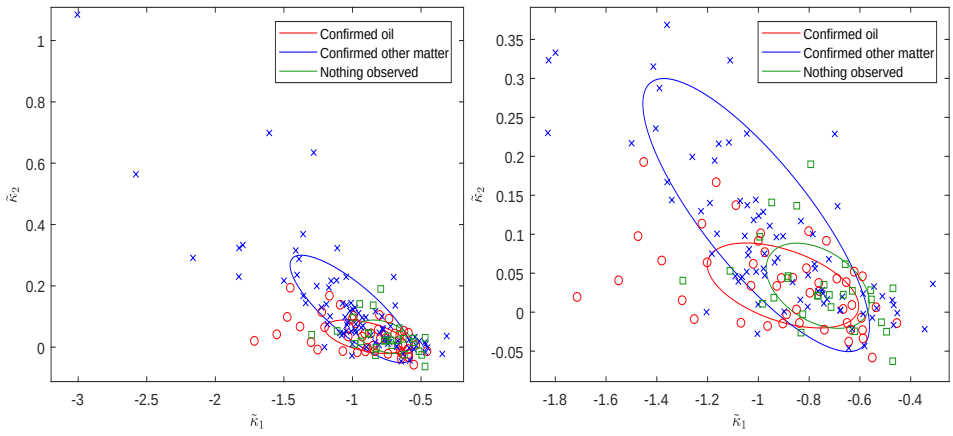

(a) **(b)**

Figure 8.2: $\tilde{\kappa_2}$ plotted as a function of $\tilde{\kappa_1}$. (a) contains all the data, while (b) is a zoomed version. Confirmed oil spills are denoted by red circles, COM by blue crosses and nothing observed by green squares. The ellipses represent the mean and variation for each class.

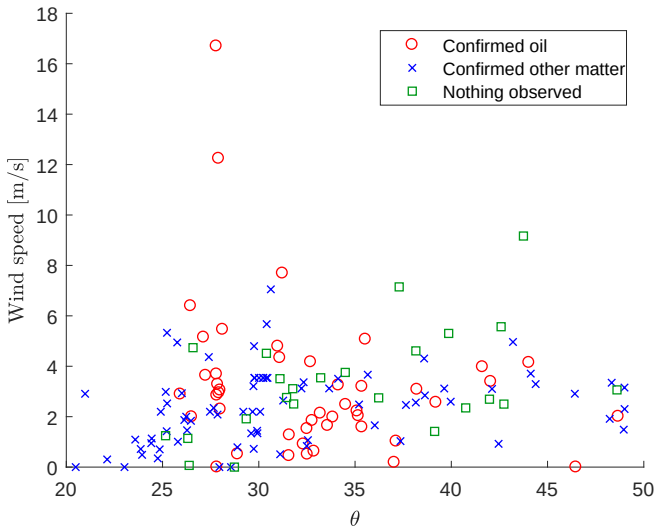

Figure 8.3: SAR derived wind speed plotted as a function of θ. Confirmed oil spills are denoted by red circles, COM by blue crosses and nothing observed by green squares.

Relationship between Log-Cumulants and Incidence Angle

This section explores the relationship between log-cumulants and incidence angle. The preliminary study revealed that κ_1 decreases with increasing incidence angle, i.e. the dark feature gets darker with increasing incidence angle. The radar backscatter for ocean areas are known to decrease with incidence angle [Elachi and Van Zyl, 2006] [Thompson et al., 1998], which explains the κ_1-θ relationship. Neither κ_2, $\tilde{\kappa_1}$ or $\tilde{\kappa_2}$ are found to have any considerable dependency on θ. Figure 8.3 illustrates how the detections are distributed over θ. It seems like θ values in the range 24-45°are ideal for detecting dark features, the density of dark features for θ values outside of this interval is considerably lower. It is interesting that there are no detected mineral oil spills for θ lower than 26°, but still several COM.

Dividing the dataset into subsets based on incidence angle might give more separable classes. The dataset is first divided into three subsets. Figure 8.4 shows $\tilde{\kappa_2}$ plotted as a function of $\tilde{\kappa_1}$ for incidence angles [19°,30°), [30°,40°] and (40°,50°]. An similar figure for κ_2 plotted as a function of κ_1 can be found in Appendix A. For dark features detected at near-range incidence angles [19°,30°), COM stands out from the other classes, with this class generally having a larger $\tilde{\kappa_2}$ combined with a lower $\tilde{\kappa_1}$ than the rest of the dark features. All of the classes still ends up in the same cluster, resulting in a an overall bad separation between the classes. Mid-range incidence angles [30°,40°] is either not able to produce any clear separation. The ellipses reveal some tendencies

in the plot, mineral oil seems to cluster towards in the lower left part of the plot i.e. this class produces a larger damping effect and more uniform dark features. COM groups up more towards the top right, meaning that it creates a smaller damping effect and has more variation within the dark features. Nothing observed ends up in between the two other classes, with a slightly lower damping ratio. There are considerable fewer dark features detected at far-range incidence angles (40°,50°], than it is for near-range angles. The radar backscatter tends to decrease with increasing incidence angle, leading to a signal closer to the noise floor, thus making it harder to detect dark features. COM tends to have a larger spread in $\tilde{\kappa_2}$, while nothing observed generally produce a lower damping ratio than the other classes. Dividing the dataset into subsets based on incidence angle tends to slightly increase the separation between the classes, especially for mid-range incidence angles.

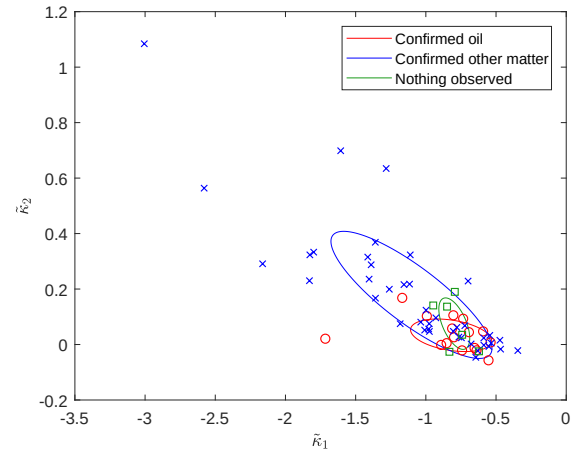

(a)

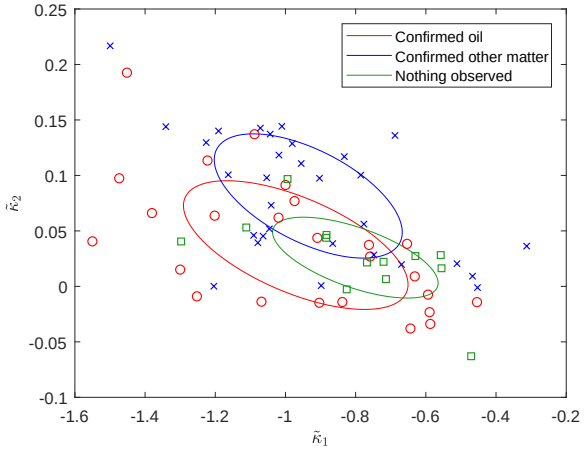

(b)

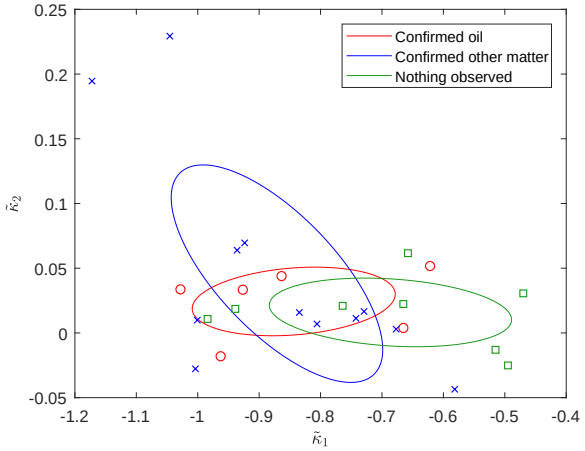

(c)

Figure 8.4: $\tilde{\kappa_2}$ plotted as a function of $\tilde{\kappa_1}$ sorted by θ (a) $\theta \in [19°,30°)$, (b) $\theta \in [30°,40°]$ and (c) $\theta \in (40°,50°]$. Confirmed oil spills are denoted by red circles, COM by blue crosses and nothing observed by green squares. The ellipses represent the mean and variation for each class.

Relationship between Log-Cumulants and Wind Speed

The preliminary study revealed that κ_1 had a slight increase with wind-speed, which is expected since high wind speeds increases the Bragg waves on the ocean surface, thus increasing the radar backscatter. No specific dependency was identified in the preliminary study between κ_2 and wind speed. Figure 8.3 shows that most of the dark features are detected in wind speeds below 6 m/s, implying that any relationships found between wind speed and log-cumulants can only be applied for wind speeds in this range. [Espedal, 1999b] suggests that a dark feature that remains connected above 7 m/s is likely to contain oil. This is observed in Figure 8.3, where about half of the dark features detected at wind speeds greater than 6 m/s contains oil, whereas the number of COM decreases with wind speed.

When dividing the data into subsets based on wind speed, only data with a wind speed below 6 m/s are included. Figure 8.5 shows $\tilde{\kappa_2}$ plotted as a function of $\tilde{\kappa_1}$ for dark features with wind speed in the intervals [0,2) m/s, [2-4] m/s and (4-6] m/s. The range of values for $\tilde{\kappa_1}$ and $\tilde{\kappa_2}$ varies between each plot, with Figure 8.5a having the smallest $\tilde{\kappa_1}$ and greatest $\tilde{\kappa_2}$, and Figure 8.5c producing the greatest $\tilde{\kappa_1}$ and the smallest $\tilde{\kappa_2}$ values. This implies that the normalized log-cumulants are dependent on wind speed, which wouldn't be the case if the normalization procedure had worked optimally. Figure 8.5a and 8.5b shows many of the same trends, with oil and nothing observed in general having relatively low $\tilde{\kappa_2}$-values with little spread. $\tilde{\kappa_2}$ appears to decrease as $\tilde{\kappa_1}$ increases for COM, this dependency is not found as clearly for the other classes. Figure 8.5c contains few dark features, thus making it difficult to say anything general about the classes. κ_2 plotted as a function of κ_1 for dark features with SAR tool derived wind speed in the intervals [0,2) m/s, [2-4] m/s and (4-6] m/s can be found in Appendix A. Dividing the dataset into subsets based on wind speed proves to slightly increase the separation between the classes for wind speeds in the range of 0-4 m/s, although a clear mixing still is observed.

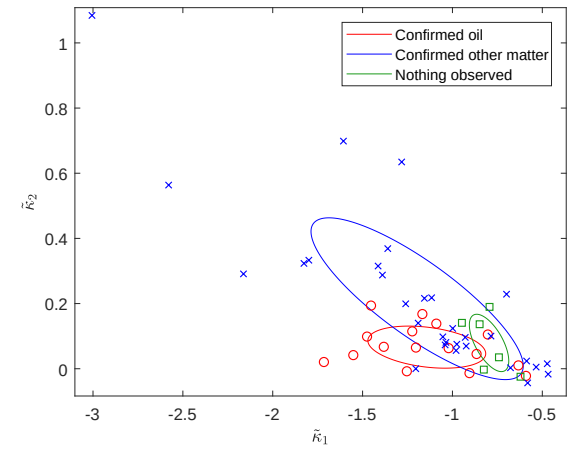

(a)

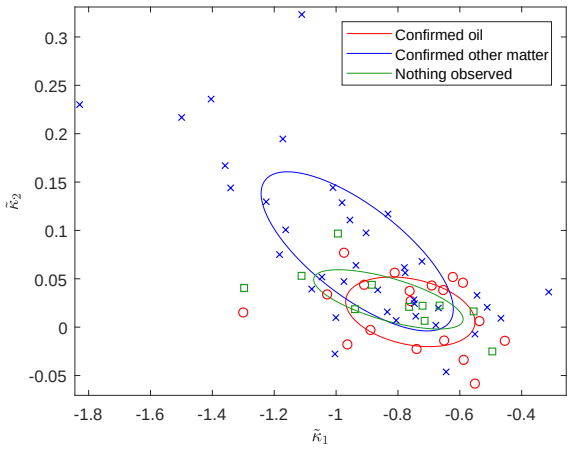

(b)

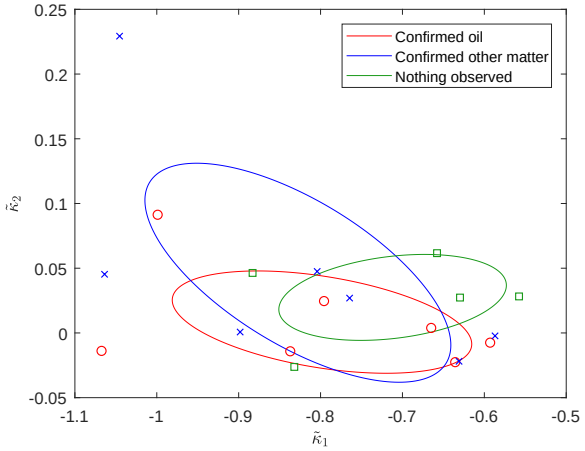

(c)

Figure 8.5: $\tilde{\kappa_2}$ plotted as a function of $\tilde{\kappa_1}$ sorted by wind speed (a) wind speed $\in[0,2)$ m/s, (b) wind speed $\in[2,4]$ m/s and (c) wind speed $\in(4,6]$ m/s. Confirmed oil spills are denoted by red circles, COM by blue crosses and nothing observed by green squares. The ellipses represent the mean and variation for each class.

8.1.2 Analysis of the S1 Dataset

This section contains the analysis of S1-GRDM and S1-GRDH products from the S1 dataset. Only RS2 ScanSAR data was studied in the preliminary study, implying that all of the data presented in this section is new data. Results from the preliminary study suggests that κ_1, κ_2, $\tilde{\kappa_1}$ and $\tilde{\kappa_2}$ are the most interesting parameters. Consequently, the main focus of the analysis will be on these parameters. Figures involving κ_3 and $\tilde{\kappa_3}$ can be found in Appendix B and C

Log-Cumulants and Normalized Log-Cumulants

Figure 8.6a shows κ_2 plotted as function of κ_1 for S1-GRDM products, which has a slightly increased resolution compared to the RS2 ScanSAR scenes (40 $\times$ 40m versus 50 $\times$ 50m). κ_1 seems to lie in the same range as the RS2 ScanSAR scenes, but κ_2 is slightly lower. It is expected that κ_2 increases with resolution, since this would make it possible to detect smaller variations within the dark feature, which is not observed here. This could be caused by the amount of multilooking performed, the RS2 ScanSAR scenes used in this thesis are multilooked 4×2 times in range and azimuth, respectively. The S1-GRDM scenes are on the other hand multilooked 22×5 times in range and azimuth, respectively. Multilooking smooths the data and consequently reduces texture, which results in a decreased κ_2. No separation between the classes are observed for in Figure 8.6a.

κ_2 plotted as function of κ_1 for S1-GRDH products are shown in Figure 8.6b. S1-GRDH (10 $\times$ 10m) products have an increased resolution compared to S1-GRDM products, and less multilooking (5×1 in range and azimuth, respectively), this leads to an increase in κ_2 compared to the S1-GRDM data. Now some is observed between mineral oil and the other classes in κ_2 direction. κ_1 is essentially the same as it was for the S1-GRDM products, which makes sense since multilooking shouldn't affect the mean backscatter in a dark feature, leading to no improved separation in κ_1 direction using S1-GRDH data.

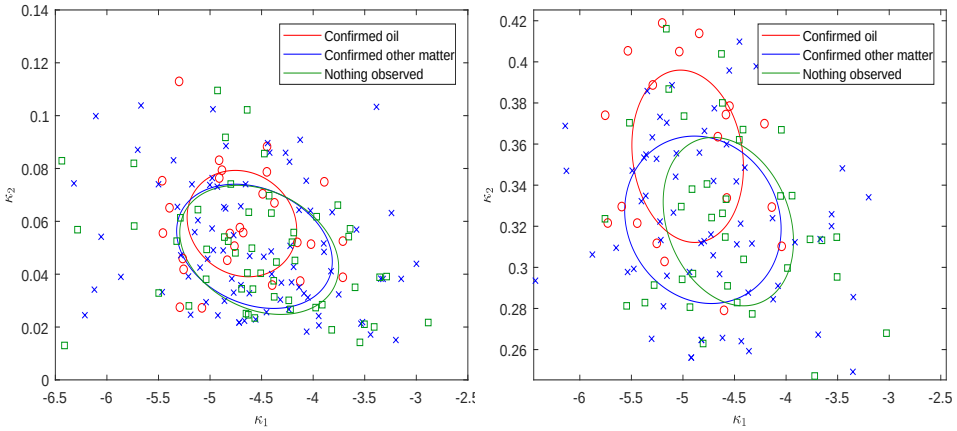

Figure 8.6: κ_2 plotted as a function of κ_1 for, (a) GRDM products and (b) GRDH products. Confirmed oil spills are denoted by red circles, COM by blue crosses and nothing observed by green squares. The ellipses represent the mean and variation for each class.

$\tilde{\kappa_2}$ plotted as a function of $\tilde{\kappa_1}$ for S1-GRDM products are displayed in Figure 8.7. The normalization increases the separation between the classes. The ellipse reveals that mineral oil generally has the smallest $\tilde{\kappa_1}$ and the largest $\tilde{\kappa_2}$ of the classes, i.e. mineral oil tends to produce dark features with both the greatest damping effect and texture. Nothing observed clusters more towards the bottom right in $\tilde{\kappa_1}$-$\tilde{\kappa_2}$ space, thus implying nothing observed produce dark features with both a low damping effect and low texture. The COM class ends up between the other classes, which leads to mixing.

The amount of S1-GRDM data available exceeds the amount of S1-GRDH data, due to difficulties transferring the segmentation masks (see Table 6.5 and section 7.1.1 for more details). To conclude on the importance of resolution in a credible manner, the results obtained using S1-GRDH data has to be compared to the results from S1-GRDM data using the same dark features. Figure 8.8 shows $\tilde{\kappa_2}$ plotted as a function of $\tilde{\kappa_1}$ for S1-GRDM and S1-GRDH data using the same dark features, i.e. only the dark features available in both S1-GRDM and S1-GRDH format. The general tendencies in Figures 8.7 and 8.8 are the same. Many of the dark features that causes mixing between mineral oil and nothing observed is not available in S1-GRDH format, leading to an increased separation between these classes when only plotting a subset of the S1-GRDM data (Figure 8.8a), compared to when using all the S1-GRDM data (Figure 8.7). The separation between mineral oil and nothing observed further increases in Figure 8.8b, with almost no overlap between the ellipses, thus enabling the separation of the majority of mineral oil and nothing observed. COM still ends

up between the two other classes, and with data all over $\tilde{\kappa_1}$-$\tilde{\kappa_2}$-space. This class consists of many different substances, which might explain the spread within the class. Separating all three classes proves to be a challenge, even using S1-GRDH data. All things considered, the increased resolution increases the separability of the classes, thus emphasizing the importance of resolution when working with log-cumulants. Resolution is identified as a key parameter to obtain separation between the classes, leading to a more comprehensive investigation of the S1-GRDH scenes in the sections to follow. For every figure presented using the S1-GRDH data, the equivalent S1-GRDM figure can be found in Appendix B.

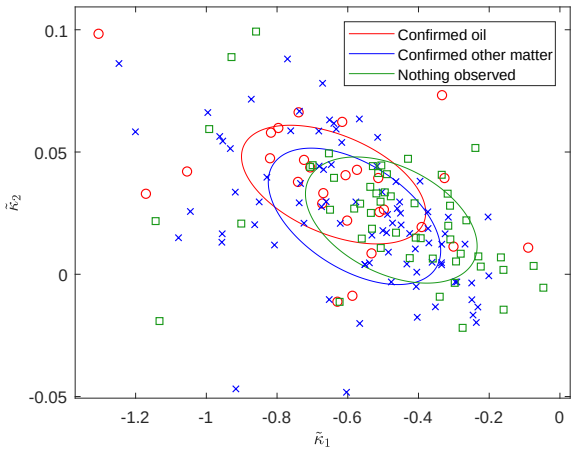

Figure 8.7: $\tilde{\kappa_2}$ plotted as a function of $\tilde{\kappa_1}$ for S1-GRDM data. Confirmed oil spills are denoted by red circles, COM by blue crosses and nothing observed by green squares. The ellipses represent the mean and variation for each class.

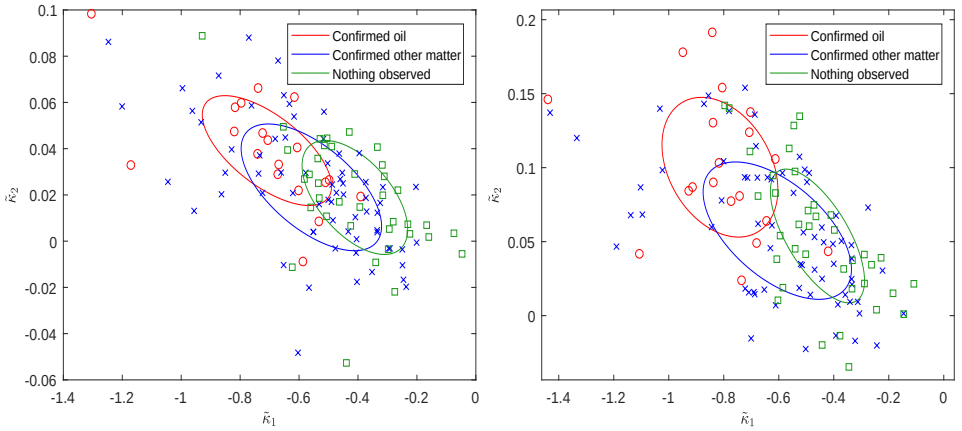

(a) **(b)**

Figure 8.8: $\tilde{\kappa_2}$ plotted as a function of $\tilde{\kappa_1}$, (a) for S1-GRDM data and (b) for S1-GRDH data. Both figures contains the same dark features. Confirmed oil spills are denoted by red circles, COM by blue crosses and nothing observed by green squares. The ellipses represent the mean and variation for each class.

Relationship between Log-Cumulants and Incidence Angle

Figure 8.9 shows how the detection distributes across θ, for the S1-GRDH data. The dark feature detection rate is more uniformly distributed across the available incidence angles, in contrast to what was the case using RS2 ScanSAR mode. The S1 IW mode only utilize about half the range of incidence angles as RS2 ScanSAR mode does, i.e. 30-46°, thus avoiding the most extreme incidence angles. κ_1, κ_2, $\tilde{\kappa_1}$ and $\tilde{\kappa_2}$, plotted as a function of incidence angle can be found in Appendix C. Neither of these are found to be dependent of incidence angle, thus varying from RS2 ScanSAR. The radar backscatter is expected to decrease with incidence angle, this relationship is not found in the S1-GRDH data used here. This might indicate that many of the dark features are close to the NESZ in the S1-GRDH data.

Figure 8.10 shows $\tilde{\kappa_2}$ plotted as a function of $\tilde{\kappa_1}$ for incidence angles [30°,35°), [35°,40°] and (40°,46°]. A substantial amount of the dark features ends up in the same $\tilde{\kappa_1}$ and $\tilde{\kappa_2}$ intervals regardless of incidence angle, which makes sense since neither $\tilde{\kappa_1}$ or $\tilde{\kappa_2}$ are found to be dependent on incidence angle. The number of dark features confirmed as mineral oil is limited for near-range incidence angles (Figure 8.10a), thus making it difficult to state anything general about this class. Except from a few outliers in the COM class, nothing observed and COM ends up in the same cluster, thus causing an overall bad separation between the classes for incidence angles at 30-35°. Figure 8.10b

shows the dark features acquired at mid-range incidence angles. In this case there is no overlap between the mineral oil and nothing observed ellipses, and almost no overlap between the mineral oil and COM ellipses. There is still a substantial overlap between the nothing observed and COM ellipses. Mineral oil generally seems to create dark features causing a greater damping and texture than the other classes, with nothing observed producing the lowest damping effect and texture. COM ends up between the other classes. The trend in the figure is the same for far-range angles (Figure 8.10c) as it is for mid-range incidence angles. There's a clear separation between mineral oil and nothing observed, with mineral oil generating the greatest texture and nothing observed producing the lowest damping effect. The main difference between the two figures is that COM now produces the greatest damping effect, although the class also has a great spread in $\tilde{\kappa_1}$.

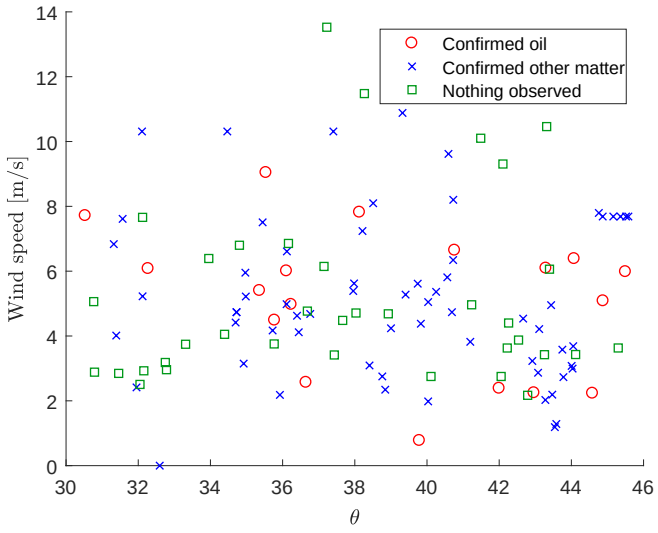

Figure 8.9: SAR derived wind speed plotted as a function of θ for S1-GRDH. Confirmed oil spills are denoted by red circles, COM by blue crosses and nothing observed by green squares.

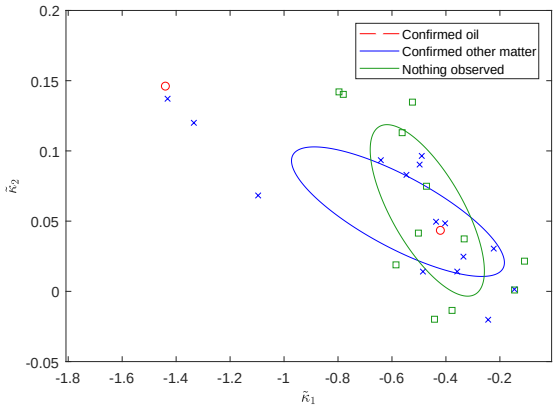

(a)

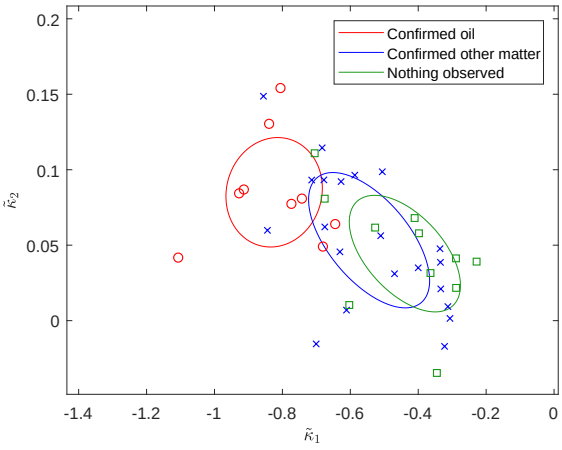

(b)

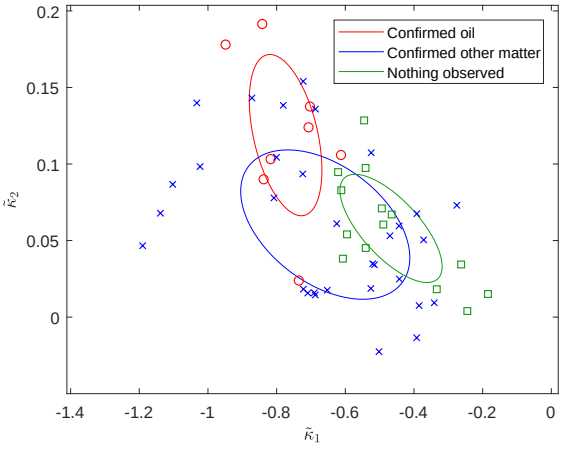

(c)

Figure 8.10: $\tilde{\kappa_2}$ plotted as a function of $\tilde{\kappa_1}$ for S1-GRDH data, sorted by θ, (a) $\theta \in [30°,35°)$, (b) $\theta \in [35°,40°]$ and (c) $\theta \in (40°,46°]$. Confirmed oil spills are denoted by red circles, COM by blue crosses and nothing observed by green squares. The ellipses represent the mean and variation for each class.

Relationship between Log-Cumulants and SAR Derived Wind Speed

κ_1, $\tilde{\kappa_1}$, κ_2 and $\tilde{\kappa_2}$ plotted a function of SAR derived wind speed can be found in Appendix C for S1-GRDH data. The preliminary study revealed that κ_1 had a positive correlation wind speed for RS2. This relationship is further confirmed here. $\tilde{\kappa_1}$ is found to have a slight positive correlation with wind speed, while κ_2 and $\tilde{\kappa_2}$ are found to be independent of wind speed. The distribution of the data over wind speed for S1-GRDH data can be seen in Figure 8.9, which clearly stands out from the RS2 ScanSAR dataset. There are considerably fewer dark features acquired at wind speeds below 2 m/s, and substantially more dark features acquired at wind speed above 6 m/s. This could be caused by S1 not being able to detect as many dark features at low wind speeds, and instead detects more at higher wind speeds. It could also be caused by the wind speed algorithm overestimating the wind speed in S1 and/or underestimating the wind speed in RS2. The number of nothing observed dark features seems to be especially dense for wind speeds from 2-5 m/s. As mentioned in the RS2 section, it is expected that dark features that still is connected at wind speeds above 7 m/s is likely to contain mineral oil. However, this is not observed for the S1-GRDH data.

Figure 8.11 shows $\tilde{\kappa_2}$ plotted as a function of $\tilde{\kappa_1}$ for SAR derived wind speed in the range [0,4) m/s, [4,8] m/s and (8,14] m/s. Figure 8.11a contains a large number of nothing observed, which appears to create the highest $\tilde{\kappa_1}$ and lowest $\tilde{\kappa_2}$ of the classes, i.e. this class has the lowest damping effect and texture. Mineral oil has the greatest $\tilde{\kappa_2}$, thus implying that these dark features have the greatest texture. The separation between mineral oil and nothing observed is clear. COM has some outliers with a high $\tilde{\kappa_1}$ that leads to a large spread in κ_1 direction for this class. COM ends up between mineral oil and nothing observed, thus leading to a poor separation between COM and the other classes. The separation between the mineral oil and nothing observed has decreased for wind speeds in the range of 4-8 m/s (Figure 8.11b), while the separation between mineral oil and COM has slightly increased compared to the low wind speed conditions. The ellipses indicates that mineral generally produces the lowest $\tilde{\kappa_1}$ and the greatest $\tilde{\kappa_2}$, i.e. this class creates dark features with the highest damping effect and texture. The ellipses of nothing observed and COM now almost completely overlap, which means that there are no separation between the classes. $\tilde{\kappa_2}$ plotted as a function of $\tilde{\kappa_1}$ for dark features acquired with a wind speed in the range 8-14 m/s can be seen in Figure 8.11c. $\tilde{\kappa_1}$ generally seems to be higher here contra Figures 8.11a and 8.11b, thus implying that the contrast between the sea and the dark features decreases at high wind speeds. This is expected since high wind speeds increases the Bragg wave height, thus reducing the damping effect created by the matter on the surface. Both nothing observed and COM seems to have a negative correlation

between $\tilde{\kappa_1}$ and $\tilde{\kappa_2}$, with nothing observed clustering more towards the top right and COM clustering more towards the bottom left. It's not possible to say anything general about the mineral oil class, due to the lack of data.

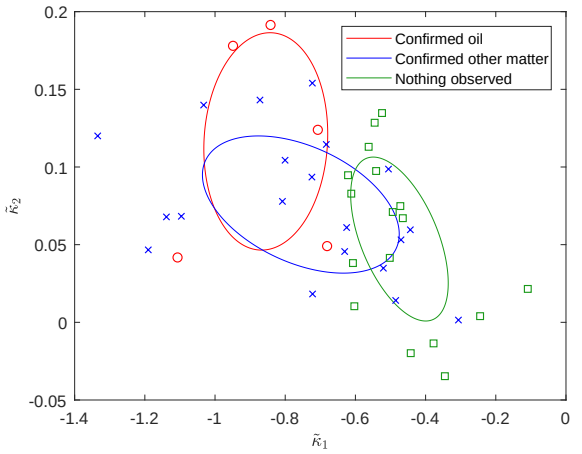

(a)

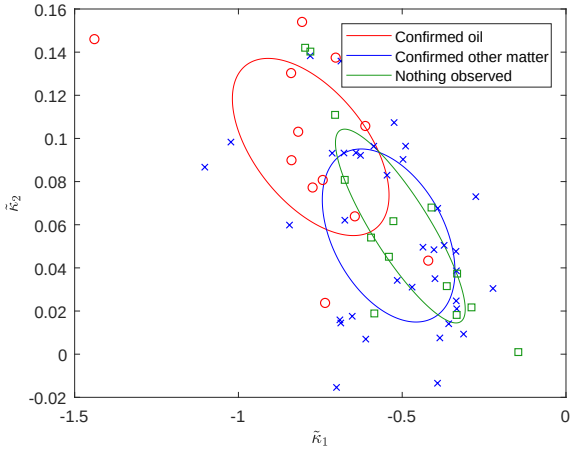

(b)

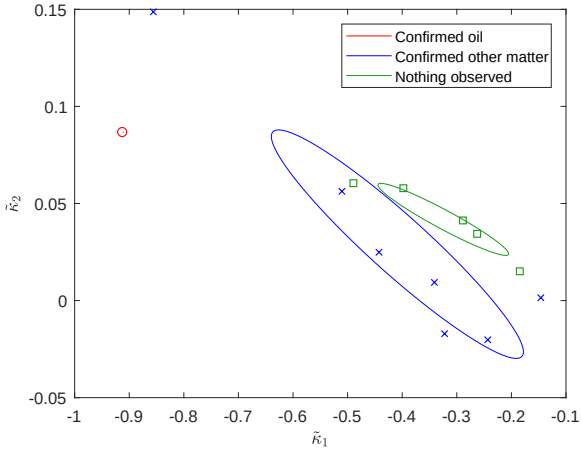

(c)

Figure 8.11: $\tilde{\kappa_2}$ plotted as a function of $\tilde{\kappa_1}$ sorted by wind speed (a) wind speed $\in$[0,4) m/s, (b) wind speed $\in$[4,8] m/s and (c) wind speed $\in$(8,14] m/s. Confirmed oil spills are denoted by red circles, COM by blue crosses and nothing observed by green squares. The ellipses represent the mean and variation for each class.

8.1.3 Summary of the Log-Cumulants Analysis

The preliminary study identified κ_1, κ_2, $\tilde{\kappa_1}$ and $\tilde{\kappa_2}$ as the parameters with the greatest potential for discriminating between mineral oil and look-alikes, and are consequently the main focus under this analysis. For RS2 ScanSAR data, the κ_1-κ_2 plot revealed no separation between the classes. Normalization seems to remove much of the spread in the data, and increase the separation between the classes, although there is still mixing. The COM class seems to produce the largest damping effect and greatest texture. Mineral oil and nothing observed both have low texture, with mineral oil producing a greater damping effect than nothing observed. Several of the COMs detected at near-range incidence angles also produce both a very large damping effect and texture, separating from the rest of the dark features. This might indicate that near-range incidence angles in the RS2 ScanSAR mode is not as well suited for mineral oil spill detection as higher incidence angles.

Only including dark features detected at mid-range incidence angles [30°,40°], leads to a slightly increased separation between the classes in $\tilde{\kappa_1}$-$\tilde{\kappa_2}$ space. The general trend in $\tilde{\kappa_1}$-$\tilde{\kappa_2}$ for these incidence angles is the same as when using the entire dataset. The majority of the RS2 ScanSAR data is detected at wind speeds below 6 m/s, implying that the analysis is limited to wind speeds below 6 m/s. By only plotting dark features detected at low wind speeds [0,2) m/s, the separation between the mineral oil and nothing observed classes are found to increase, compared to when applying all of the S1-GRDH data. Both classes seem to produce the similar texture, but mineral oil tends to produce a larger damping effect than nothing observed. The COM class looks to produce both the largest damping effect and texture both for dark features detected at [0,2) m/s and [2,4] m/s. To summarise, no clear separation are found between any of the classes for RS2. The COM class generally produces the largest texture and damping effect, it also seems like there is a negative correlation between $\tilde{\kappa_1}$ and $\tilde{\kappa_2}$ for this class. Mineral oil and noting observed generally produce the same texture, with mineral oil creating a greater damping effect.

The overall separation between the classes are found to be much better using S1 data. some separation is found in κ_1-κ_2 space using S1-GRDM data, with increased of separation being observed when using S1-GRDH data. The normalization procedure generally increases the separation between the classes. Now mineral oil tends to produce both the largest damping effect and texture. COM and nothing observed generates the similar texture, with nothing observed having the lowest damping effect. This corresponds well with what was found in [Skrunes et al., 2015a], where both crude oil and emulsion generally generated dark features with a larger damping effect and texture, compared to plant oil and natural phenomena. A negative correlation between $\tilde{\kappa_1}$ and $\tilde{\kappa_2}$ is observed for all classes. The separation between the classes further improves

when using S1-GRDH data, implying that resolution is a key parameter. Especially the separation in $\tilde{\kappa_2}$ seems to increase with resolution. The improved resolution in the S1-GRDH scenes makes it possible to detect smaller differences in radar backscatter, i.e. it is possible to detect more subtle differences in texture. This means that $\tilde{\kappa_2}$ contains more information in the S1-GRDH scenes compared to in the S1-GRDM scenes. The overall best separation is found between mineral oil and nothing observed. The COM class has a large spread in the data and tends to end up between the other classes, thus leading to mixing. Dividing the S1-GRDH dataset into subsets based on incidence angle, further increased the separation between mineral oil and nothing observed for near-range [30,35) and mid-range [35,40] incidence angles. The number of mineral oil detections are too small to conclude on the separation between mineral oil and nothing observed for far-range incidence angles. Dividing the dataset into subsets based on wind speed also seems to increase the separation between the classes. Especially wind speeds in the range [0,4) m/s seems to give clear separation between mineral oil and nothing observed, with mineral oil generating both a greater damping effect and texture than nothing observed. COM still ends up between the other classes. To summarize, a significantly better separation is found between the mineral oil and nothing observed classes using S1-GRDH data. No clear separation is found between COM and any of the other classes. Some potential for using log-cumulants to discriminate between mineral oil and nothing observed are identified, at least using S1-GRDH data. It would be of great value for companies like KSAT to be able to distinguish between mineral oil and look-alikes created by atmospheric/oceanographic phenomena.

Both sensors seems to comply with that nothing observed produces dark features with a low damping effect and little texture, but they disagree on how both mineral oil and COM behaves in relation to each other. As explained in subsection 4.2.2, it is expected form literature that mineral oil generates dark features with a greater damping effect and texture than natural films. This corresponds well with what is found from the S1-GRDH and S1-GRDM data.

8.2 Classification

This section presents the classification results, meaning that the S1-GRDM, S1-GRDH and RS2 ScanSAR data will be classified using a linear SVM (See chapter 5 for details). The analysis in section 8.1.2 proved that there were separation between mineral oil and nothing observed in $\tilde{\kappa_1}$-$\tilde{\kappa_2}$ space, the COM class are found to end up between the other classes. Mineral oil appears to be easier to separate from nothing observed than from COM, and the classification

is therefore done in two parts. Firstly, it will be tested if the SVM can separate mineral oil, COM and nothing observed, and then the classification task will be restricted to only classifying nothing observed and mineral oil.

Classification of all Three Classes

Table 8.1 shows the results obtained using the S1-GRDH data, when trying to classify all three classes using a linear SVM. The classification model completely fails and generally assigns all samples into the COM class. Only the results from using S1-GRDH data is displayed, but the classifier also failed using the S1-GRDM, S1-GRDM-2 and RS2 ScanSAR dataset. The overall goal of the classifier is to maximize the CA, and if the classes are sufficiently mixed or unbalanced, the classifiers often achieves this by assigning all samples into one class. This happens for 8 of the cases tested. For the remaining 3 cases, the classifier tries to divide the dark features into different classes, but achieves a lower CA than what could be obtained by assigning all dark features into one class.

Parameter/Case #	1	2	3	4	5	6	7	8	9	10	11
$\tilde{\kappa_1}$	x	x	x	x	x	x	x	x	x	x	x
$\tilde{\kappa_2}$	x	x	x	x	x	x	x	x	x	x	x
$\tilde{\kappa_3}$		x		x	x	x	x	x	x	x	x
κ_2		x	x	x	x	x	x	x	x	x	x
Width				x							x
Length				x							x
First Hu-moment					x			x	x	x	x
Damping ratio											x
Perimeter											x
Area										x	x
Compactness						x			x	x	x
Coefficient of variation							x	x	x	x	x
Number of objects										x	x
CA [%]	54.8	54.8	54.8	54.8	54.8	54.8	54.8	54.8	50.8	51.6	52.4

Table 8.1: The results obtained classifying all three classes using the S1-GRDH dataset, a linear SVM and 50-fold cross validation.

Classification of Mineral Oil and Nothing Observed using Quantitative Parameters

The results from classifying mineral oil and nothing observed can be seen in Table 8.2. The log-cumulants are included in all classification results. The cases 1-3 reveal that the log-cumulants performs poorly when classifying the full

S1-GRDM dataset, Figure 8.7 shows that although there is some separation between the classes, it is not enough to prevent overlapping. Overlap generally causes problems for linear classifiers, thus leading to $\bar{\kappa}$ values in the range -0.094-0.114 when only using the log-cumulants, which indicates that the result is not much better than what could be expected by chance. Case 4 involves using the width and length, in addition to log-cumulants. Width and length proves to perform well and raises the $\bar{\kappa}$ and CA to 0.351 and 74.1%, respectively. This $\bar{\kappa}$-value indicates that the classification model performs fairly good. The results from case 5 are the same as in case 2, thus indicating that the first Hu-moment does not improve the classification. The first Hu-moment essentially measures the same geometrical feature as length and width, namely elongatedness, it is unexpected that the classification results obtained using these parameters differs that much. Case 6 shows that compactness raises both $\bar{\kappa}$ and CA to 0.298 and 72.8%, thus meaning that compactness performs well in separating the classes. Case 7-9 shows that coefficient of variation and first Hu-moment does not improve the classification at all, while compactness is still found valuable. By comparing case 9 and 10, it becomes clear that including area and number of objects decreases both CA and $\bar{\kappa}$. Case 11 involves all the parameters in Table 8.2, which seems to give the overall best result using the S1-GRDM dataset. One of the advantages with a SVM is that it is very fit for solving problems with a small sample set and high dimensional data [Yan et al., 2009], compared to other classification methods. This advantage is observed here, with case 11 giving a $\bar{\kappa}$ and CA of 0.388 and 75.3%, respectively.

The S1-GRDM-2 dataset contains the same dark features as available in the S1-GRDH dataset, just in S1-GRDM format. The only difference between the S1-GRDM and S1-GRDM-2 dataset is that S1-GRDM contains 25 additional dark features (for the mineral oil and nothing observed class). As seen in Figure 8.8a, these datapoints have a better separation between mineral oil and nothing observed in $\tilde{\kappa_1}$-$\tilde{\kappa_2}$ space. This improves the classification results compared to when using the full S1-GRDM dataset, as can be seen in Table 8.2. This improvement demonstrates the sensitivity of the classification system when adding new dark features to the dataset. A larger dataset would not be that sensitive, and would allow for more definite conclusions regarding the performance of the classification system.

Parameter/Case #		1	2	3	4	5	6	7	8	9	10	11
$\tilde{\kappa_1}$		x	x	x	x	x	x	x	x	x	x	x
$\tilde{\kappa_2}$		x	x	x	x	x	x	x	x	x	x	x
$\tilde{\kappa_3}$			x		x	x	x	x	x	x	x	x
κ_2			x	x	x	x	x	x	x	x	x	x
Width					x							x
Length					x							x
First Hu-moment						x			x	x	x	x
Damping ratio												x
Perimeter												x
Area											x	x
Compactness							x			x	x	x
Coefficient of variation								x	x	x	x	x
Number of objects											x	x
CA [%]	S1-GRDM	61.7	67.9	61.7	74.1	67.9	72.8	67.9	64.2	72.8	71.6	75.3
	S1-GRDM-2	76.8	76.8	78.6	76.8	76.8	80.4	76.8	78.6	82.1	76.8	76.8
	S1-GRDH	83.9	89.3	87.5	76.8	87.5	91.1	89.3	91.1	91.1	89.3	83.9
	RS2-ScanSAR	63.5	58.1	63.5	62.2	63.5	64.9	60.8	60.8	64.9	64.9	62.2
$\bar{\kappa}$-value	S1-GRDM	-.094	.114	-.094	.351	.114	.298	.114	-.048	.313	.274	.388
	S1-GRDM-2	.462	.462	.496	.447	.462	.556	.412	.496	.591	.496	.447
	S1-GRDH	.627	.761	.652	.447	.725	.793	.761	.793	.793	.755	.617
	RS2-ScanSAR	0	-.063	0	-.01	0	.081	-.033	-.033	.133	.133	.049

Table 8.2: The results obtained classifying mineral oil and nothing observed using a linear SVM and 50-fold cross validation. GRDM, GRDM-2,GRDH and RS2 denotes the classification results obtained using the full GRDM dataset, dark features corresponding to the GRDH dataset in GRDM format, the GRDH dataset and the RS2 dataset, respectively.

The S1-GRDM-2 andS1- GRDH dataset contains the same dark features, which means that the result from these can be directly compared. The log-cumulants are able to classify the data with a higher precision, thus in case 2 for the S1-GRDH data, it creates a CA and $\bar{\kappa}$ of 89.3% and 0.761, respectively. It is difficult assessing the importance of $\tilde{\kappa_3}$ since the results are inconclusive when comparing case 2 and 3. CA and $\bar{\kappa}$ decreases when removing $\tilde{\kappa_3}$ for S1-GRDH data, while it increases for the S1-GRDM-2 data. When including the width and length as parameters, CA and $\bar{\kappa}$ decreases to 76.8% and 0.447 both for S1-GRDH and S1-GRDM-2 data. In contrast to what was found when analysing the full S1-GRDM dataset, these parameters are not found to increase CA or $\bar{\kappa}$ using S1-GRDM-2 and S1-GRDH data. Neither the first Hu-moment or the coefficient of variation seems to have any serious impact on the classification result in case 5 and 7, but by combining them and using the S1-GRDH data leads to a CA and $\bar{\kappa}$ of 91.1% and 0.793 in case 8, respectively. This $\bar{\kappa}$ value corresponds to a good/very good classification according to Table 5.1. Compactness is once again identified as useful parameter, producing a CA of 91.1% and 80.4%, as well as $\bar{\kappa}$-value of 0.793 and 0.556 using the S1-GRDH and S1-GRDM-2 data,

respectively. Combining compactness, the first Hu-moment and coefficient of variation improved the classification even further for the S1-GRDM-2 dataset, producing a CA and $\bar{\kappa}$ of 82.1% and 0.591 , respectively. All parameters are used in case 11, which leads to a decrease in CA and $\bar{\kappa}$. It is interesting that the results from the S1-GRDM and S1-GRDM-2 dataset approaches each other when combining all parameters. The classification results using RS2 data mostly give a $\bar{\kappa}$ value around 0, which means that the classifier performs no better than what could be expected by chance.

The classification results obtained without using log-cumulants are displayed in Table 8.3. The S1-GRDM dataset still proves to be difficult to classify, with the $\bar{\kappa}$-value ranging from 0-0.298. Case 2 provided the best classification result, which includes all parameters except the damping-ratio. A $\bar{\kappa}$ value of 0.298 corresponds to a fair agreement between the classification model and the true values. The results obtained when using the log-cumulants was slightly better. Only including the first Hu-moment and compactness resulted in a CA and $\bar{\kappa}$ of 72.8% and 0.283, respectively. By adding the coefficient of variation the classification completely fails, producing a $\bar{\kappa}$ equal to zero. The coefficient of variation generally seems to create poor classification results, which might be explained by the resolution of the data used here. This parameter is related to both texture and radar backscatter, and it is expected that texture increases with resolution. This parameter might be more useful for data with increased resolution.

As was the case when using log-cumulants, the classification results improves when using the S1-GRDM-2 and S1-GRDH dataset compared to the S1-GRDM dataset. The results from the S1-GRDH dataset is still superior to the results from the other datasets, further underlining the importance of using high resolution data when classifying dark features. The comparison of case 1 and 2 in Table 8.3 reveals that damping ratio does not aid the classification result in either the S1-GRDM, S1-GRDM-2 or S1-GRDH dataset. The damping ratio is strongly related to $\tilde{\kappa_1}$, and it is unexpected that this parameter does not contribute more. The comparison of case 3 and 4 indicates that the first Hu-moment is more valuable than width and length for S1-GRDH data, while width and length is found slightly more helpful for S1-GRDM and S1-GRDM-2 data. It is unanticipated that these parameters should be that dependent on resolution, especially the first Hu-moment, which is scale invariant. Comparing case 5 and 6 in Table 8.3, further confirms the usefulness of the first Hu-moment. The overall best classification result obtained both in Table 8.2 and 8.3 using the S1-GRDM-2 and S1-GRDH dataset, is produced using the first Hu-moment, compactness and coefficient of variation. These parameters classified with an accuracy of 91.1% and a $\bar{\kappa}$ of 0.798 using the S1-GRDH data, and with an accuracy of 83.9% and $\bar{\kappa}$ of 0.627 using the S1-GRDM-2 data. Both $\bar{\kappa}$-values are the highest obtained for these datasets. Using the same parameters to classify

the S1-GRDM dataset produces a $\bar{\kappa}$-value of zero, further highlighting the sensitivity of this classification system to the introduction of new dark features to the dataset. It is very surprising that the performance of the classification system deteriorate that much by adding 25 extra dark features to the dataset. Case 7-9 shows that the coefficient of variation is not as useful as the first Hu-moment and compactness, since both CA and $\bar{\kappa}$ is greater in case 9 than both 7 and 8 using the S1-GRDH and S1-GRDM-2 dataset.

Parameter/Case #		1	2	3	4	5	6	7	8
Width		x	x		x				
Length		x	x		x				
First Hu-moment		x	x	x		x		x	x
Damping ratio		x							
Perimeter		x	x	x	x				
Area		x	x						
Compactness		x	x	x	x	x	x		x
Coefficient of variation		x	x	x	x	x	x	x	
Number of objects		x	x	x	x				
CA [%]	S1-GRDM	71.6	72.8	69.1	71.6	66.7	66.7	64.2	72.8
	S1-GRDM-2	76.8	82.1	75.0	75.0	83.9	67.9	78.6	83.9
	S1-GRDH	82.1	82.1	85.7	78.6	91.1	73.2	82.1	89.3
	RS2 ScanSAR	64.9	56.8	56.8	59.5	66.2	63.5	63.5	67.6
$\bar{\kappa}$-value	S1-GRDM	.274	.298	.211	.258	0	0	-.048	.283
	S1-GRDM-2	.496	.569	.412	.361	.627	.223	.496	.627
	S1-GRDH	.569	.569	.673	.452	.798	.344	.591	.755
	RS2	.133	-.030	-.030	.034	.158	.074	0	.199

Table 8.3: The results obtained classifying mineral oil and nothing observed using a linear SVM and 50-fold cross validation, without using log-cumulants. S1-GRDM, S1-GRDM-2,S1-GRDH and RS2 denotes the classification results obtained using the full S1-GRDM dataset, dark features corresponding to the S1-GRDH dataset in S1-GRDM format, the S1-GRDH dataset and the RS2 dataset, respectively.

Classification of Mineral Oil and Nothing Observed using Parameters Available in the Detection Report

Table 8.4 shows the classification result from using parameters available in KSATs detection rapport in addition to the log-cumulants. These parameters are only tested using the S1-GRDH dataset, since this dataset proved to give the best result in Tables 8.2 8.3. Contrast, edge, natural slicks in vicinity, angular shape, droplet shape, feathered shape, patch shape, tail shape, winding

shape, outline, texture and shape related to wind history are all qualitative parameters, with the rest being quantitative parameters. Case 1-7 involves using log-cumulants in addition to these parameters, where the overall best results are obtained only using log-cumulants. This indicates that neither the contrast, edge, texture or any of the shape parameters adds any useful information to the information already contained within the log-cumulants, leading to more misclassifications. In case 6, the log-cumulants, contrast, edge, shape parameters, outline and texture are all included, leading to a CA and $\bar{\kappa}$ of 73.2% and 0.395, which is a noticeably worse result than obtained just using the log-cumulants. Including all the parameters produced a $\bar{\kappa}$ close to zero. However, this result could be caused by a phenomena often referred to as "the curse of dimensionality", which relates to phenomena that arise when analysing data in high dimensions, thus leading to poor classification results. As mentioned earlier, the SVM is especially robust when dealing with high dimensional data, although it could be that 20 parameters using such a small dataset is to much to handle, even for the SVM. The results actually improves when only using the parameters available in the detection report from KSAT, i.e. when the log-cumulants are removed. This further suggests that the main problem in case 7 is that there are too many parameters, since the log-cumulants are identified as valuable parameters in previous classification cases. Comparing case 6 and 8 further confirms the value of log-cumulants, including log-cumulants improves both the CA and $\bar{\kappa}$ from 58.9% and -0.035 to 73.2% and 0.395, respectively. This also indicates that the value of the qualitative parameters used here are limited. Width, length, area and wind speed (case 10) produces acceptable results, although not as good as the log-cumulants.

Parameter/Case #	1	2	3	4	5	6	7	8	9	10
$\tilde{\kappa_1}$	x	x	x	x	x	x	x			
$\tilde{\kappa_2}$	x	x	x	x	x	x	x			
$\tilde{\kappa_3}$	x	x	x	x	x	x	x			
κ_2	x	x	x	x	x	x	x			
Width							x		x	x
Length							x		x	x
Contrast		x				x	x	x	x	
Edge			x			x	x	x	x	
Natural slick in vicinity							x		x	
Angular shape					x	x	x	x	x	
Droplet shape					x	x	x	x	x	
Feathered shape					x	x	x	x	x	
Patch shape					x	x	x	x	x	
Tail shape					x	x	x	x	x	
Winding shape					x	x	x	x	x	
Outline						x	x	x	x	
Shape related to wind history							x		x	
Texture				x		x	x	x	x	
Wind SARtool							x		x	x
Area							x		x	x
CA [%]	89.3	87.5	85.7	85.7	78.6	73.2	66.1	58.9	73.2	76.8
$\bar{\kappa}$-value	.761	.718	.681	.673	.522	.395	.191	-.035	.305	.397

Table 8.4: The results obtained classifying mineral oil and nothing observed using the S1-GRDH dataset, a linear SVM and 50-fold cross validation.

8.2.1 Summary of the Classification Results

This section summarizes the classification results obtained in section 8.2. The classification system is found to completely fail when trying to classify all three classes. The main problem seems to be the COM class, which consists of a variety of matters, thus mixing with both the mineral oil and the nothing observed class. The nothing observed class constitutes about 2/3 of the in-situ observations made in the CSN program in the period 2015-2017, which makes it a pressing manner to remove at least some of these detections. The log-cumulant analysis indicated that these are easier to separate from mineral oil than COM. Only trying to separate mineral oil and nothing observed also produce better classification results, although it is found that the performance are very dependent on the data used. The classification of the RS2 ScanSAR dataset give for the most part a $\bar{\kappa}$-value close to zero. This indicates that the results are no better than what could be expected by chance. The best results are obtained using only compactness and the first Hu-moment, which give a $\bar{\kappa}$-value of 0.199 using this sensor. The S1-GRDM dataset produces a bit

better classification results, with length, width and compactness proving to be valuable parameters. The classification fails when only using log-cumulants. The overall best result using this dataset is obtained using all parameters available in Table 8.2, which give a $\bar{\kappa}$-value of 0.388. This corresponds to a fair/moderate strength of agreement between the classification and the true class labels.

The S1-GRDM-2 dataset produces better classification results than the S1-GRDM dataset, with the first Hu-moment, compactness and coefficient of variation standing out as the most useful parameters. Using these parameters, the SVM is able to produce a classification result with a $\bar{\kappa}$-value of 0.627. This corresponds to a good/moderate correlation between the classification and the true class labels. The classification of the S1-GRDH dataset proves to give the overall best result. Several variations of using the log-cumulants, first Hu-moment, compactness and coefficient of variation in the SVM produce a CA of 91.1%. The highest $\bar{\kappa}$-value is 0.798, and is produced using the first Hu-moment, compactness and coefficient of variation. This $\bar{\kappa}$ corresponds to a good/very good correlation between the classification and true class labels. The S1-GRDM-2 and the S1-GRDH dataset both contains the same dark features, meaning that the results from these are directly comparable. The comparison of these datasets underline the importance of resolution when trying to discriminate between mineral oil and nothing observed. Nevertheless, the difference between the S1-GRDM and S1-GRDM-2 dataset gives reason for concern, since introducing 25 new dark features has a large impact on the classification results. It also raises the question, would the classification result for the S1-GRDH data be as good if all of the masks were successfully moved to the S1-GRDH format, i.e. the S1-GRDH dataset contained the same dark features as the S1-GRDM dataset? A larger dataset would make it possible to make more definite conclusions regarding the potential of this classification system.

Most of the parameters found in KSATs detection report are not found very useful in this classification system, as limited potential is identified for the qualitative parameters. Examples are shown in Figures 7.7c-7.7h, where the "variable" category is strongly represented, with no class standing out from the others in this category, leading to an overall poor separation. These parameters are set manually by a operator, who has to deliver a complete oil spill report within 30 minutes of acquiring the SAR product. The human involvement results in subjective parameters, meaning that the parameters can change based on who the operator is. Qualitative measures are generally not able to detect smaller changes in a parameter, meaning that some information is lost contra using quantitative parameters. Many of the parameters suggested in Tables 8.1-8.3, describes the same slick properties as the parameters from KSATs detection report. These parameters seems to perform better, and may

make it possible to automate more of KSATs oil detection service, which could make KSAT able to deliver their oil detection service quicker. However, more testing of these parameters on larger datasets would be required before making a final verdict on their performance.

9 Conclusions

The objective of this thesis was to investigate the potential for discrimination between marine oil spills and look-alikes, using several parameters describing the characteristics of a dark feature. This work consist of two main parts. First the potential for using log-cumulant diagrams for separation of mineral oil and look-alikes was explored. Then a SVM classification system was built and used to evaluate the discrimination potential of different parameters. These parameters both includes qualitative descriptors currently used by KSAT, and parameters from the literature that quantitatively describes the same properties of the dark feature as KSATs parameters. Two datasets containing dark features detected and reported by KSAT through their oil spill detection service, have been investigated. The first dataset contains dark features detected using RS2 in ScanSAR mode. The second dataset includes dark features detected using S1 in IW mode, which are available in two formats, S1-GRDM and S1-GRDH, with different resolution and degree of multilooking. Feedback reports are also provided by KSAT, providing in-situ information about each detection. This knowledge is applied to divide the dark detections into three main classes, namely dark features created by mineral oil, other matters on the surface (referred to as COM) and detections where nothing was found (referred to as nothing found), it is assumed that these dark features are created by atmospheric/oceanographic phenomena.

Log-Cumulant Analysis

$\tilde{\kappa_1}$ and $\tilde{\kappa_2}$, which denotes the normalized first and second order log-cumulant, were identified in the preliminary study as the log-cumulants with greatest potential for discrimination of mineral oil and look-alikes, thus leading to a more extensive analysis of these parameters in this thesis. $\tilde{\kappa_1}$ and $\tilde{\kappa_2}$ measures the damping effect and texture produced by the dark feature, respectively. The normalization procedure normalizes the log-cumulants against the sea state, and proved to be vital to obtain any separation between the classes. No significant separation between any of the classes was found using RS2 ScanSAR data. On the other hand, some potential for discrimination of mineral oil and nothing observed was identified using both S1-GRDH and S1-GRDM data, although S1-GRDH definitely gave the overall best separation. Diving the S1-GRDH dataset into subsets based on incidence angle and wind-speed further increased the separation between the mineral oil and nothing observed classes. The log-cumulant analysis of the S1-GRDH data reveals that mineral oil appears to create the greatest damping effect and texture. Nothing observed and COM are found to generate dark features with similar texture, though with the nothing observed class producing the lowest damping effect. These findings corresponds well with what has previously been observed for high-resolution, multi-polarization SAR data. To the authors knowledge, this is the first log-cumulant analysis performed on data used operationally by the oil detection services. It reveals some potential for using log-cumlants to discriminate between mineral oil and look-alikes created by atmospheric/oceanographic phenomena.

Classification Result

The SVM classification model was applied to quantify the separability obtained in parameter space. The SVM was not able to successfully classify all three classes. The COM class is composed of a variety of different phenomena, spreading all over the parameter space, leading to an overall bad classification. The results improved significantly when restricting the classification to only include mineral oil and nothing observed, i.e., when distinguishing between mineral oil and look-alikes created by atmospheric/oceanographic phenomena. This would be of great interest for companies likes KSAT. It was found that the performance of the classification system was very dependent on the data used. The classification results obtained using RS2 ScanSAR data was not much better than what could be expected by chance. The results improved using the S1 data, with the overall best results being generated using the S1-GRDH format, thus implying that it is preferable to limit the degree of multilooking and maintain a high resolution when classifying dark features. A variety of parameters was tested during the classification process. This includes descrip-

tors currently applied in KSATs detection service and quantitative parameters selected from literature that describes several of the same characteristics. The normalized first order log-cumulant, compactness, the first Hu-moment and the coefficient of variation were identified as the most promising parameters. The last three of these descriptors achieved the overall best classification results, which corresponded to a CA of 91.1% and a kappa statistics score of 0.798, for S1-GRDH data. Using all of the parameters currently used in KSATs oil detection service, produced a CA of 73.2% and a kappa statistics score of 0.305, using the same data. This leads to the conclusion that quantitative and objective parameters performs better and more consistent in comparison to qualitative and subjective parameters, when measuring the same property. In addition, objective parameters would not require any human intervention into the classification system, which could make it possible to speed up the classification process. Reducing the time from acquiring the SAR product to the detection report being completed would be essential for KSATs oil detections service, due to their strict requirements with respect to time.

9.1 Future Work

The different separability obtained using RS2 and S1 demonstrates the sensitivity of the log-cumulants, and the other parameters to the data type used. More research should be done on this dataset, to further explore why the results are that dependent on the sensor. A negative correlation between $\tilde{\kappa_1}$ and $\tilde{\kappa_2}$ was observed throughout the log-cumulant analysis, more research could be conducted to explore this relationship. The parameters used in this work could with benefit be further tested on other sensors, including sensors utilizing other frequency bands. Some of the results from the log-cumulant analysis indicates that a part of the dark features have a signal strength close to the noise floor. A complete noise analysis on the dataset could be conducted to test if this is can explain why the results varies that much between the sensors. It is worth mentioning that a noise analysis was conducted on the RS2 dataset in the preliminary study, which revealed that there was several dark features close to the noise floor, although removing these didn't lead to any significant improvement in the separation between the classes.

The difference between the classification results obtained using the full S1-GRDM dataset and S1-GRDM subset indicates that the classification system is very sensitive to having new data added to it. This implies that the dataset ideally should contain more dark features. This would make it possible to make a more definite conclusion regarding the performance of the classification system. In addition, a larger dataset would allow for testing of a neural network, and to see if it could produce better classification results. More research could be

done on the parameters suggested in this thesis, such that it would be possible to make a ranking of the parameters. The first Hu-moment and compactness, which both measures the shape of a dark feature, was both found to be among the most promising parameters in this thesis. A more extensive analysis of these parameters could reveal if there is any class specific shape produced by mineral oil and by look-alikes, and if this could be used to help discriminate them.

Bibliography

[Alpers et al., 2017] Alpers, W., Holt, B., and Zeng, K. (2017). Oil Spill Detection by Imaging Radars: Challenges and Pitfalls. *Remote Sensing of Environment*, 201:133–147.

[Anfinsen and Eltoft, 2011] Anfinsen, S. N. and Eltoft, T. (2011). Application of the Matrix-Variate Mellin Transform to Analysis of Polarimetric Radar Images. *IEEE Transactions on Geoscience and Remote Sensing*, 49(6):2281–2295.

[Brekke, 2007] Brekke, C. (2007). Automatic Screening of Synthetic Aperture Radar Imagery for Detection of Oil Pollution in the Marine Environment. *Unpublished Ph. D. dissertation, Faculty of Mathematics and Natural Science, Univ. Oslo*.

[Brekke and Solberg, 2005] Brekke, C. and Solberg, A. H. (2005). Oil Spill Detection by Satellite Remote Sensing. *Remote sensing of environment*, 95(1):1–13.

[Campbell and Wynne, 2011] Campbell, J. B. and Wynne, R. H. (2011). *Introduction to Remote Sensing, Fifth Edition*. Guilford Press.

[CCRS, 2007] CCRS (2007). Canada Centre for Remote Sensing. Fundamentals of Remote Sensing. http://www.nrcan.gc.ca/sites/www.nrcan.gc.ca/files/earthsciences/pdf/resouce/tutor/fundam/pdf/fundamentals_e.pdf. Visited 10. Oct. 2017.

[Cohen, 1960] Cohen, J. (1960). A Coefficient of Agreement for Nominal Scales. *Educational and psychological measurement*, 20(1):37–46.

[De Zan and Guarnieri, 2006] De Zan, F. and Guarnieri, A. M. (2006). TOPSAR: Terrain Observation by Progressive Scans. *IEEE Transactions on Geoscience and Remote Sensing*, 44(9):2352–2360.

[Del Frate et al., 2000] Del Frate, F., Petrocchi, A., Lichtenegger, J., and Cal-

abresi, G. (2000). Neural Networks For Oil Spill Detection using ERS-SAR Data. *IEEE Transactions on geoscience and remote sensing*, 38(5):2282–2287.

[Dettwiler et al., 2008a] Dettwiler, M. et al. (2008a). RADARSAT-2. https://mdacorporation.com/geospatial/international/satellites/RADARSAT-2. Visited 01. Des. 2017.

[Dettwiler et al., 2008b] Dettwiler, M. et al. (2008b). RADARSAT-2 Product Format Definition. *Macdonald, Dettwiler and Associates Ltd.: Richmond, BC, Canada*.

[Dettwiler et al., 2016] Dettwiler, M. et al. (2016). RADARSAT-2 Product Description. *Macdonald, Dettwiler and Associates Ltd.: Richmond, BC, Canada*.

[El-Darymli et al., 2014] El-Darymli, K., McGuire, P., Gill, E., Power, D., and Moloney, C. (2014). Understanding the Significance of Radiometric Calibration for Synthetic Aperture Radar Imagery. In *Electrical and Computer Engineering (CCECE), 2014 IEEE 27th Canadian Conference on*, pages 1–6. IEEE.

[Elachi and Van Zyl, 2006] Elachi, C. and Van Zyl, J. J. (2006). *Introduction to the Physics and Techniques of Remote Sensing, Second Edition*. John Wiley & Sons.

[EMSA, 2017] EMSA (2017). European Maritime Safety Agency. the CleanSeaNet Service Brochure. http://www.emsa.europa.eu/csn-menu/items.html?cid=122&id=2123. Visited 15. Oct. 2017.

[ESA, 2017a] ESA (2017a). European Space Agency Sentinel Copernicus. Level-1 Radiometric Calibration. https://sentinels.copernicus.eu/web/sentinel/radiometric-calibration-of-level-1-products. Visited 15. Oct. 2017.

[ESA, 2017b] ESA (2017b). Sentinel-1 Fact Sheet. http://esamultimedia.esa.int/docs/EarthObservation/Sentinel-1_sheet_170321.pdf. Visited 01. Des. 2017.

[ESA, 2017c] ESA (2017c). Sentinel-1 IW-Mode. https://sentinel.esa.int/web/sentinel/user-guides/sentinel-1-sar/acquisition-modes/interferometric-wide-swath. Visited 30. Apr. 2018.

[ESA, 2018] ESA (2018). SciHub - The Copernicus Open Access Hub. https://scihub.copernicus.eu/dhus/#/home. Visited 11. May. 2018.

[Espedal, 1999a] Espedal, H. (1999a). Detection of Oil Spill and Natural Film

in the Marine Environment by Spaceborne SAR. In *Geoscience and Remote Sensing Symposium, 1999. IGARSS'99 Proceedings. IEEE 1999 International*, volume 3, pages 1478–1480. IEEE.

[Espedal, 1999b] Espedal, H. (1999b). Satellite SAR Oil Spill Detection using Wind History Information. *International Journal of Remote Sensing*, 20(1):49–65.

[Espedal et al., 1998] Espedal, H. A., Johannessen, O. M., Johannessen, J. A., Dano, E., Lyzenga, D., and Knulst, J. (1998). COASTWATCH'95: ERS 1/2 SAR Detection of Natural Film on the Ocean Surface. *Journal of Geophysical Research: Oceans*, 103(C11):24969–24982.

[Fiscella et al., 2000] Fiscella, B., Giancaspro, A., Nirchio, F., Pavese, P., and Trivero, P. (2000). Oil Spill Detection using Marine SAR Images. *International Journal of Remote Sensing*, 21(18):3561–3566.

[Gade et al., 1998] Gade, M., Alpers, W., Hühnerfuss, H., Masuko, H., and Kobayashi, T. (1998). Imaging of Biogenic and Anthropogenic Ocean Surface Films by the Multifrequency/Multipolarization SIR-C/X-SAR. *Journal of Geophysical Research: Oceans*, 103(C9):18851–18866.

[GESAMP, 2007] GESAMP (2007). *Estimates of Oil Entering the Marine Environment from Sea-Based Activities*. International Maritime Organization.

[Gonzalez and Woods, 2012] Gonzalez, R. C. and Woods, R. E. (2012). Digital Image Processing.

[Holt, 2004] Holt, B. (2004). *SAR Users Manual Chapter 2: SAR Imaging of the Ocean Surface*.

[Hovland et al., 1994] Hovland, H. A., Johannessen, J. A., and Digranes, G. (1994). Slick Detection in SAR Images. In *Geoscience and Remote Sensing Symposium, 1994. IGARSS'94. Surface and Atmospheric Remote Sensing: Technologies, Data Analysis and Interpretation., International*, volume 4, pages 2038–2040.

[Hu, 1962] Hu, M.-K. (1962). Visual Pattern Recognition by Moment Invariants. *IRE transactions on information theory*, 8(2):179–187.

[KSAT, 2017] KSAT (2017). Kongsberg Satellite Services Brochure. http://www.ksat.no/en/about%20us/. Visited 15. Oct. 2017.

[Kuruoglu and Zerubia, 2004] Kuruoglu, E. E. and Zerubia, J. (2004). Model-

ing SAR Images with a Generalization of the Rayleigh Distribution. *IEEE Transactions on Image Processing*, 13(4):527–533.

[Lee and Pottier, 2009] Lee, J.-S. and Pottier, E. (2009). *Polarimetric Radar Imaging: from Basics to Applications*. CRC press.

[Marston, 2009] Marston, L. (2009). *Introductory Statistics for Health and Nursing using SPSS*. Sage.

[MatLab, 2018] MatLab (2018). MatLab Classification Learner. https://se.mathworks.com/help/stats/classificationlearner-app.html. Visited 20. May. 2018.

[McCandless and Jackson, 2004] McCandless, S. W. and Jackson, C. (2004). *SAR Users Manual Chapter 1: Principles of Synthetic Aperture Radar*.

[Migliaccio et al., 2007] Migliaccio, M., Gambardella, A., and Tranfaglia, M. (2007). SAR Polarimetry to Observe Oil Spills. *IEEE Transactions on Geoscience and Remote Sensing*, 45(2):506–511.

[National Research Council, 2003] National Research Council (2003). *Oil in the Sea III: Inputs, Fates, and Effects*. The National Academies Press, Washington, DC.

[Nicolas, 2002] Nicolas, J.-M. (2002). Introduction aux Statistiques de Deuxième espèce: Applications des Logs-Moments et des Logs-Cumulants à l'analyse des lois d'images Radar. *TS. Traitement du signal*, 19(3):139–167.

[Nicolas and Anfinsen, 2002] Nicolas, J.-M. and Anfinsen, S. N. (2002). Introduction to Second Kind Statistics: Application of Log-Moments and Log-Cumulants to the Analysis of Radar Image Distributions. Technical note, translation from French of [Nicolas, 2002]. URL: http://eo.uit.no/publications/jmn-trans-12.pdf, Visited 28. Nov. 2017.

[Nixon and Aguado, 2002] Nixon, M. and Aguado, A. (2002). *Feature Extraction and Image Processing*. Electronics & Electrical. Newnes.

[Raney, 2016] Raney, R. (2016). Comparing Compact and Quadrature Polarimetric SAR Performance. *IEEE Geoscience and Remote Sensing Letters*, 13(6):861–864.

[Shi et al., 2008] Shi, L., Zhao, C., Fan, K., Shi, Y., and Liu, P. (2008). Texture Feature Application in Oil Spill Detection by Satellite Data. In *Image and Signal Processing, 2008. CISP'08. Congress on*, volume 4, pages 784–788.

IEEE.

[Simard et al., 1998] Simard, M., DeGrandi, G., Thomson, K. P., and Benie, G. B. (1998). Analysis of Speckle Noise Contribution on Wavelet Decomposition of SAR Images. *IEEE Transactions on Geoscience and Remote Sensing*, 36(6):1953–1962.

[Skrunes, 2014] Skrunes, S. (2014). Characterization of Low Backscatter Regions in the Marine Environment by Multipolarization C-and X-band Synthetic Aperture Radar Data. Ph.D. thesis, University of Tromsø, Norway.

[Skrunes et al., 2015a] Skrunes, S., Brekke, C., and Doulgeris, A. P. (2015a). Characterization of Low-Backscatter Ocean Features in Dual-Copolarization SAR using Log-Cumulants. *IEEE Geoscience and Remote Sensing Letters*, 12(4):836–840.

[Skrunes et al., 2015b] Skrunes, S., Brekke, C., Eltoft, T., and Kudryavtsev, V. (2015b). Comparing Near-Coincident C-and X-Band SAR Acquisitions of Marine Oil Spills. *IEEE Transactions on Geoscience and Remote Sensing*, 53(4):1958–1975.

[Solberg et al., 1999] Solberg, A. S., Storvik, G., Solberg, R., and Volden, E. (1999). Automatic Detection of Oil Spills in ERS SAR Images. *IEEE Transactions on geoscience and remote sensing*, 37(4):1916–1924.

[Theodoridis and Koutroumbas, 2008] Theodoridis, S. and Koutroumbas, K. (2008). *Pattern Recognition, Fourth Edition*. Academic Press, 4th edition.

[Thompson et al., 1998] Thompson, D. R., Elfouhaily, T. M., and Chapron, B. (1998). Polarization Ratio for Microwave Backscattering from the Ocean Surface at Low to Moderate Incidence Angles. In *Geoscience and Remote Sensing Symposium Proceedings, 1998. IGARSS'98. 1998 IEEE International*, volume 3, pages 1671–1673. IEEE.

[Topouzelis et al., 2009] Topouzelis, K., Stathakis, D., and Karathanassi, V. (2009). Investigation of Genetic Algorithms Contribution to Feature Selection for Oil Spill Detection. *International Journal of Remote Sensing*, 30(3):611–625.

[Topouzelis, 2008] Topouzelis, K. N. (2008). Oil Spill Detection by SAR Images: Dark Formation Detection, Feature Extraction and Classification Algorithms. *Sensors*, 8(10):6642–6659.

[Ulaby et al., 1982] Ulaby, F. T., Moore, R. K., and Fung, A. K. (1982). Mi-

crowave Remote Sensing Active and Passive-Volume ii: Radar Remote Sensing and Surface Scattering and Emission Theory.

[Valenzuela, 1978] Valenzuela, G. R. (1978). Theories for the Interaction of Electromagnetic and Oceanic Waves—a Review. *Boundary-Layer Meteorology*, 13(1-4):61–85.

[Wolff, 2017] Wolff, C. (2017). Radar Tutorial - the Radar Range Equation. http://www.radartutorial.eu/01.basics/The%20Radar%20Range%20Equation.en.html#this. Visited 06. Nov. 2017.

[Yan et al., 2009] Yan, F., Mei, W., and Chunqin, Z. (2009). SAR Image Target Recognition Based on Hu Invariant Moments and SVM. In *Information Assurance and Security, 2009. IAS'09. Fifth International Conference on*, volume 1, pages 585–588. IEEE.

Appendices

A Analysis of log-cumulants using RS2 data

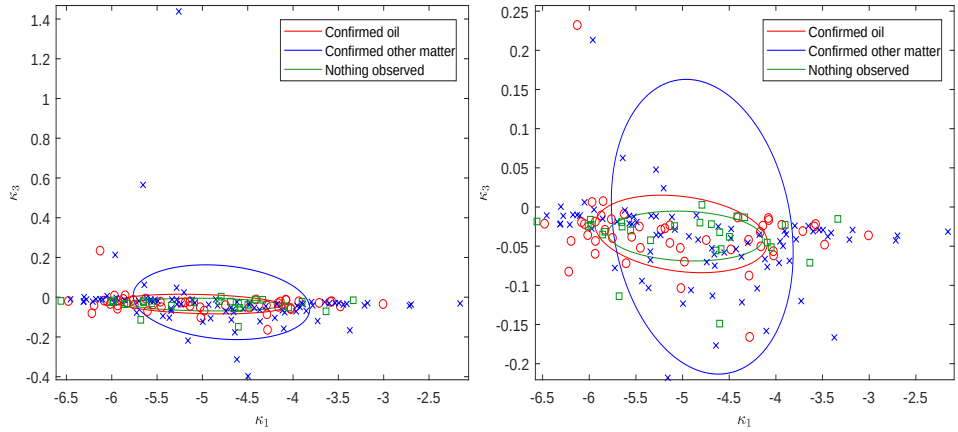

(a) **(b)**

Figure A.1: κ_3 plotted as a function of κ_1. Confirmed oil spills are denoted by red circles, COM by blue crosses and nothing observed by green squares. The ellipses represent the mean and variation for each class. (a) contains all the data, while (b) is a zoomed version.

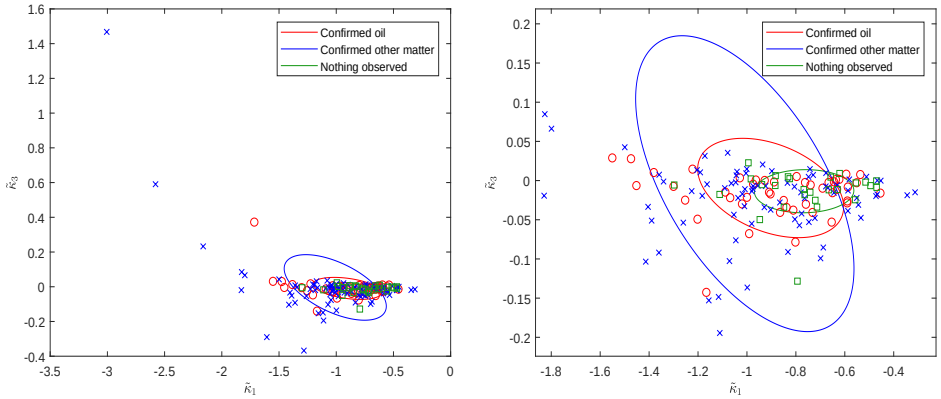

(a) **(b)**

Figure A.2: $\tilde{\kappa_3}$ plotted as a function of $\tilde{\kappa_1}$. Confirmed oil spills are denoted by red circles, COM by blue crosses and nothing observed by green squares. The ellipses represent the mean and variation for each class. (a) contains all the data, while (b) is a cropped version.

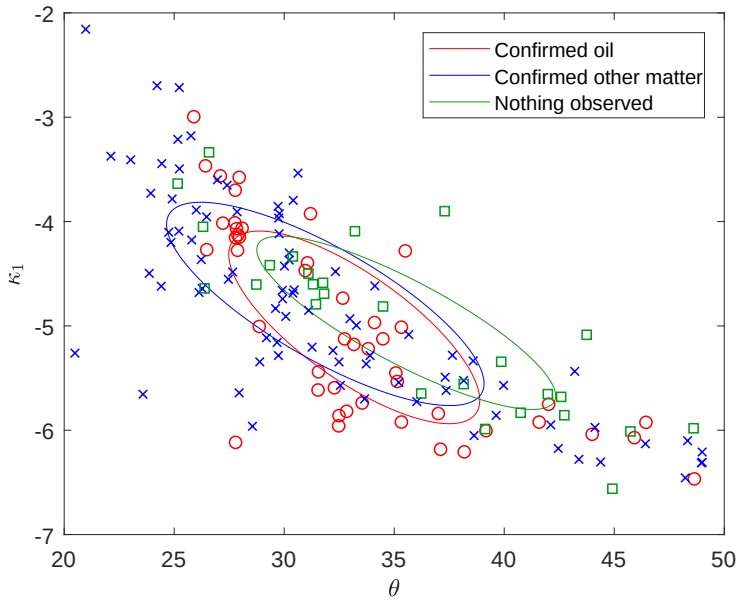

Figure A.3: κ_1 plotted as a function of θ. Confirmed oil spills are denoted by red circles, COM by blue crosses and nothing observed by green squares. The ellipses represent the mean and variation for each class.

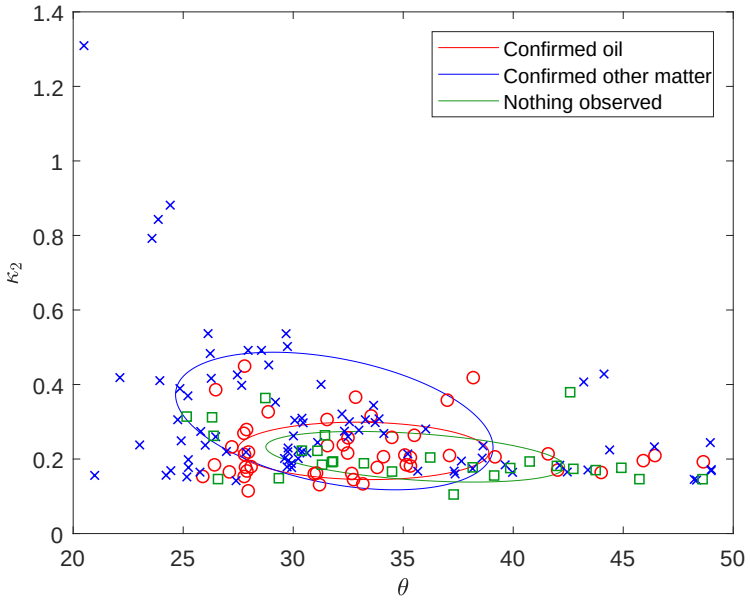

Figure A.4: κ_2 plotted as a function of θ. Confirmed oil spills are denoted by red circles, COM by blue crosses and nothing observed by green squares. The ellipses represent the mean and variation for each class.

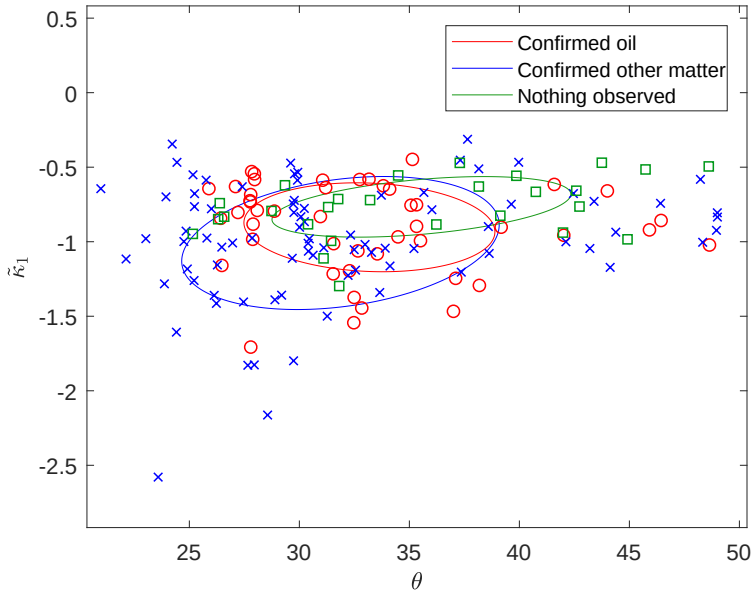

Figure A.5: $\tilde{\kappa_1}$ plotted as a function of θ. Confirmed oil spills are denoted by red circles, COM by blue crosses and nothing observed by green squares. The ellipses represent the mean and variation for each class.

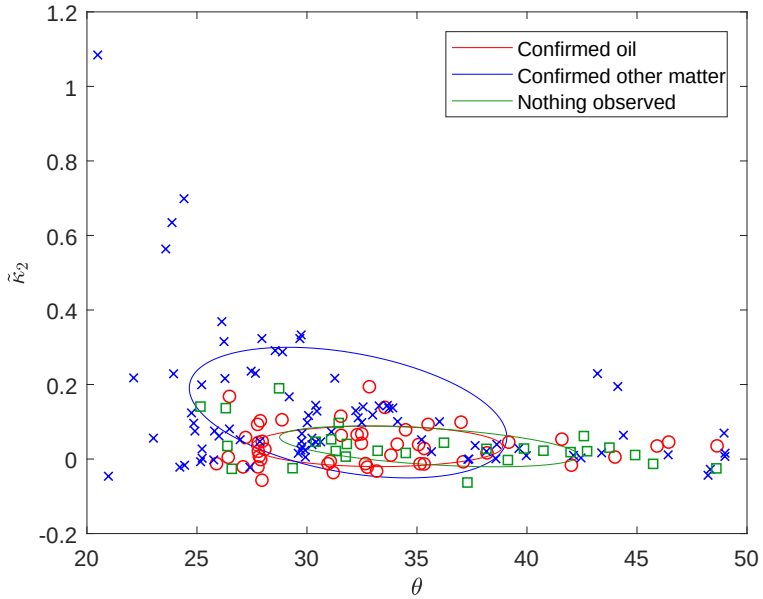

Figure A.6: $\tilde{\kappa_2}$ plotted as a function of θ. Confirmed oil spills are denoted by red circles, COM by blue crosses and nothing observed by green squares. The ellipses represent the mean and variation for each class.

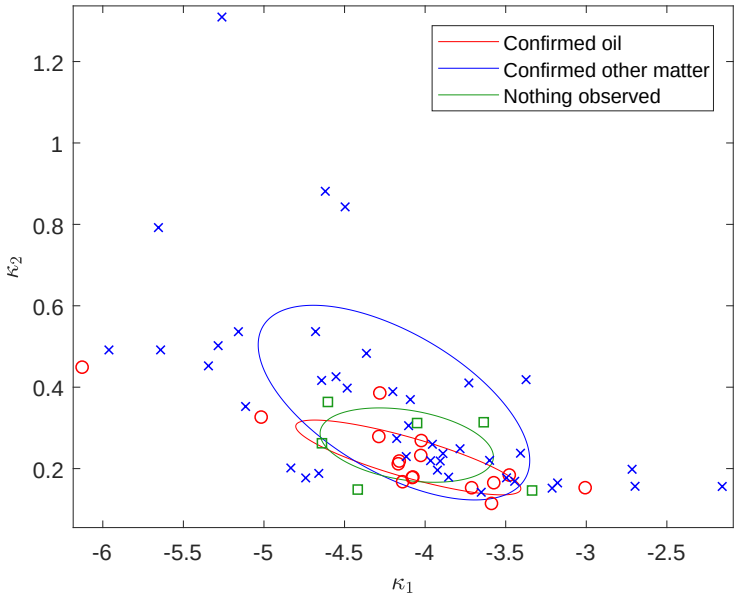

Figure A.7: κ_2 plotted as a function of κ_1, for dark features with incidence angle in the interval [19°,30°). Confirmed oil spills are denoted by red circles, COM by blue crosses and nothing observed by green squares. The ellipses represent the mean and variation for each class.

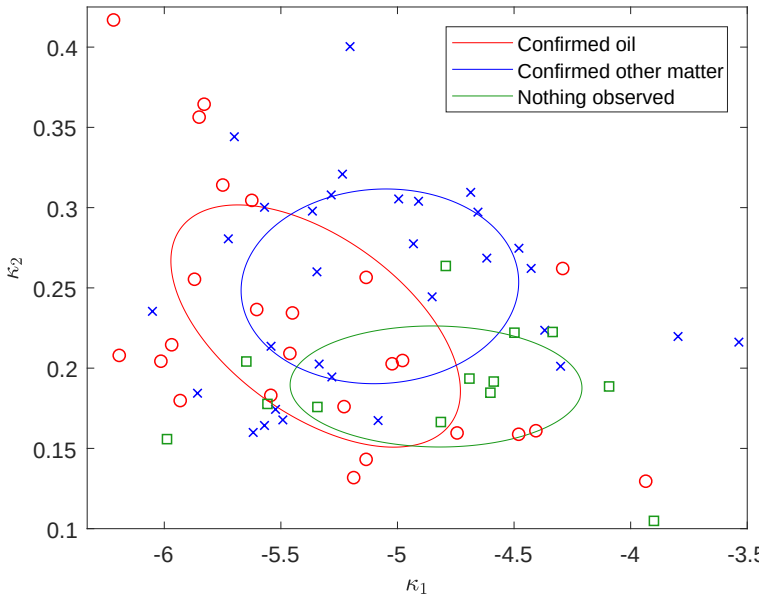

Figure A.8: κ_2 plotted as a function of κ_1, for dark features with incidence angle in the interval [30°,40°]. Confirmed oil spills are denoted by red circles, COM by blue crosses and nothing observed by green squares. The ellipses represent the mean and variation for each class.

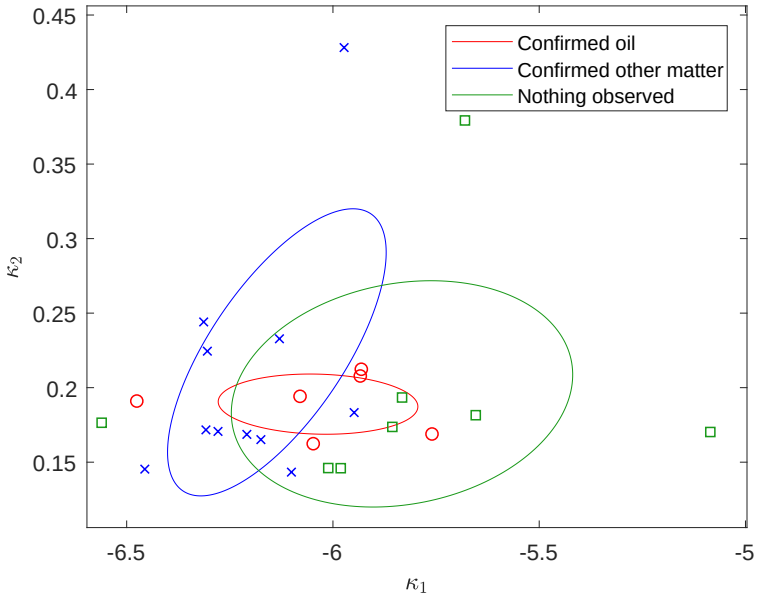

Figure A.9: κ_2 plotted as a function of κ_1, for dark features with incidence angle in the interval (40°,50°]. Confirmed oil spills are denoted by red circles, COM by blue crosses and nothing observed by green squares. The ellipses represent the mean and variation for each class.

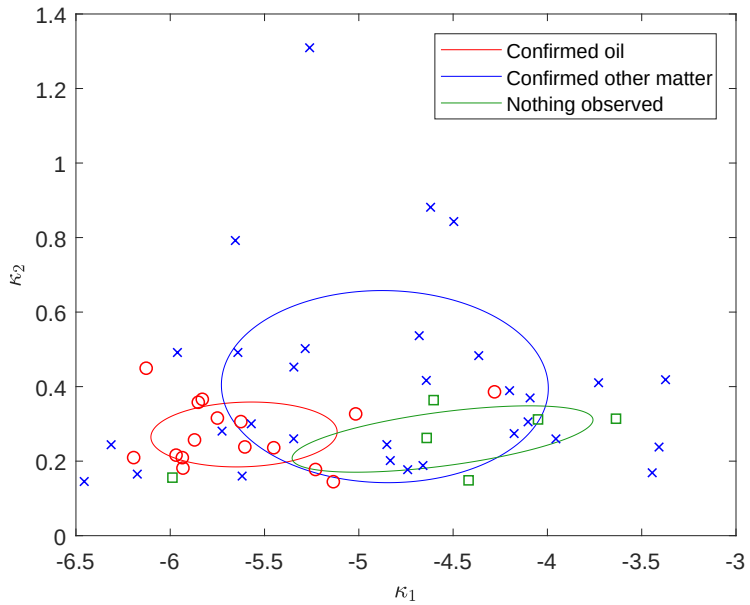

Figure A.10: κ_2 plotted as a function of κ_1, for dark features with SAR tool derived wind speed in the interval [0,2) m/s. Confirmed oil spills are denoted by red circles, COM by blue crosses and nothing observed by green squares. The ellipses represent the mean and variation for each class.

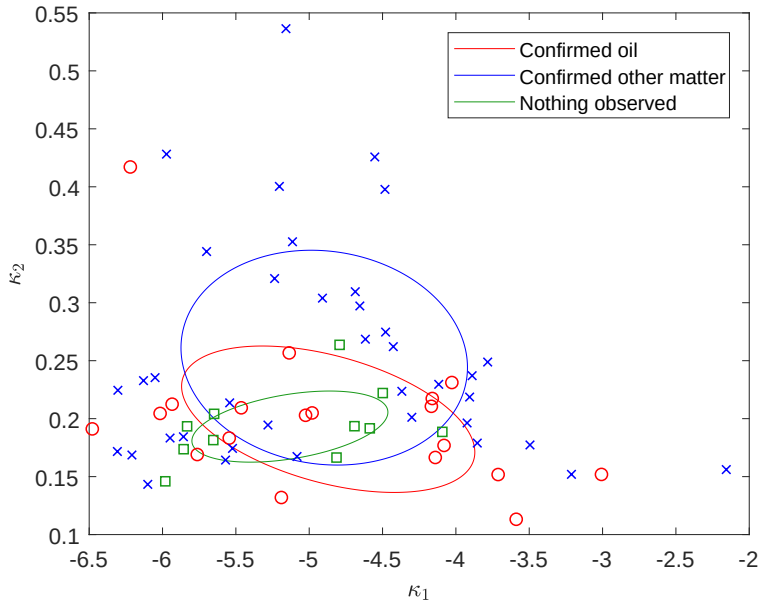

Figure A.11: κ_2 plotted as a function of κ_1, for dark features with SAR tool derived wind speed in the interval [2,4] m/s. Confirmed oil spills are denoted by red circles, COM by blue crosses and nothing observed by green squares. The ellipses represent the mean and variation for each class.

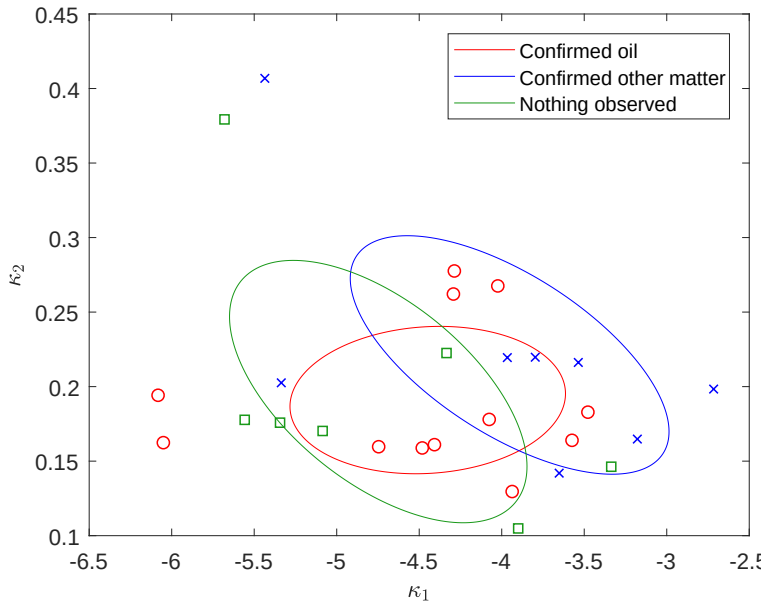

Figure A.12: κ_2 plotted as a function of κ_1, for dark features with SAR tool derived wind speed in the interval (4,12] m/s. Confirmed oil spills are denoted by red circles, COM by blue crosses and nothing observed by green squares. The ellipses represent the mean and variation for each class.

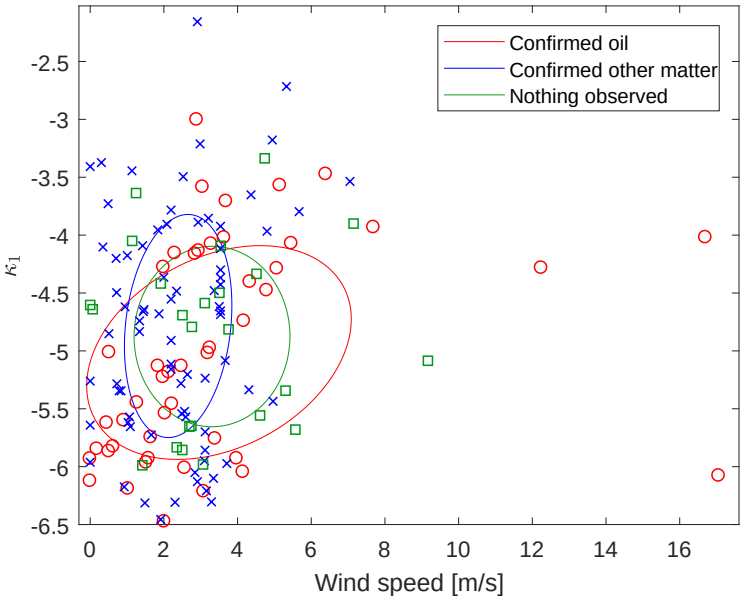

Figure A.13: κ_1 plotted as a function of SAR derived wind speed. Confirmed oil spills are denoted by red circles, COM by blue crosses and nothing observed by green squares. The ellipses represent the mean and variation for each class.

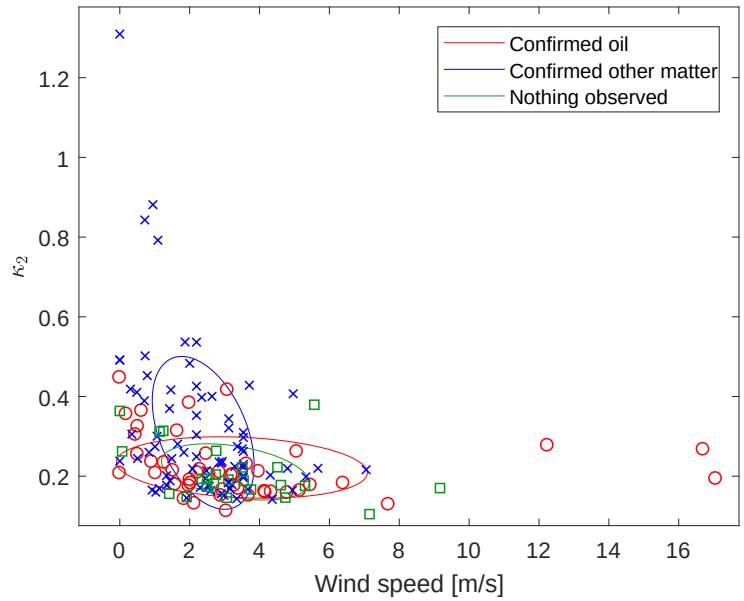

Figure A.14: κ_2 plotted as a function of SAR derived wind speed. Confirmed oil spills are denoted by red circles, COM by blue crosses and nothing observed by green squares. The ellipses represent the mean and variation for each class.

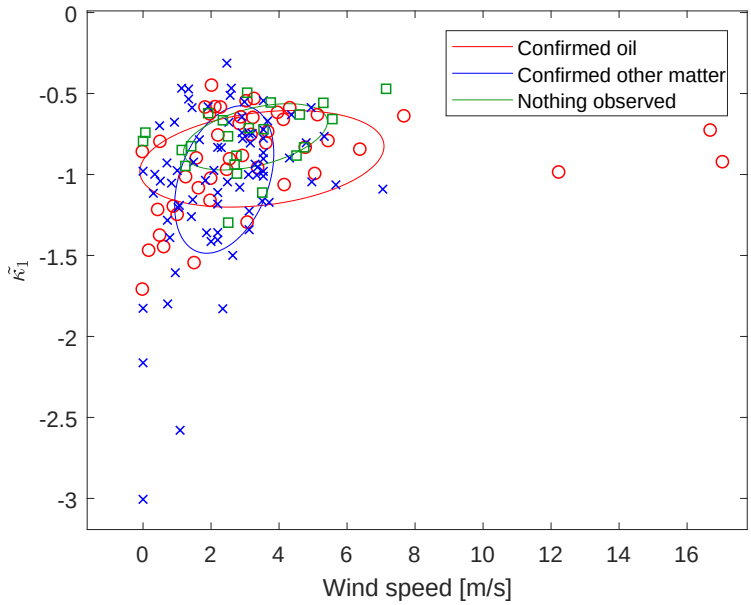

Figure A.15: $\tilde{\kappa_1}$ plotted as a function of SAR derived wind speed. Confirmed oil spills are denoted by red circles, COM by blue crosses and nothing observed by green squares. The ellipses represent the mean and variation for each class.

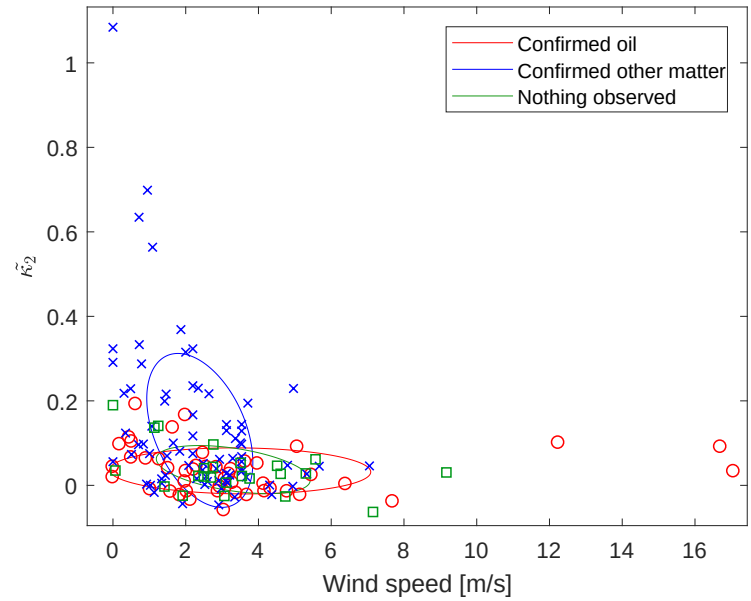

Figure A.16: $\tilde{\kappa_2}$ plotted as a function of SAR derived wind speed. Confirmed oil spills are denoted by red circles, COM by blue crosses and nothing observed by green squares. The ellipses represent the mean and variation for each class.

B Analysis of log-cumulants using Sentinel-1 GRDM format

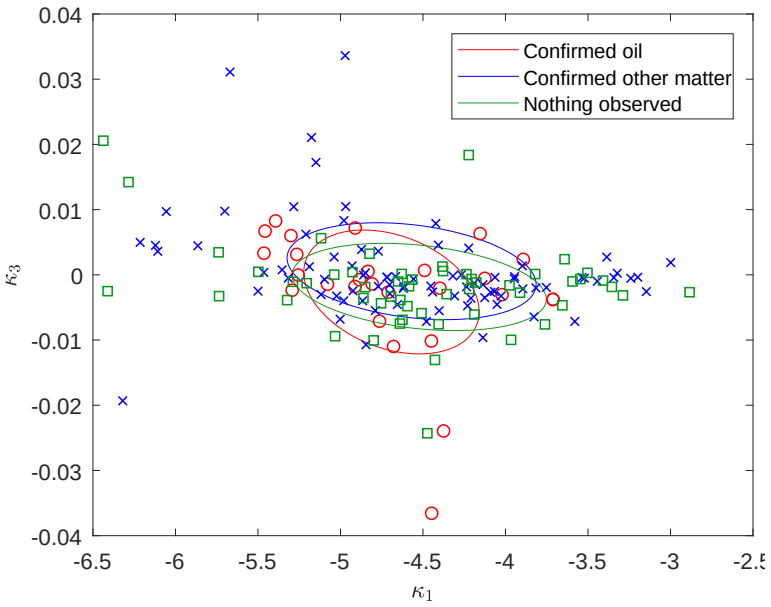

Figure B.1: κ_3 plotted as a function of κ_1, contains data calculated from GRDM products. Confirmed oil spills are denoted by red circles, COM by blue crosses and nothing observed by green squares. The ellipses represent the mean and variation for each class.

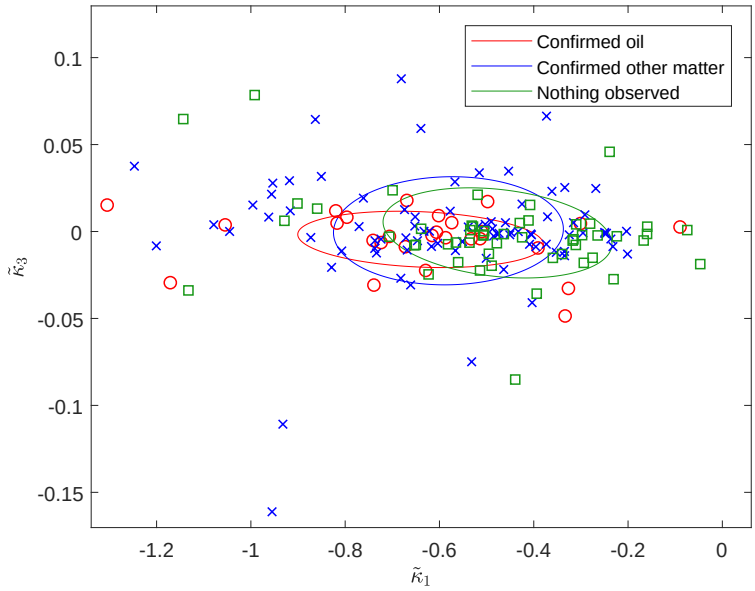

Figure B.2: $\tilde{\kappa_3}$ plotted as a function of $\tilde{\kappa_1}$ for GRDM data. Confirmed oil spills are denoted by red circles, COM by blue crosses and nothing observed by green squares. The ellipses represent the mean and variation for each class.

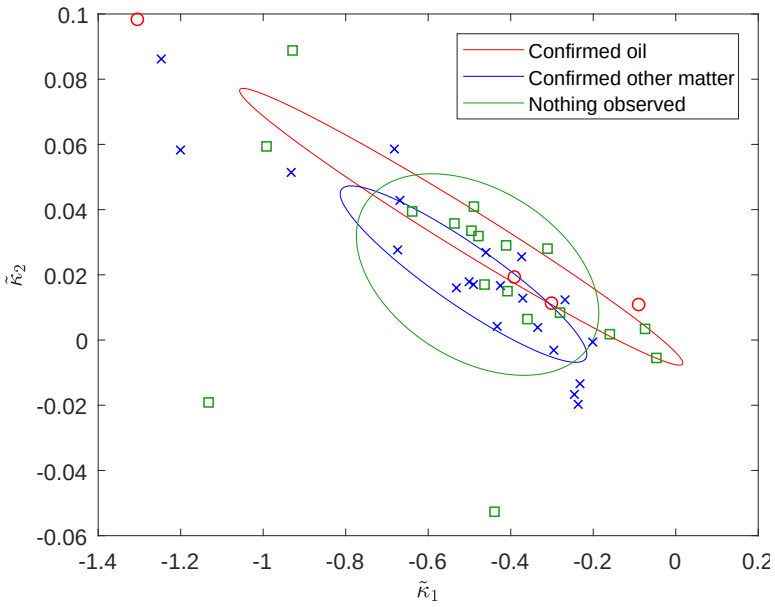

Figure B.3: $\tilde{\kappa_2}$ plotted as a function of $\tilde{\kappa_1}$, for dark features with incidence angle in the interval [30°,35°). Confirmed oil spills are denoted by red circles, COM by blue crosses and nothing observed by green squares. The ellipses represent the mean and variation for each class.

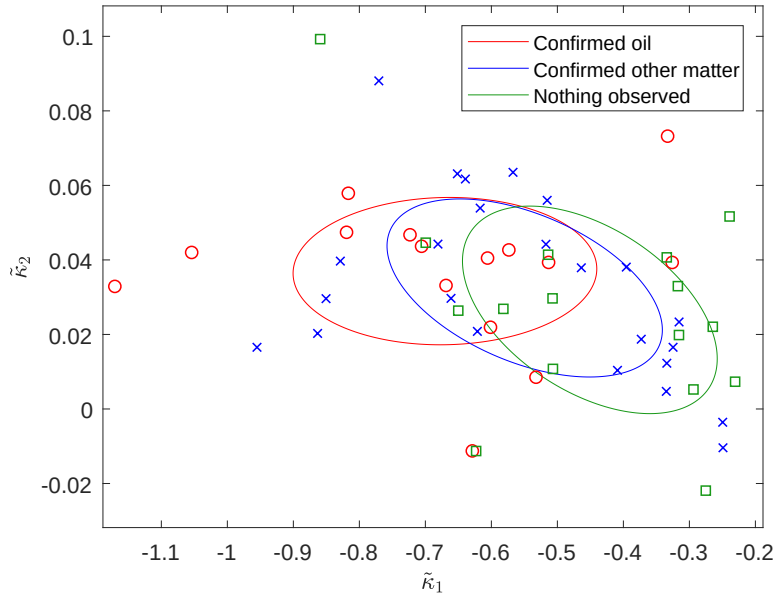

Figure B.4: $\tilde{\kappa_2}$ plotted as a function of $\tilde{\kappa_1}$, for dark features with incidence angle in the interval [35°,40°]. Confirmed oil spills are denoted by red circles, COM by blue crosses and nothing observed by green squares. The ellipses represent the mean and variation for each class.

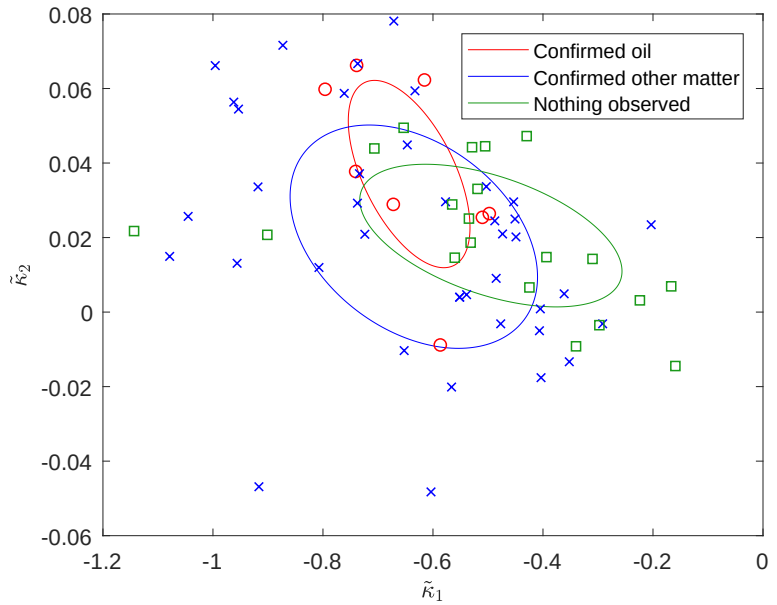

Figure B.5: $\tilde{\kappa_2}$ plotted as a function of $\tilde{\kappa_1}$, for dark features with incidence angle in the interval (40°,46°]. Confirmed oil spills are denoted by red circles, COM by blue crosses and nothing observed by green squares. The ellipses represent the mean and variation for each class.

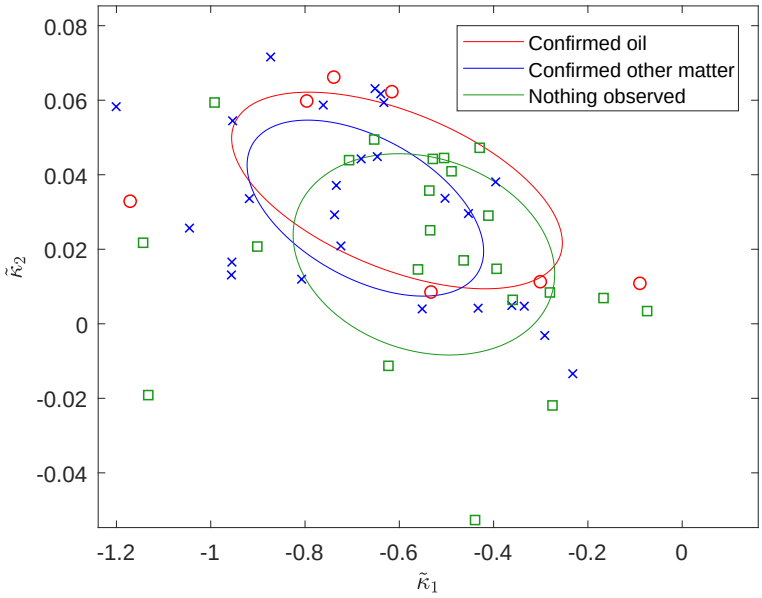

Figure B.6: $\tilde{\kappa_2}$ plotted as a function of $\tilde{\kappa_1}$, for dark features with SAR tool derived wind speed in the interval [0,4) m/s. Confirmed oil spills are denoted by red circles, COM by blue crosses and nothing observed by green squares. The ellipses represent the mean and variation for each class.

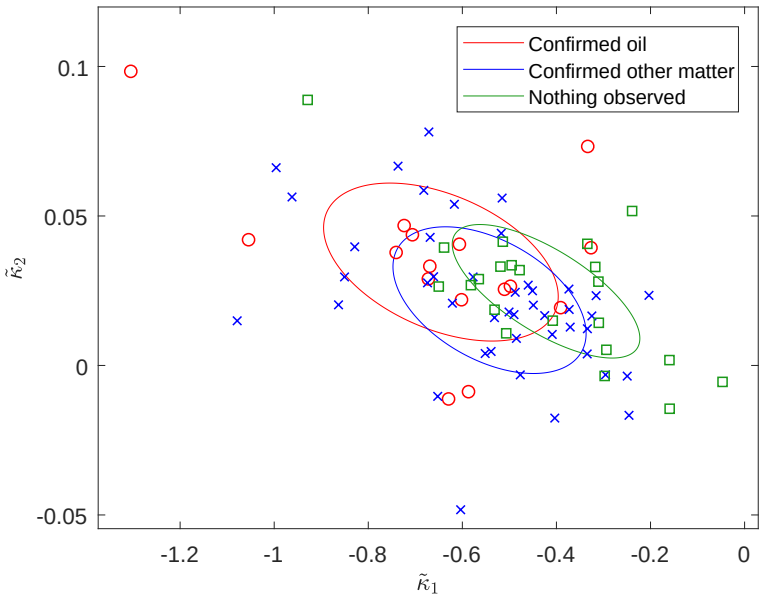

Figure B.7: $\tilde{\kappa_2}$ plotted as a function of $\tilde{\kappa_1}$, for dark features with SAR tool derived wind speed in the interval [4,8] m/s. Confirmed oil spills are denoted by red circles, COM by blue crosses and nothing observed by green squares. The ellipses represent the mean and variation for each class.

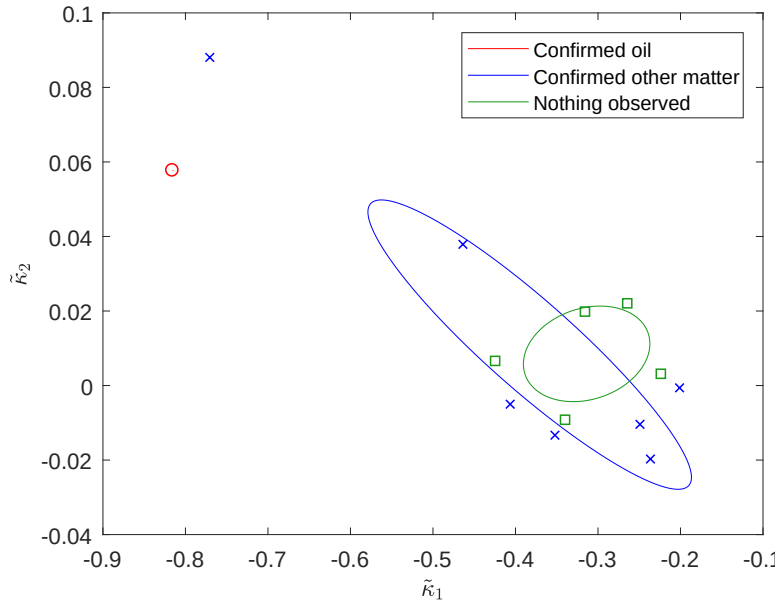

Figure B.8: $\tilde{\kappa_2}$ plotted as a function of $\tilde{\kappa_1}$, for dark features with SAR tool derived wind speed in the interval (8,14] m/s. Confirmed oil spills are denoted by red circles, COM by blue crosses and nothing observed by green squares. The ellipses represent the mean and variation for each class.

C Analysis of log-cumulants using Sentinel-1 GRDH format

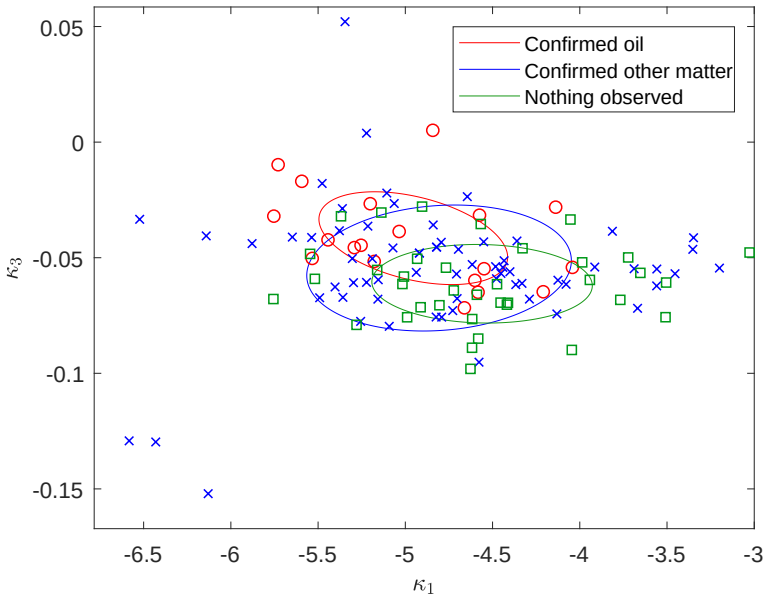

Figure C.1: κ_3 plotted as a function of κ_1, contains data calculated from GRDH products. Confirmed oil spills are denoted by red circles, COM by blue crosses and nothing observed by green squares. The ellipses represent the mean and variation for each class.

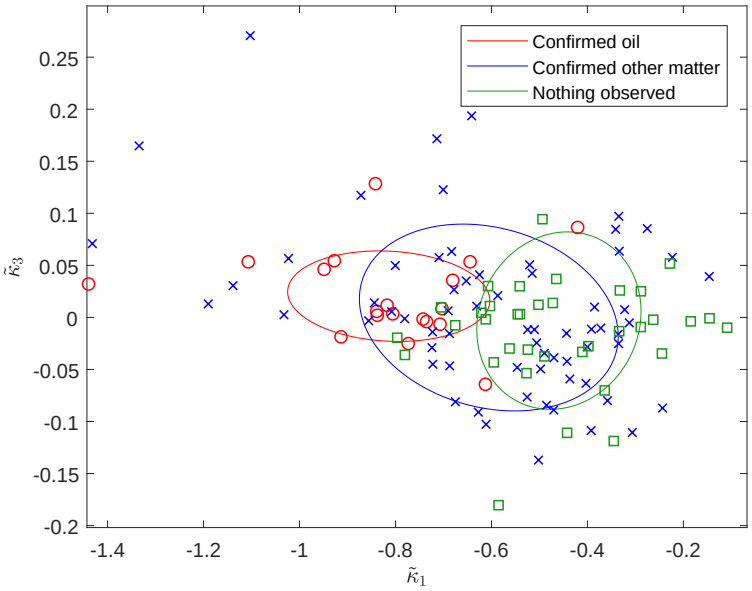

Figure C.2: $\tilde{\kappa_3}$ plotted as a function of $\tilde{\kappa_1}$ for GRDH data. Confirmed oil spills are denoted by red circles, COM by blue crosses and nothing observed by green squares. The ellipses represent the mean and variation for each class.

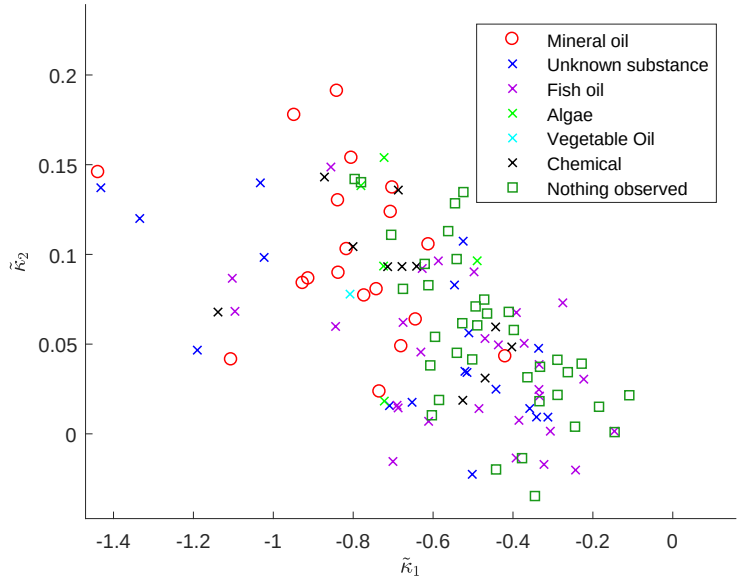

Figure C.3: κ_2 plotted as a function of κ_1. Confirmed oil spills are denoted by red circles, COM by crosses and nothing observed by green squares. The different classes of COM are separated by color.

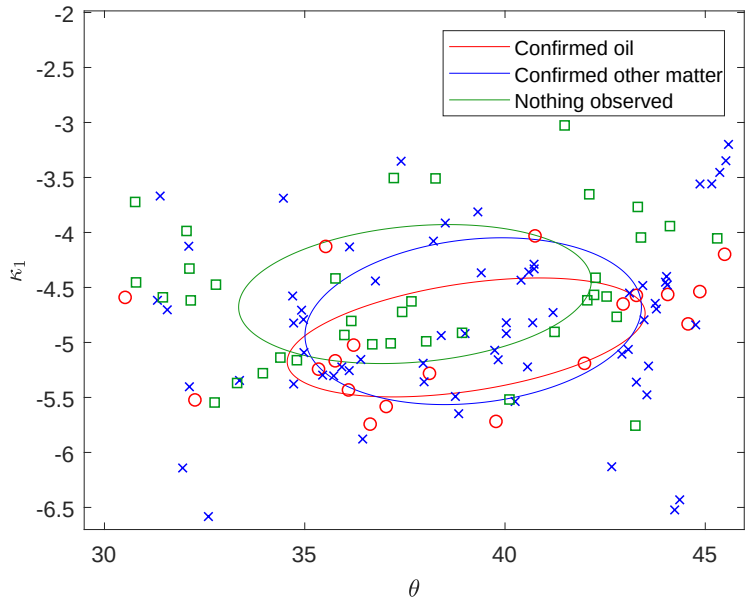

Figure C.4: κ_1 plotted as a function of θ. Confirmed oil spills are denoted by red circles, COM by blue crosses and nothing observed by green squares. The ellipses represent the mean and variation for each class.

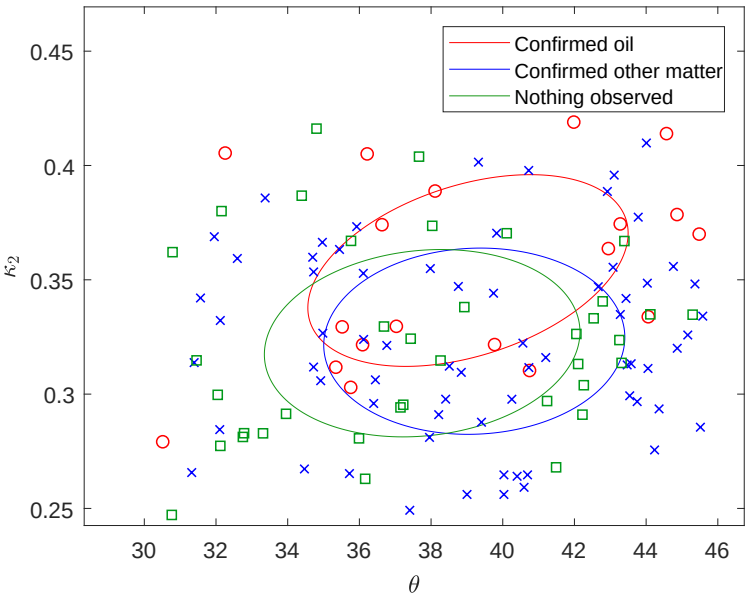

Figure C.5: κ_2 plotted as a function of θ. Confirmed oil spills are denoted by red circles, COM by blue crosses and nothing observed by green squares. The ellipses represent the mean and variation for each class.

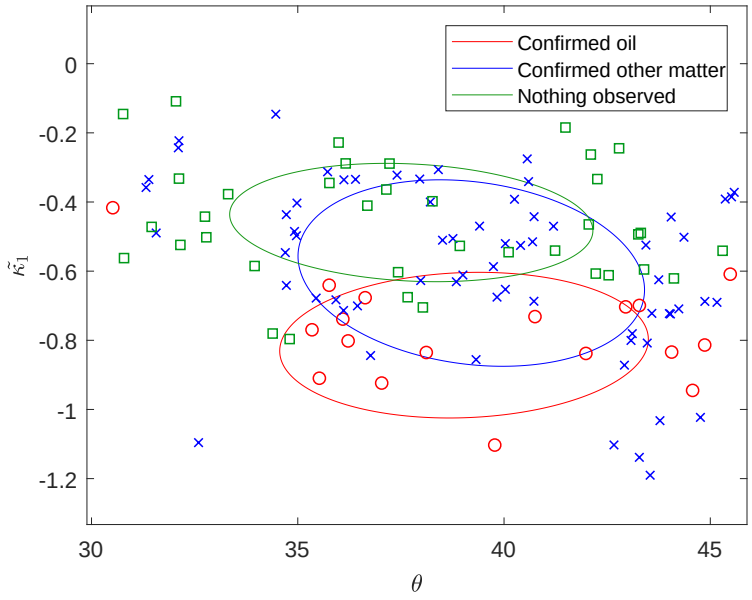

Figure C.6: $\tilde{\kappa_1}$ plotted as a function of θ. Confirmed oil spills are denoted by red circles, COM by blue crosses and nothing observed by green squares. The ellipses represent the mean and variation for each class.

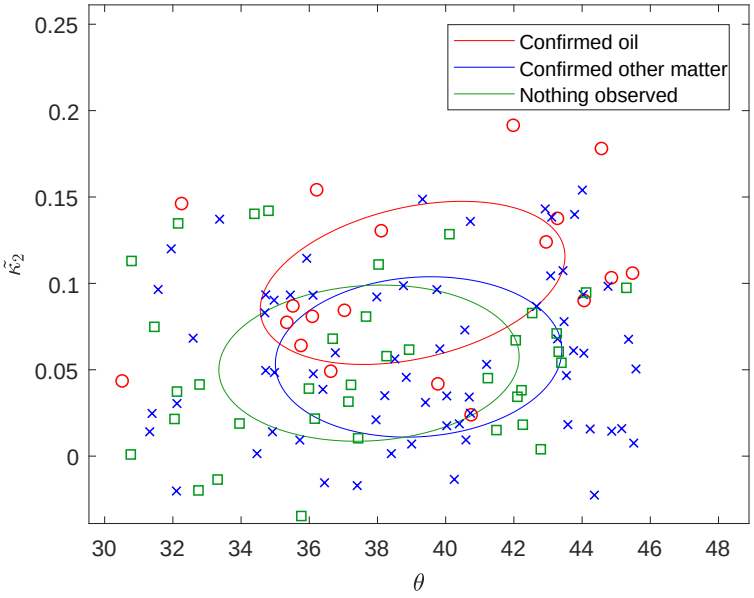

Figure C.7: $\tilde{\kappa_2}$ plotted as a function of θ. Confirmed oil spills are denoted by red circles, COM by blue crosses and nothing observed by green squares. The ellipses represent the mean and variation for each class.

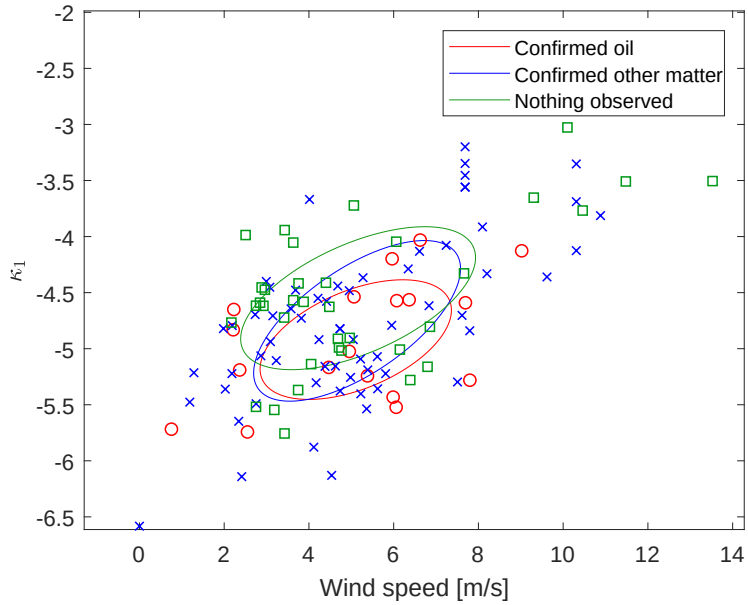

Figure C.8: κ_1 plotted as a function of SAR derived wind speed. Confirmed oil spills are denoted by red circles, COM by blue crosses and nothing observed by green squares. The ellipses represent the mean and variation for each class.

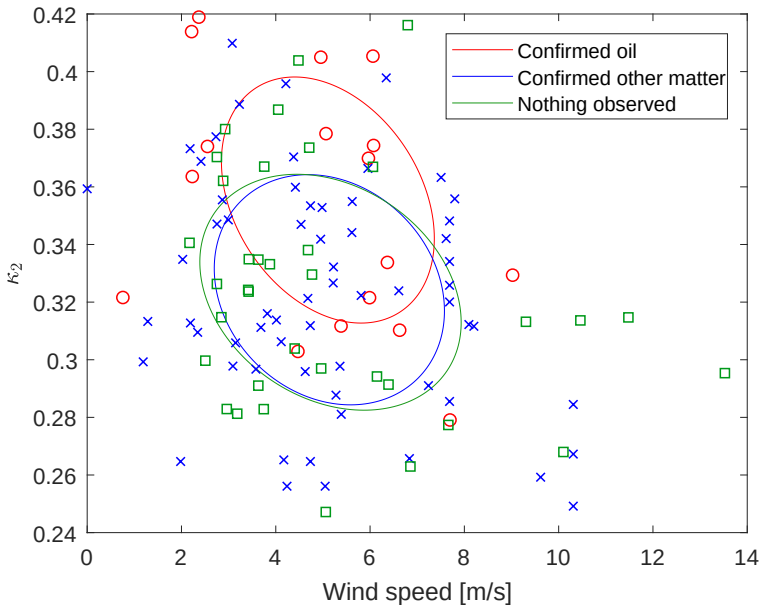

Figure C.9: κ_2 plotted as a function of SAR derived wind speed. Confirmed oil spills are denoted by red circles, COM by blue crosses and nothing observed by green squares. The ellipses represent the mean and variation for each class.

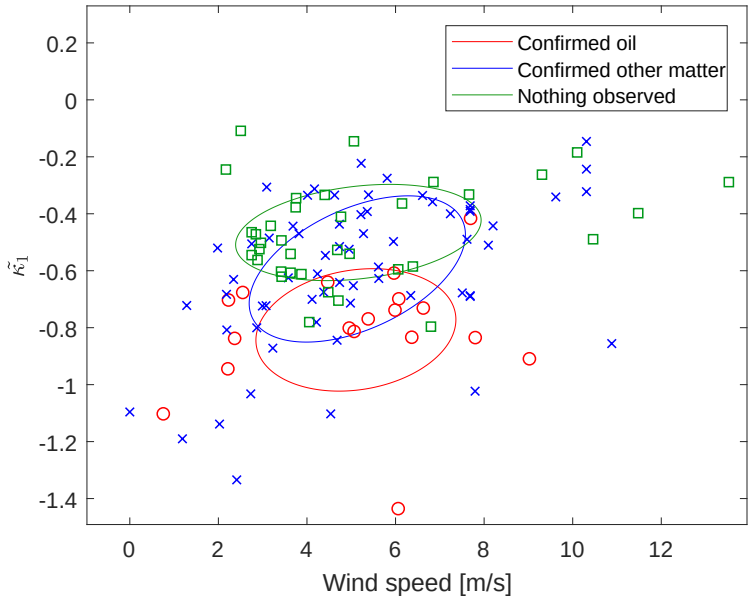

Figure C.10: $\tilde{\kappa_1}$ plotted as a function of SAR derived wind speed. Confirmed oil spills are denoted by red circles, COM by blue crosses and nothing observed by green squares. The ellipses represent the mean and variation for each class.

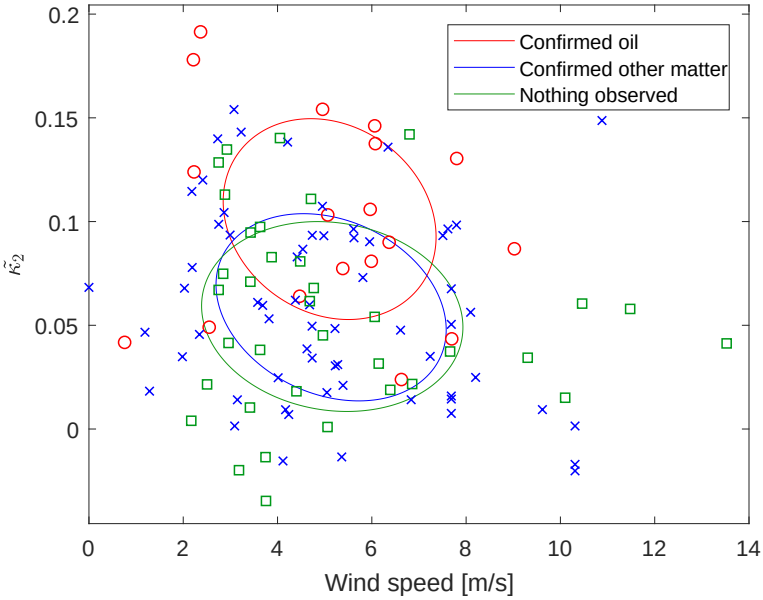

Figure C.11: $\tilde{\kappa_2}$ plotted as a function of SAR derived wind speed. Confirmed oil spills are denoted by red circles, COM by blue crosses and nothing observed by green squares. The ellipses represent the mean and variation for each class.